Université Libre de Bruxelles
Ecole polytechnique de Bruxelles
OPERA
Wireless Communications Group

Université Pierre et Marie Curie
Faculté d'Ingénierie
Laboratoire d'Électronique et
Électromagnétisme

Channel modeling for 60 GHz Body Area Networks

Dissertation originale présentée en vue de l'obtention du Grade de
DOCTEUR en Sciences de l'Ingénieur
de l'UNIVERSITÉ LIBRE DE BRUXELLES
et
DOCTEUR de l'UNIVERSITÉ PIERRE ET MARIE CURIE

préparée sous la direction des Professeurs
Philippe De Doncker et Aziz Benlarbi-Delaï

Présentée par

M. MAVRIDIS Theodoros

Composition du Jury :

Prof. Dricot Jean-Michel	Président
Prof. De Doncker Philippe	Directeur de thèse ULB
Prof. Benlarbi-Delaï Aziz	Directeur de thèse UPMC
Prof. Liénard Martine	Rapporteur
Prof. Oestges Claude	Rapporteur
Prof. Horlin François	Examinateur
Prof. Helier Marc	Examinateur
Dr. Sarrazin Julien	Encadrant

Remerciements

Voici donc l'une des parties la plus importante de la thèse. En effet, nombreux sont ceux qui ne liront que celle-ci ! Tout d'abord, merci aux autres ! Au final, la thèse est un travail personnel mais qui repose sur les contributions d'un entourage. Ce parcours m'a permis de constater que plus celui-ci est riche, plus la thèse est une expérience réussie. Aujourd'hui, je ne changerais rien à ces quatre dernières années. Avant tout, je souhaite remercier mes promoteurs : Philippe De Doncker et Aziz Benlarbi-Delaï qui m'ont fait confiance et donné l'opportunité de réaliser cette thèse en cotutelle. Aziz, merci de m'avoir accueilli si généreusement au L2E et d'avoir fait de moi un membre à part entière du laboratoire. Ayant passé le plus clair de mon temps au laboratoire OPERA WCG, mes plus chaleureux remerciements vont à Philippe. Je te remercie de ton temps, de la liberté que tu m'as donnée dans ma recherche, de la méthode scientifique que tu m'as transmise et des opportunités que tu m'as offertes. Tout ceci est en grande partie grâce à toi. Je souhaite aussi remercier les membres du jury de m'avoir fait l'honneur de s'intéresser à mon travail et de m'avoir partagé leurs avis et leurs critiques me permettant d'obtenir un manuscrit aussi abouti.

La thèse est faite par les expériences. J'aimerais donc saluer et remercier l'équipe de UBC et Dr. Michelson pour leur accueil et leur confiance. En particulier, Big Up à Siamak, Sina, Mina et bien sûr Maryam !

La thèse est aussi faite au jour le jour par les collègues. En quatre années, j'en ai vu passé un bon nombre que je tiens à saluer. Au commencement, il y avait les anciens. Je vous remercie tous pour ce que vous m'avez apporté: Stéphane, François Quitin, Ali & Oli, Jon, Jessica, Thibault et ses parties d'échecs, Matthieu et bien sûr, Bellou qui m'a accueilli comme "colocataire de bureau" et formé dans mes débuts. Tes « à la bouffe » m'ont manqué ces deux dernières années ! La relève est du même calibre : merci à Naim, Jeremy, Marie-Paul, Thomas, Sylvain, Florence, Marc, Solofo, Jean-François. J'aimerais aussi remercier Julien

Sarrazin d'avoir partagé son expertise, ses connaissances et son temps avec moi. Petite dédicace particulière au trio de tête: Dr. Hipster Petrillo, merci d'avoir partagé ces heures interminables au bureau, au labo ou en sur le square G ! Sullivan, merci pour les débats "on n'est pas couché" et tes prises de position de dictateur. Enfin, merci Dr. Jawad avec qui j'ai partagé ces dures heures de préparation du FRIA, des sons de rap, de soirées, de voyages,... c'tout.

La thèse est aussi faite de son entourage. Merci à mes amis d'enfance, les cinq toujours ensemble, d'être toujours là et d'avoir fait de moi en partie ce que je suis aujourd'hui. Merci à Némé pour les parties de ping pong et les soirées au Bazar, à Volo pour la période de rédaction et le groupe de travail/motivation. Merci aussi à Tarik pour tous ces midis, la natation, les cafés, les soirées Bomaye ! Enfin, mes parents sans qui tout ceci ne serait jamais arrivé. Merci pour de m'avoir transmis vos valeurs et d'avoir mis l'accent sur l'importance de l'éducation et de la scolarité. Merci à Eva d'avoir fait de moi un grand frère. Finalement, j'aimerais remercier Maria Victoria d'avoir partagé toutes ses années avec moi, tu as été d'un soutient inestimable et tu seras éternellement dans mon cœur.

Abstract

Abstract

Channel Modeling for 60 GHz Body Area Networks

The *smart environments* and the *connected human* seems to be the future of wireless communications. The development of new frequency bands in the millimeter range will allow us to create high data rate communications which will led to the *Wireless Body Environment Networks*. In this kind of scenarios, it is expected that the user and the environment will interact. In order to develop such new applications, it is necessary to first study the propagation mechanisms and then, the communication channel underlying body centric environments. This thesis treats of channel models for 60 GHz Body Area Networks and more particularly of three kinds of scenarios: (i) the communication between an external base station and a worn node (off-body); (ii) the communication between two worn nodes (on-body); the communication between an external base station and a hand-held device (near-body).

An indoor off-body channel model is numerically proposed and implemented. The model is based on the IEEE 802.11ad indoor standard channel at 60 GHz and a fast computation solution of the scattering of a plane wave by a circular cylinder. The model is developed for two orthogonal polarizations and the communications performances are studied.

The on-body propagation is studied for two different configurations: line-of-sight and non-line-of-sight communications on the body. These scenarios led to different solutions for the channel knowing as, respectively, Norton's equations and creeping formulations. These solutions are obtained using simplified geometries which has been experimentally validated. Further, in order to improve the propagation on the human body, a technique using metallic plates has been proposed. This technique has been theoretically studied using Milligton's equations and experimentally assessed on a flat phantom with the properties of the human skin. The proposed method allows to save up to 20 dB.

Finally, the near-body communication scenario has been introduced and studied. The near-body region is extended from 5 to 30 cm away of the user body which corresponds to the arm's reach and models a handheld device. A numerical algorithm has been proposed to model indoor near-body environments. Also, a special has been given to statistical body shadowing. It has been shown that the fading follows a Two-Wave Diffuse Power distribution.

Keywords : 60 GHz, Body Area Networks, Smart Environments, Connected Human, On-body, Off-body, Near-body, millimeter waves, Channel modeling, propagation, scattering, Experimental characterization.

Résumé

Modélisation de Canal pour Body Area Networks à 60 GHz

Les environnements intelligents et l'homme connecté semble être la prochaine évolution des télécommunications sans fil. En effet, le développement des nouvelles bandes de fréquence millimétriques permettront de créer des communications haut débit et de nouveaux types d'environnements, les Wireless Body Environment Networks, où les utilisateurs auront la possibilité d'interagir avec l?environnement. Pour développer ces environnements, il est nécessaire d'étudier les mécanismes de propagation et les canaux de communication sans fil autour du corps humain.

Cette thèse analyse les canaux de propagation pour les réseaux corporels à 60 GHz et plus particulièrement trois scenarios: (i) la propagation entre une station de base externe et un noeud placé à proximité du corps (off-body) ; (ii) la propagation entre deux noeuds portés sur le corps (on-body) ; (iii) la communication entre une station de base externe et un noeud tenu porté par la main de l'utilisateur (near-body).

Un modèle de canal numérique est proposé et implémenté pour modéliser la propagation off-body en environnement intérieur. Le modèle est basé sur le standard IEEE 802.11ad et une solution de la diffraction d'une onde plane incidente sur un modèle cylindrique du corps humain. Le modèle est développé pour deux polarisations orthogonales et les performances d'une communication WiGig sont étudiées via le bit error rate.

La propagation on-body est étudiée pour deux différentes configurations: avec et sans ligne de vue directe. Ces scenarios mènent à des solutions analytiques différentes: l'équation de Norton et l'onde rampante. Ces solutions sont obtenues en utilisant des modèles de corps simplifiés et ont été validées expérimentalement. De plus, une méthode permettant d'améliorer le bilan de liaison entre deux dispositifs portés sur le corps en utilisant des plaques métalliques réduisant les pertes de propagation. Cette technique a été illustrée théoriquement en utilisant les équations de Millington. Une campagne de mesure a été effectuée sur un modèle de corps plat ayant les propriétés électriques de la peau humaine. Il a été montré que cette méthode permet d'augmenter le bilan de liaison de 20 dB.

La région near-body s'étendant de 5 à 30 cm du corps humain est étudiée. Il s'agit de la région correspondant à la portée de main. Un algorithme numérique est proposé pour modéliser la présence d'un utilisateur dans un environnement intérieur. Un modèle statistique a aussi été proposé. Il a été montré que la distribution spatiale du champ suit une Two-Wave Diffuse Power distribution.

Mots-clés : 60 GHz, Body Area Networks, Environnement intelligent, Homme connecté, On-body, Off-body, Near-body, Ondes millimétriques, Modélisation de canal, propagation, Diffusion, Charactérisation Expérimentale.

Contents

List of Figures

List of Tables

Acronyms

BAN	Body Area Networks
WBAN	Wireless Body Area Networks
WBEN	Wireless Body Environment Networks
UWB	Ultra Wideband
ISM	Industrial, scientific and medical
FCC	Federal Communications Commission
ETSI	European Telecommunications Standards Institute
CEPT	European Conference of Postal and Telecommunications Administrations
EIRP	Equivalent isotropically radiated power
ICNIRP	International Commission on Non-Ionizing Radiation Protection
IEEE	Institute of Electrical and Electronics Engineers
60GBAN	60 GHz Body Area Networks
VNA	Vector Network Analyzer
HD	High Definition
GO	Geometrical Optics
TWDP	Two-Wave Diffuse Power
OFDM	Orthogonal Frequency-Division Multiplexing
PEC	Perfectly Electrical Conductor
FDTD	Finite-Difference Time-Domain
IQR	Interquartile Ranges
WiGig	Wireless Gigabit Alliance
TM	Transverse Magnetic
TE	Transverse Electric
dB	decibel
Rx	Receiver
Tx	Transceiver
MSRE	Mean Square Root Error
SNR	Signal to Noise Ratio
IF	Intermediate Frequency
BER	Bit Error Rate

Chapter 1

Context

Contents

1.1 Wireless Body Environment Networks

With the widespread of the internet, the *connected world* is available for almost each of us. Entrepreneurs, programmers and worldwide companies have imagined a new vision of future technologies: *connected environments* also called *smart environments*. In these environments, it is expected that objects will be permanently connected to the network. They could be monitored and controlled at distance, or they could become *smart* and adapt their behaviour by learning from daily experience and by exchanging information. These *Smart Environments* have been under study for a few years now [4] and are appearing more and more often in our everyday life.

One of the key issue to ensure the development of such environments is the *connected human* which is also bound to the scientific field of Body Area Networks (BANs). The need for new applications and technologies in the field of healthcare and entertainment have led to the development of body worn sensors. These sensors are communicating around the human body and are sharing information for an over-the-air treatment or to store data. These networks have been widely studied in the ISM bands such as 2.45 GHz and also in the Ultra Wideband (UWB) from 3.1 to 10.6 GHz [5].

Actually, theses two visions, *smart environment* and *connected human*, may appear as one: Wireless Body Environment Network (WBEN). In this latter, it is expected that the user can interact with the environment and the environment will respond to him. New human-centred services such as HD streaming video, augmented reality, wireless gaming or Gigabit Ethernet, but also health monitoring, comfort improvement, well being increase will be part of our future. The availability of wearable wireless high data rate technologies will be one of the key issue of these WBEN.

The development of such WBEN does not seem to be easily reachable with today's technology. But the recent progress in low-cost mm-wave circuit design allows us to use new frequency bands such as the 60 GHz band. This band offers an unlicensed bandwidth available all around the world and thus the possibility to develop new communication services such as HD streaming video, augmented reality, wireless gaming, Gigabit Ethernet,... [6]. The 60 GHz band is expected to become the new WiFi band for indoor short range communications. The major drawback of millimeter frequencies is the high propagation losses. But the small wavelength allows one to build really compact and efficient antenna arrays which will improve the communication quality. Also, the human body proximity can create higher losses and signal fading. Before implementing and optimizing these systems, it is necessary to model the propagation for different scenarios such as, for instance, the channel between two devices embedded on the human body (on-body propagation) or the communication between an external base station and a body worn device (off-body propagation).

In conclusion, mm-waves, and more specifically 60 GHz systems, seem to be the key to realize Wireless Body Environment Networks. Fig. 1.1 presents a schematic view of a WBEN. Different kinds of channel can be identified:

- two nodes worn on the body: on-body channel
- a node worn on the body and the external base station: off-body channel
- two nodes worn by different users: body-to-body channel

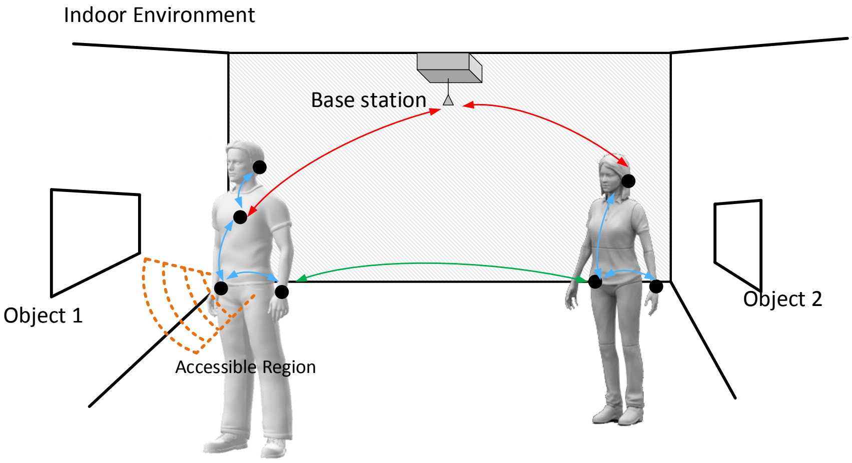

Figure 1.1: Schema of users placed in a WBEN. The users can interact with smart object, the base station and toghether. The accessible region presented here shows the typical region where the user can interact with objects.

The aim of this thesis is the characterization and modeling of on- and off-body channels for 60 GHz WBENs.

1.2 60 GHz Wireless Communications

Indoor and Mobile Communications

In the past years, millimeter wave (mm-wave) technology has mainly been used for military applications. However, with the progress in manufacturing and in low-cost integration solutions, a great deal of work has been done towards mm-wave communications for commercial applications [7]. More particularly, the recent breakthrough in silicon-based complementary metal-oxide-semiconductor (CMOS) processes and the gate length of transistors reaching sizes below 50 nm allow the development of highly integrated transmitters and receivers [8]. One of the main advantage is the huge unlicensed bandwidth (up to 7 GHz) allocated in 2001 by the Federal Communications Commission (FCC). A summary of the most recent global regulatory results is presented in Table 1.1.

Table 1.1: Emission power requirement

Region	Bandwidth	Tx Max Power	EIRP	Max Gain
USA	7 GHz (57-64)	500 mW	40 dBm	NS
Canada	7 GHz (57-64)	500 mW	40 dBm	NS
Japan	7 GHz (59-66)	10 mW	NS	47 dBi
Australia	3.5 GHz (59.4-62.9)	10 mW	max 150 W	NS
Korea	7 GHz (57-64)	500 mW	TBD	TBD
Europe	9 GHz (57-66), min 500 MHz	20 mW	max 57 dBm	37 dBi

In Europe, the European Telecommunications Standards Institute (ETSI) and European Conference of Postal and Telecommunications Administrations (CEPT) have established the legal framework for the deployment of 60 GHz devices. 9 GHz unlicensed spectrum is allocated for 60 GHz applications with a minimum spectrum of 500 MHz and a maximum EIRP of 57 dBm. It has been proposed that the 64-66 GHz band is allocated to point-to-point fixed services and the use of 57-59 GHz can be allocated to fixed services without requiring frequency planning [9, 10].

Compared to the ultra wideband (UWB) between 3.1 and 10.6 GHz [11], 60 GHz offers a continued bandwidth with higher transmit power. This high transmit power is necessary to overcome the path losses at 60 GHz. With the miniaturization and the compact size of the 60 GHz systems, efficient technologies with numerous antennas will be developed which was not possible at lower frequency.

Several research groups and consortium [12, 13, 11] have been focused on the development of 5G mobile communications. The key points for 5G are high data rates and low latency ensuring high quality of service. To cope with these requirements, new frequency bands are investigated. Most of the research have been focused in the 28 GHz and 38 GHz bands since 1 GHz bandwidth is available in the USA [12]. Also the 60 GHz and 73 GHz bands have been more recently under interest for the same reasons (wide available bandwidth). Other bandwidths are still highlighted by the FCC such as the 24 GHz, 42 GHz and 80 GHz ones [11].

The development of future Wireless Personal Area Networks (WPANs) and Wireless Local Area Networks (WLANs) is aiming to push the technology to provide gigabits per second throughput. WLAN devices are carrying Internet traffic and are operating under the IEEE 802.11n standard. The Very High Throughput study group of IEEE [14] is considering the 60 GHz bandwidth for the next generation of WLAN. Also, the development of gigabit Ethernet (WPAN) is driving the development of 60 GHz solutions. The IEEE 802.15.3c is developing a communication standard for wireless data transfers in order to replace USB or gigabit Ethernet cables. Wireless multimedia uncompressed streaming is also one of the main application which fosters the development of future indoor wireless communications and more particularly, of 60 GHz technologies. The Wireless Gigabit (WiGig) Alliance [15] has been formed to promote the IEEE 802.11ad protocol in order to accelerate the commercial development of the expansion of the Wi-Fi. WiGig gives technical specifications for 60 GHz communications such as modulation type, coding rate, power, etc.

60 GHz Body Area Networks

Body Area Networks have been widely studied at lower frequencies as it has been shown previously but with the development and widespread of the 60 GHz technologies, research groups have focused on 60 GHz Body area Networks (60GBANs). The wideband mm-wave spectrum, the miniaturization of electronic devices, the interference reduction and the high channel security are key factors motivating the development of 60GBANs [16]. Moreover, the development of mm-wave mobile communications is definitely pushing for the study of 60GBANs. It is important to note that body area networks is wider than only the communication between two embedded nodes. For instance, the off-body communication between an external base station and a device in close proximity of the human body is of first importance in mobile and even indoor communications. At millimeter frequencies, the human body becomes electrically large and cannot be neglected anymore.

The question of the feasibility of 60GBANs is legitimate since the communication is affected by high path loss. An answer has been sketched by *Sarrazin et al* by discussing the size of the antennas [1]. It is recalled that the major constraint of BANs is the size of the devices worn by the user since it has to remain comfortable. The advantage of millimetre wave frequencies is that the efficiency of centimetric and even millimetric antennas is high while at lower frequencies, the antennas may be inefficient. This leads to the fact that the antenna efficiency has to be taken into account as well as the path loss to assess the link budget.

In Fig. 1.2, a comparison of the power attenuation including the antenna efficiency at several frequencies is given, for a small antenna (0.5 mm). 60 GHz appears attractive for small distances links. However, these results become less and less true when the antenna size is growing (60 GHz becomes less interesting). But, these preliminary simulations do not take into account the presence of the body on the antenna Q-factor and they still need to be refined in the future to make the results more realistic. Nevertheless, it allows us to mitigate the effortless statement that mm-waves are not suited because of propagation losses. Also, the development of antenna arrays to focus the power into a specific direction will permit to widely increase the received power compared to lower frequencies where spatial diversity is not possible.

When our group started to focus on the characterization of 60GBANs, very few results were already published. One of the earliest published result was the simulated mm-wave communication between soldiers in a battlefield [17] using Geometrical Optics (via a ray-launching algorithm). To our best knowledge, it was the first mm-wave body-to-body results which showed the feasibility of 60GBANs. During the past four years, some research groups have started to conduct research on 60GBAN such as *Université Rennes 1*, *University of Birmingham*, or *University Queen Mary*. Most of their research have been

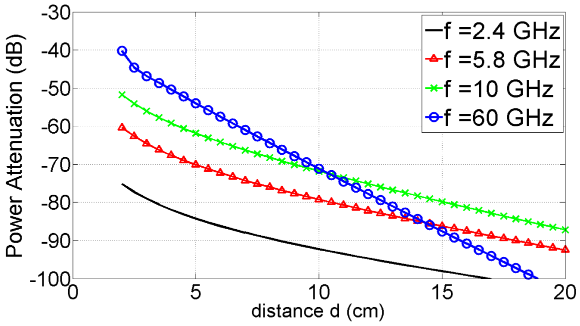

Figure 1.2: Link budget including antenna efficiency for antenna radius of 0.5 mm, antenna height of 5 mm and antenna Q-factor of 25 [1].

focused on the development of wideband efficient 60 GHz antennas for body centric applications [16] and phantoms manufacturing [18]. Indeed, wearable antennas have been proposed by [19] for 60 GHz on-body propagation, by [20] for off-body communications, and also textile antennas have been developed by [21].

The enthusiasm for mm-wave body centric applications and these research groups showed promising results for the development of 60 GHz Body Area Networks.

Human Exposure Issue

The development of such body worn wireless networks (re-)introduces the debate about exposure and safety. More particularly, the use of new band of the radio frequency spectrum deserves a special look at the impact of mm-waves on the human body. Recently, *Wu, Rappaport* and *Collins* published a state-of-the-art review paper summarizing all the conducted works on mm-wave body exposure. This paper [22] is the main basis of the following.

Most of the research reveals no adverse health effects that are not thermal [23]. The well-known and understood thermal effects consist into the heating of tissues exposed to electromagnetic radiations as stated by the IEEE International Committee on Electromagnetic Safety. In the case of extreme high intensity exposure, the US army investigated the use of very powerful mm-wave beams to ensure crowd control. The only observed effects could be explained by thermal effects [24]. In the case of mm-waves, the heating is limited to surface effects (eyes and skin) since the small penetration depth prohibits energy to propagate deeper into the body.

In [22], it is proposed to describe the electromagnetic energy with a particle formalism instead of common waves. Each photon has an energy $E = hf$ where h is Planck's constant and equal to 6.626×10^{-34} J.s and f is the frequency of the radiated signal in Hz. This equation shows that the energy of the photon increases with the frequency which may lead to ionizing issues. Nevertheless, the photon energy to remove an electron from an atom is about 12 eV. The energy of the photon at 100 GHz is 4.135×10^{-4} eV which is four order weaker and thus mm-waves are not able to displace electrons. The disruption of molecules due to ionization is linked to cancer. Mm-waves are then safe concerning ionization.

In classic radio frequency dosimetry, the whole body specific absorption rate (SAR) is often used in order to characterize the human body exposure. However, at mm-wave frequencies, the absorbed energy is localized in the skin and therefore, the use of whole body SAR is questionable.

The heating effects are rather related to the incident power density S defined in the far field as:

$$\mathrm{S} = \frac{G \cdot P}{4\pi d^2} \tag{1.1}$$

where G is the transmit antenna gain, P is the transmit power in W and d is the distance from the source. The FCC and the ICNIRP give a restriction on S averaged over the whole body of 10 $\mathrm{W/m^2}$ for general public exposure in the millimeter wave range. There is still a lack of near-field recommendations for mm-wave. It has been proven that this leads to a temperature elevation of 0.1 ° C [22] at 60 GHz. Humans are able to detect a warmth change of less than 0.1 ° C on the skin induced by mm-wave radiation [22]. In [25], it is claimed that temperature changes in the skin of 1 ° C are safe. The eyes are particularly vulnerable because of the lack of blood irrigation. Several studies have been conducted on primate eyes such as [26] which showed that 60-GHz mm-wave radiation at 10mW/cm^2 during 8 hours caused no ocular damage.

1.3 Thesis Contribution and Outline

The main objective of this thesis is to propose channel models for 60 GHz Body Area Networks and therefore, to physically understand and to quantitatively assess the impact of the human body on the propagation and communication.

In **Chapter 2**, the state of the art of body centric channels in the industrial, scientific and medical (ISM) radio bands and ultra-wideband is recalled. More particularly, the path loss, shadowing and small-scale fading are detailed and reviewed. Then, a special interest is given to 60 GHz body area channels. Since human blockage has been studied, the major results are recalled. The first numerical and experimental results regarding 60 GHz on-body propagation are then discussed.

Chapter 3 proposes a numerical indoor wideband channel model for off-body communications. This model is implemented using the indoor IEEE 802.11ad channel and the scattering of a plane wave by a circular cylinder. A simplified diffraction model is first proposed and validated for this last problem. This channel is developed for two orthogonal polarization and these polarization are discussed using an orthogonal frequency-division multiplexing (OFDM) communication.

Then, in **Chapter 4**, on-body propagation is investigated theoretically and experimentally. A on-torso path loss model is first proposed using Norton's formulations. The shadowing is then experimentally investigated. Secondly, an around-torso propagation model is described using creeping waves. This model is experimentally studied with a perfect electrical conductor (PEC) cylinder and with a real human body. Finally, a method using metallic plates located on the body is proposed to improve propagation. It is theoretically studied using Millington's equation and experimentally validated with a flat human body phantom.

In **Chapter 5**, the propagation between an external transmitting base station and a device hold by the user hand is described and referred to as *Near-Body* propagation. This scenario is numerically investigated using a method similar to the one developed in Chapter 3. A special interest is given on body shadowing and modeled using a Two-Wave Diffuse Power (TWDP) distribution. This last distribution is then experimentally verified.

Finally, **Chapter 6** recalls the major contributions and concludes this thesis.

Chapter 2

Body Area Networks Channel Modeling

Contents

2.1 Body Area Channels

2.1.1 The radio channel

The propagation medium between a transmit and a receive antenna is called the *radio channel*. The transmitted electromagnetic waves interact with the environment before exciting the receive antenna. These interactions are complex and highly dependent on the environment. This does not allow an accurate deterministic description of the radio channel. This can be easily understood by imagining a complete indoor environment model and the calculation of each electromagnetic interaction with every tiny objects of the environment. Further, the dynamics of the channel is almost impossible to predict accurately (objects, people or even base stations moving).

Statistical modeling is then often preferred. However, this method also suffers from drawbacks. It requires the channel to have time and space stationary statistics. This condition is not always met.

The baseband impulse response of the radio channel $h(t)$ links the received signal $y(t)$ and the transmitted signal $x(t)$ as

$$y(t) = \int_{-\infty}^{+\infty} x(t-\tau)h(t,\tau)\mathrm{d}\tau \tag{2.1}$$

where t is the time, $n(t)$ is the additive noise at the receiver side and $*$ is the convolution product.

The transmit antenna radiates waves in certain directions depending on its radiation pattern. Each wave will interact differently with the environment. Finally, the waves arrive at the receiver with a propagation delay τ. The magnitude of the voltage excited by each wave depends on the radiation pattern of the receive antenna, and so it depends on the angle of arrival of each wave. Regarding this description, there are then three distinct elements that build the channel:

- the effect of the transmit antenna
- the effect of the environment on each transmitted wave
- the effect of the receive antenna

This channel h is also called the *Communication Channel* while the *Propagation Channel* only concerns the effect of the environment. The description and characterization of the propagation channel consists in studying each wave and, as discussed above, modeling the parameters of each of them such as the amplitude, the phase, the delay, the polarization, the angles of departure and arrival. However, to perform such model, it is necessary to be able to discriminate each wave. This requires wideband measurements leading to a precise temporal resolution.

Path loss

By conservation of energy, the integral over any sphere of the power radiated in free space from any source is a constant. This simply leads to an electric field strength inversely proportional to the distance between the source and the observation point. The path loss description is based on this result. The received power decreases with the distance between the transmitter and the receiver. The environment will define how much the power is reduced and is usually described using a path loss exponent which describes the power reduction with the distance. The path loss exponent is equal to 2 in free space but can go way up in some environments such as 4 in indoor environments or even higher in non-line-of-sight scenarios.

Shadowing

The effect of large obstacles on the received power variation is usually called shadowing. It can be easily understood by thinking of the effect on the signal of a person crossing the direct path between fixed transmit and receive antennas. This will create a variation in the received power. Variations of the channel around the path loss are often statistically characterized thanks to measurement campaigns.

Small-scale fading

The narrowband channel impulse response is made up of one tap which is the sum of all propagation paths. When the receiver or the transmitter slightly move, the propagation paths sum up differently because of the phase shifts due to the displacement. This interference is the small scale fading. It is statistically modeled using spatial or temporal distributions derived from measurements.

2.1.2 The Saleh-Valenzuela Impulse Response

Wideband systems implies frequency-dependent channel. The description of the channel is usually done in the delay-domain by considering an impulse response made up several propagation paths. The Saleh-Valenzuela impulse response model is the most commonly used. An example of measured and schematic impulse response is shown in Fig. 2.1.

Discrete time models are based on the channel impulse response:

$$h(\tau) = \sum_{k=1}^{N} \alpha_k \delta(\tau - \tau_k) \tag{2.2}$$

where α_k is the complex amplitude on path k, τ is the excess delay, τ_k is the delay of path k, N is the number of multipath components (MPCs) and $\delta(\cdot)$ stands for the Dirac function. The Saleh-Valenzuela channel model goes further by describing each path by a cluster which is made of several multipath components. (2.2) is then modified as:

$$h(\tau) = \sum_{i=0}^{C} \sum_{j=0}^{L_i} \alpha_{i,j} \delta(\tau - T_i - \tau_{i,j}) \tag{2.3}$$

where C is the number of clusters, L_i the number of MPCs in cluster i and T_i is the arrival time of cluster i. The cluster arrivals are described by a Poisson process implying an inter arrival time given by an exponential random variable:

$$p(T_i|T_{i-1}) = \Lambda e^{-\Lambda(T_i - T_{i-1})} \tag{2.4}$$

with Λ the mean cluster arrival rate, $T_0 = 0$ and $i > 0$.

This model also predicts an exponential decrease of the cluster power such as:

$$|\alpha_{i,j}|^2 = |\alpha_{0,0}|^2 e^{-T_i/\Gamma} e^{-\tau_{i,j}/\gamma} \tag{2.5}$$

where $|\alpha_{0,0}|^2$ is the power of the first MPC of the first cluster, γ is the intra-cluster power decay and Γ is the cluster power decay.

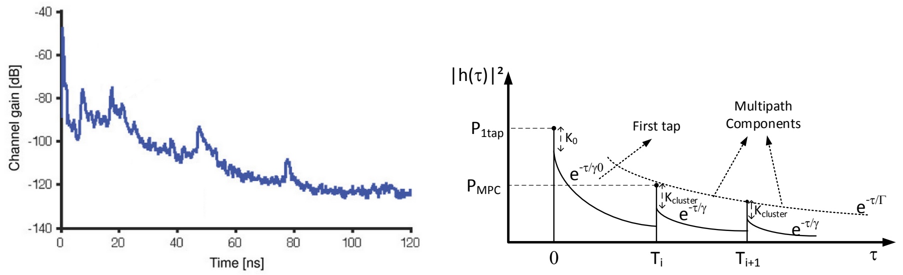

(a) Measured Example (b) Model

Figure 2.1: Measured and schematic impulse response

2.1.3 On-Body Channels

With the increase of calculation capabilities, several numerical solutions for on-body propagation have been proposed. Method of Moments (MoM) and Finite-Difference Time-Domain (FDTD) [27, 28] are the most used numerical methods to solve electromagnetic problems. However, due to large computation time and complicated structures modeling the body, ray-based methods are more commonly used. The development of the Uniform Theory of Diffraction (UTD) [29] which generalizes the Geometrical Optics (GO) have led to the use of diffraction mechanisms in order to simulate body area communications with simplified geometries of the human body. For instance, in [30], a comparison between UTD and FDTD is provided using a 3D simplified body model made of several cylinders. Good agreements between simulations and measurements is shown in the frequency band ranging from 3 to 9 GHz. Also, in [31], the modal solution of the scattering of a line source by a circular cylinder is extended to an iterative algorithm allowing to model the human body by three cylinders (arms and trunk). Again, the simulations and the measurements show good agreement at 2.45 GHz. In [31], small scale movements of the arms are performed in order to emulate a dynamic channel. In [32], a modal solution of the scattering of a point source by a circular cylinder is proposed and compared to measurements. It is shown that the cylindrical model is acceptable for on-body communications at 915 MHz and 2.45 MHz. However, the high variability of the body shape and the complexity of the scenario make analytical channel modeling not general enough. Measurements are then most commonly used to derive standardized channel models.

2.1.3.1 Narrowband channels

The human body is a complex environment and it requires extensive characterizations of the phenomena involved in the various communication scenarios. Due to inherent mobility, the propagation channel varies with the modifications of the body shape such as breathing, posture or parts of the body movements. The presence of device in close proximity of the body involves antenna-body interaction effects including, near-field coupling, radiation pattern modifications, antenna efficiency degradations, etc.

Path loss

The complex body geometry, the multitude of body shape variation and the numerous propagation paths available in Body Are Networks make difficult to fit measured path losses to a distance related law [33, 34, 35]. This can be easily understood by considering a link between two nodes in front of the torso and a second one with a node in front and the other node in back of the torso. Even if the links have similar lengths, the propagation mechanisms are different and the path gains can be widely different. An uniform path loss with distance model for on-body communications is then impossible to obtain accurately. Despite this, narrowband path losses with distance have been widely studied. The main reason is the easy understanding of the underlying laws and the easy usability and implementation of such formulations. For instance, as reported in [33], in the IEEE 802.15.6 channel model, a function of the distance was used to model the path loss [36]. Other authors considered such Friis based path loss solutions at 2.4 GHz [37, 38]. It has been shown that the path loss along torso and arms shows good fit to analytical solution on a flat lossy medium representing human tissue. Path loss P_{dB} models in decibels are often based on Friis-like formula:

$$P_{\mathrm{dB}} = P_{\mathrm{dB}}^{0} - 10n\log_{10}(d/d_0) + \mathcal{X}_\sigma \tag{2.6}$$

where d is the distance between transmit and receive antenna, n is the path loss exponent and P_{dB}^{0} is the reference path loss at reference distance d_0. $\mathcal{X}_\sigma$ is the shadowing, often modeled by a Gaussian distribution of 0 dB-mean and standard deviation σ. Other path loss formulations have been proposed which are more suited for NLOS links:

$$P_{\mathrm{dB}} = P_{\mathrm{dB}}^{0} - \gamma(d - d_0) + \mathcal{X}_\sigma \tag{2.7}$$

where γ is the path loss decay in dB/m. In [39], measurements have been conducted at 915 MHz and 2.45 GHz. It has been found a path loss decay γ equal to 2.1 dB/cm and 2 dB/cm respectively. On the other hand, [38] showed path losses exponents $n \simeq 3.3$. In [40], path loss exponents have been evaluated at 2.45 GHz and depending on the scenario (around- or on-torso) different values have been obtained ranging from n =2.4 up to 4.5. In [41], an hybrid model has been proposed based on (2.7):

$$P_{\mathrm{dB}} = -10\log_{10}(P_0 e^{-\gamma(d-d_0)} + P_1) + \mathcal{X}_\sigma \tag{2.8}$$

This model comes from the fact that the path loss is due to the main diffraction path around the body for small distances (modeled by the exponential part) while it is defined by the environment for larger distances (P_1 part). It has been shown in [33, 41] that $P_0[\mathrm{dB}] = -25.8$, $\gamma = 2$ dB/cm and $P_1[\mathrm{dB}] = -71.3$ which implies that the effect of the environment is overriding for links larger than 20 cm. $\mathcal{X}_\sigma$ is a lognormal distribution in (2.8).

In [42], path loss has been investigated for fixed links and then, no formulation with distance is derived. This methodology is *scenario-based* and it does not lead to any generalized model. Also, [42] presents averaged path losses for different actions of the user such as standing, walking or running.

Fading Statistics

In (2.6) and (2.7), we introduced the shadowing $\mathcal{X}_\sigma$ as a normal distribution in dB. Fading due to body shadowing has been studied for on-body links in [43] by averaging the small scale fading using a sliding temporal window. It has been shown that body shadowing at 2.45 GHz is well described using a lognormal distribution. It is also shown that shadowing highly depends on the type of body movements. On the other hand, small scale fading has been modeled by the same authors and others [44] using Rice distribution and the Rice K factor. It has been shown that K is high when the body is stationary and drastically decreases when the user becomes mobile within indoor environments. This simply means that fading is low when the user is static while it is high due to movements and multipath components.

However, rather than decompose the signal into body shadowing and small-scale fading, it is generally proposed to model the received signal variations as a single random variable. In the literature, several other distributions have been proposed to model on-body fading: Lognormal

[45, 46] for both stationary and routine activities cases; Rayleigh [47] for large obstructed on-body nodes in indoor environments; Nakagami [46] when the fading is worst than the one predicted by Rayleigh; Weibull [35] has been reported for running and walking cases. There is no consensus on which distribution to use because it is highly dependent on the scenario [33].

Time Dependence

It has been suggested that some movements of the human body are repetitive and that the time variation of the signal can be anticipated. This has a strong importance for the design of communication protocols and error correcting codes. Time dependencies are often studied through the autocorrelation function of time variations of the signal. The understanding of time variations in BANs is limited and found to be due to movements of the limbs [33]. Models are almost always measurement-based and some results can be found in [48, 49].

Periodic signal variations have also been studied in [50] and it was found that body movements caused Doppler spread. An experimental model have been proposed to characterize the power spectrum density which showed some significant harmonics on the Doppler spectra.

2.1.3.2 Wideband channels

A special interest has been given to on-body propagation models in UWB (from 3.1 to 10.6 GHz)[5]. In this frequency band, BAN channel models are based on the understanding of the main propagation mechanisms as presented in Fig. 2.2. A lot of results can be obtained from the theses [39] and [2]. More particularly, path loss formulas (2.6) and (2.7) have been obtained for the first path[45, 49]. Also, in [45], an increase of path loss with frequency has been observed. Power delay profile models have been proposed by giving the path loss of the first tap, power decay, fading statistics but also intertap correlation. In [51], the mean number of paths, between 41 and 66, is provided for indoor environments. In [45], a two-cluster model is proposed for indoor scenarios. In [2], the distribution and the parameters (angles, delay, amplitude) of each cluster are defined using Saleh-Valenzuela models presented in section 2.1.2.

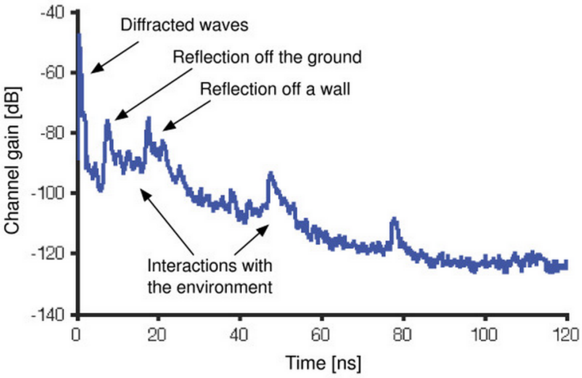

Figure 2.2: Impulse response model. Description of the main propagation mechanisms in on-body propagation. [2]

2.1.4 Off-Body Channels

Early measurements of the propagation between a worn device and an external transmitter have been conducted by [52]. The subject was walking towards and away from the transmitter in order to emulate an LOS and NLOS communication. The measurements were compared to a simulation tool which provided good fit for LOS cases. Statistics showed that Rayleigh and lognormal distributions provide a good fit of the small-scale fading. Multi-antenna off-body propagation has been studied at 868 MHz by [53]. It is shown that body orientation and antenna positioning have a strong influence on the off-body channel. Comparison between 820 MHz and 2.36 GHz has been performed in [35] and it has been observed that the channel was more stable at lower frequencies.

Again, UWB have been studied for off-body communications and multi-slope path loss formulas have been proposed in [54]. In [55], an off-body UWB channel model has been proposed which was really close to the free-space indoor one [33].

2.2 60 GHz Body Area Networks

2.2.1 Electric Properties of human body tissues

The human body is considered as a highly heterogeneous and irregular medium from an electromagnetic point of view. The body is made up several layers of skin, muscle, blood, ... and each layer possesses its own electrical properties. This creates complex electric field distributions at the tissue scale. However, in this thesis, only effects of electromagnetic fields around the human body are of interest and not inside it.
Biological tissues are mathematically described by lossy dielectric media. Such media are described by their complex permittivity ε which depends on the angular frequency ω:

$$\varepsilon(\omega) = \varepsilon'(\omega) - j\frac{\sigma(\omega)}{\omega} \tag{2.9}$$

where σ is the conductivity and ε' is the real part of permittivity. It is important to notice that the magnetic permeability of tissues is equal to the permeability of free space μ_0. [3] references the electric properties of most of the human tissues for frequencies ranging from 10 Hz to 100 GHz. The real part of the permittivity and the conductivity of the human skin are presented over the V-band (from 50 to 75 GHz) in Fig. 2.3.

The attenuation of the electric field E inside a lossy dielectric tissue can be mathematically described by $|E|^2 = e^{-2\alpha z}$ where

$$\alpha = \omega\sqrt{\frac{\mu_0\varepsilon}{2}}\left[\sqrt{1+(\frac{\sigma}{\omega\varepsilon})^2} - 1\right]^{1/2} \tag{2.10}$$

and z is the distance inside the medium. The skin depth $1/\alpha$ is about 0.5 mm at 60 GHz while it is about 2 cm at 3 GHz. This implies one major conclusion for 60 GHz communications: the body model can be limited to one single layer.

2.2.2 Propagation Models and Results

Since human blockage has been identified as one of the most critical aspect of 60 GHz indoor communications [56], several groups have been

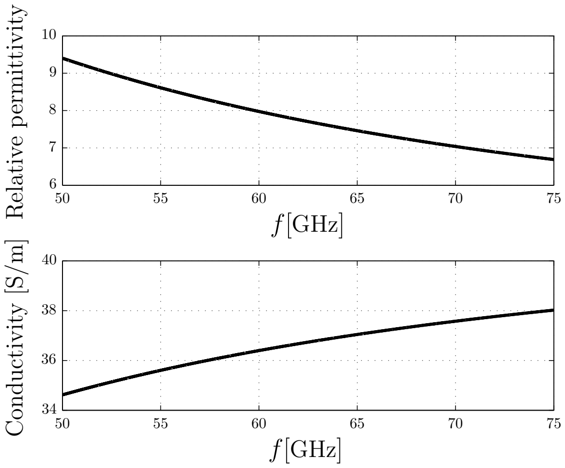

Figure 2.3: Permittivity and conductivity of the human skin over the V-band [3].

focused on it in order to be taken into account in the IEEE 802.11ad standard. In [57], a combination of a random walk model and knife edge diffraction has been intended to describe human movements. This has been used in order to provide probability of blockage of clusters which can be easily implemented in the standard. In [58], measurements have been conducted in an indoor environment aiming to determine the maximum attenuation caused by human blockage. It has been shown that losses with and without body blockage can exceed 40 dB. Further, in [59], link blockage probability has been assessed for a ceiling-mounted transmitter. As expected, it has been shown that the blockage probability of the line-of-sight increase when bodies move towards the receiver and when human density increases. The channel capacity has been assessed accordingly. More recently, cylindrical models of the human body have been proposed and studied in [60]. It is shown that the human body can be approximated by a PEC cylinder and no significant difference has been observed between circular and elliptic cylinders. Simulations have shown a Doppler shift due to human activity which has been easily suppressed using directive antennas.

Analytical models for 60 GHz Body Area Networks have been obtained by using greatly simplified body geometries [16]. In [61], a flat body model is proposed, leading to Norton's equations. It is shown that, in a line-of-sight configuration, with the antenna located a few millimeters away from the body, the received power in dB can be approximated by a logarithmic decay with distance. The path loss exponent is about 3.4 for vertical polarization and about 4 for horizontal polarization. These values have been experimentally verified on a flat skin-equivalent phantom by [61]. A generalization of this last paper has been used in [62] in order to study the impact of clothing on the propagation. It has been shown that different layers and types of clothing have a negligible effect on the path loss. Further, the same group of authors introduced an electro-textile with specific electric properties (high conductivity) allowing a significant improvement of the path loss [63].

Numerical simulations have also been used to study the channel for 60 GHz Body centric communications. In [17], ray tracing algorithm had been used to model soldier-to-soldier communication scenarios in battlefield operations. It has been shown that the signal direction of arrival spread was increasing when soldiers goes from outdoor to indoor environments. Further, recent progresses in numerical phantoms of the human body have allowed one to develop models with sub-millimeter meshes [64]. Also the development of huge numerical resources have made possible to use Finite-Difference Time-Domain method (FDTD) for 60 GHz BANs. Since we are dealing with a electrically large problem, parallelized simulations have been proposed in [64]. This method has the advantage to give the received power for a realistic geometry. However, the major drawback of FDTD in such case is the need for enormous calculation resources. In [64], the number of cells to discretize a human phantom is evaluated to about 10^{11}. These results are interesting and give a range of values for the expected received power on a specific link. However, high received signal variability is introduced by the human body shape, size, asperity, roughness, but also by the small and large movements or by the different positions of the body.

Later, scenario-based models have been proposed by a research group of the *University of Birmingham*. In [65], measurements have been conducted on five antenna positions and heights using body-mounted monopoles. The antenna positions were the followings: head, arm, chest, wrist and waist. Temporal samples were measured and it was proposed to study the median and the interquartile ranges (IQRs) of path loss. The eight links under study are summarized in Table 2.1. In [65], information about distances are not available. Comparison with the previous section is then complicated. The longest links is Head-Wrist and the shortest are Chest-Head and Head-Arm. It is not possible to draw any conclusion since these three links have about the same median. However, it is interesting to study the IQR of each link. It can be seen that the lowest one is the Arm-Wrist link which is always in a LOS situation. The second range of IQR values is Head-Wrist, Waist-Chest and Chest-Arm which can be affected by breathing or small movements like to on-torso links studied in the previous section. Finally, the Chest-Head, Head-Arm, Chest-Wrist and Waist-Wrist have the largest IQR which is mainly due to shadowing by large movements such as arm movement, etc. This creates situations with high LOS and high NLOS configurations which create high disparities in the received power.

[66] discusses the impact of polarization and directivity in the same scenario-based on-body set-up but waveguide antennas are considered

Table 2.1: Path Loss parameters in a Scenario-based model

Link	Median [dB]	IQR [dB]
Arm-Wrist	-57.3	4.8
Chest-Head	-64.2	15.9
Head-Arm	-67.1	16.6
Head-Wrist	-69.0	9.2
Waist-Chest	-70.5	8.4
Chest-Arm	-75.4	8.9
Chest-Wrist	-80.5	13.7
Waist-Wrist	-88.2	13.8

instead of monopoles. Using directive waveguides drives out different conclusions. Some paths can be helped by directivity while others are adversely affected. For instance, the chest-waist link can be increased by 25 dB using vertical polarized waveguides instead of monopoles while the head-wrist channel is decreased by 20 dB. These results shows that the directivity impacts the budget link as expected. However, it should be used precociously because increasing the gain on a link may decrease it on an other one. More recently, [67] has completed [66] with extra-measurements. Antenna polarization effect is discussed and compared to the monopole antenna. It is noticed that horns provide 10 dB less path loss (at least) in the case of channels with restricted movements. In other channels (with larger antenna movements), monopoles provide about the same path loss as horns. The IQR with guides is also in general similar to the monopole one except in the case of arm wrist link where it is considerably lower. In [67], the authors conclude that the choice between a monopole or a horn antenna will depend on the communication link. Hence, horn antennas will be preferred for quasi-stationary links.

Further, in [65], it is proposed to split up time-variations into two components: short-term and long-term fading. This has been proposed to model a user making everyday activities. Measurements show high variability of the distribution shapes depending on the considered link. The authors proposed to categorize links depending on the distribution shape. However, it seemed that links in a same group can be highly different and it is not obvious to relate them with a physical parameter. On the other hand, it shown that short-term data can be modelled by the Cauchy-Lorentz distribution CL with the zero position parameter and the scale parameter γ:

$$\mathrm{CL}(x,\gamma) = \frac{\gamma/\pi}{x^2+\gamma^2} \tag{2.11}$$

where γ is estimated as the half of the IQR of short-term fading. It is shown that all links have the same distribution shape. Again, the measured distribution are not symmetrical and the lower tail of the distribution is then slightly underestimated. However, the Cauchy-Lorentz distribution had never been reported in radiowave propagation and authors affirms that the nature of this distribution needs further investigation for on-body short-term fading.

In this scope, this thesis contributes to a better understanding of 60 GHz Body Area Networks propagation. Analytical and numerical models and experimental validations are proposed for the characterization of on-, off- and near-body propagation characterization.

2.3 Conclusion

Very few contributions have been made in the field of 60 GHz Body Area Networks propagation. More particularly, there is almost no results regarding off-body or even near-body propagation. Also, experimental results of on-body propagation have been proposed but there is no physical understanding of the underlying propagation mechanisms. Hence, in this thesis, a special effort is given to analytical modeling and to physical understanding of the propagation. Also, this thesis proposes to fill in the dips in the state-of-the-art knowing as the off- and near-body propagations and a deeper study of on-body propagation. The proposed models allow to simulate the propagation in controlled conditions in order to study the effect of different parameters. In conclusion, the results obtained in this thesis are more general than the ones found in the literature since more scenarios can be modeled but there are less accurate due the simplified considered geometries.

Chapter 3

Off-Body Propagation and Communication

Contents

3.1 Objectives and Scenario definition

The main goal of this chapter is to propose an indoor off-body channel model and to illustrate it by presenting some simulation results. To derive such channel model, it is proposed to split up the problem into two components: the body impact and the effect of the environment.

First, a ray-based indoor channel model has to be chosen and implemented in order to simulate the effect of the environment on the channel. The most commonly used channel model for 60 GHz indoor communications has been developed by *Maltsev et al.* and standardized as IEEE 802.11ad [56]. Let us briefly recall the main structure and parameters of the channel impulse response h in this model:

$$\begin{aligned} &h(t, \phi_{\mathrm{Tx}}, \theta_{\mathrm{Tx}}, \phi_{\mathrm{Rx}}, \theta_{\mathrm{Rx}}) = \sum_i \mathbf{H}^{(i)} \times \\ &C^{(i)}(t - T^{(i)}, \phi_{\mathrm{Tx}} - \Phi_{\mathrm{Tx}}^{(i)}, \theta_{\mathrm{Tx}} - \Theta_{\mathrm{Tx}}^{(i)}, \phi_{\mathrm{Rx}} - \Phi_{\mathrm{Rx}}^{(i)}, \theta_{\mathrm{Rx}} - \Theta_{\mathrm{Rx}}^{(i)}) \end{aligned} \tag{3.1}$$

with $C^{(i)}$ is the impulse response relative to the i^{th} cluster:

$$\begin{aligned} &C^{(i)}(t, \phi_{\mathrm{Tx}}, \theta_{\mathrm{Tx}}, \phi_{\mathrm{Rx}}, \theta_{\mathrm{Rx}}) = \sum_k \alpha_{(i,k)} \delta(t - \tau^{(i,k)}) \times \\ &\delta(\phi_{\mathrm{Tx}} - \phi_{\mathrm{Tx}}^{(i,k)}) \delta(\theta_{\mathrm{Tx}} - \theta_{\mathrm{Tx}}^{(i,k)}) \delta(\phi_{\mathrm{Rx}} - \phi_{\mathrm{Rx}}^{(i,k)}) \delta(\theta_{\mathrm{Rx}} - \theta_{\mathrm{Rx}}^{(i,k)}) \end{aligned} \tag{3.2}$$

where,

- $t, \tau, \phi_{\mathrm{Tx}}, \theta_{\mathrm{Tx}}, \phi_{\mathrm{Rx}}, \theta_{\mathrm{Rx}}$ are, respectively, time, delay, azimuth and elevation angles at the transmitter (Tx) and receiver (Rx).
- $\mathbf{H}^{(i)}$ is the i^{th} 2x2 polarization matrix of the cluster gains.
- $T^{(i)}, \Phi_{\mathrm{Tx}}^{(i)}, \Theta_{\mathrm{Tx}}^{(i)}, \Phi_{\mathrm{Rx}}^{(i)}, \Theta_{\mathrm{Rx}}^{(i)}$ are the temporal and angular coordinates of i^{th} cluster.

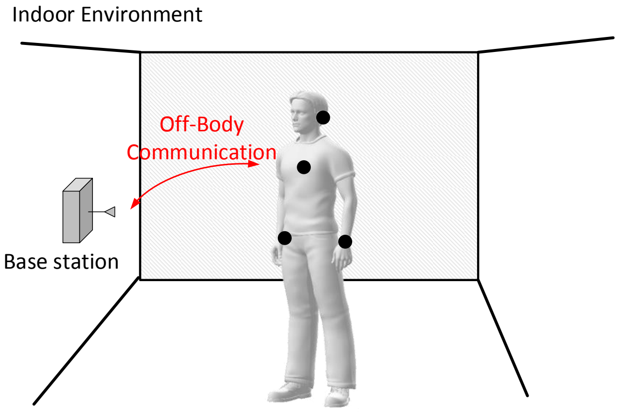

Figure 3.1: Schema of an Off-Body communication in an indoor environment.

- $\alpha_{(i,k)}$ is the magnitude of the k^{th} ray of the i^{th} cluster.

Since this channel is already available, it can be used and modified in order to take into account the body presence. The idea is to develop an analytical, accurate and fast-computation off-body propagation model and to insert it into the IEEE 802.11ad. To do so, we propose to study the problem of the diffraction of a plane wave by a circular cylinder. Using these propagation results, each wave of the indoor channel model has to be modified following the geometry presented in Fig. 3.2(a). The result will lead to the indoor off-body propagation model.

The reaming of the chapter is then organized as follows: in section 3.2, the scattering of the plane wave by a cylinder is simulated and

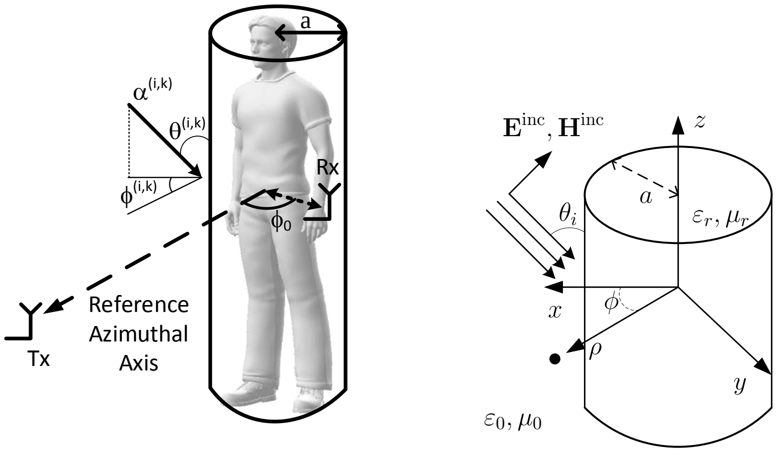

(a) (b)

Figure 3.2: The human body is modeled by a circular cylinder of radius a. On the left, the receiver (Rx) is located at azimuth angle ϕ_0 with respect to the reference axis drawn between the transmitter (Tx) and the center of the cylinder. On the right, the Off-Body geometry is presented. The electric (magnetic) field lies in the xz plane for TM (TE) polarization.

experimentally assessed. Then, the indoor off-body channel model is generated, simulated and experimentally validated in section 3.3. Finally, in section 3.4, the proposed model is used in order to study the performances of the communication in a WiGig standard communication. The bit error rate is evaluated and spatial and polarization diversity are investigated with respect to the mean channel attenuation and the Rician K-factor. Conclusions are drawn in section 3.5

3.2 Propagation Model assessment

The propagation model proposed in this chapter is derived from the diffraction of a plane wave by a circular cylinder. This geometry for modeling the human body is over-simplified but it allows us to calculate analytically the scattered electric field in an efficient computational way.

3.2.1 Analytical model

3.2.1.1 Problem definition

The geometry definition is drawn in Fig. 3.2(b). The incident electric field $\mathbf{E}_{\text{inc}}$ for TM polarization is defined as:

$$\mathbf{E}^{\text{inc}} = E_0(\cos\theta_i\ \hat{x} + \sin\theta_i\ \hat{z})\ e^{jk_0 x \sin\theta_i} e^{jk_0 z \cos\theta_i} \tag{3.3}$$

where E_0 is the electric field amplitude, $k_0 = \omega/c$ is the free-space wavenumber, c is the speed of light and θ_i the elevation angle.
The magnetic field $\mathbf{H}_{\text{inc}}$ for TE polarization is defined as:

$$\mathbf{H}^{\text{inc}} = H_0(\cos\theta_i\ \hat{x} + \sin\theta_i\ \hat{z})\ e^{jk_0 x \sin\theta_i} e^{jk_0 z \cos\theta_i} \tag{3.4}$$

where H_0 is the magnetic field amplitude. The total electric field $\mathbf{E}^{\text{tot}}$ around the cylinder is:

$$\mathbf{E}^{\text{tot}} = \mathbf{E}^{\text{inc}} + \mathbf{E}^{\text{s}} \tag{3.5}$$

where $\mathbf{E}^{\text{s}}$ is the scattered field.

Geometrically and as depicted in Fig. 3.3, the shadow boundary between the lit and shadow regions is defined by:

$$\phi_{\text{bound}} = \frac{\pi}{2} + \cos^{-1}(\frac{a}{\rho}) \tag{3.6}$$

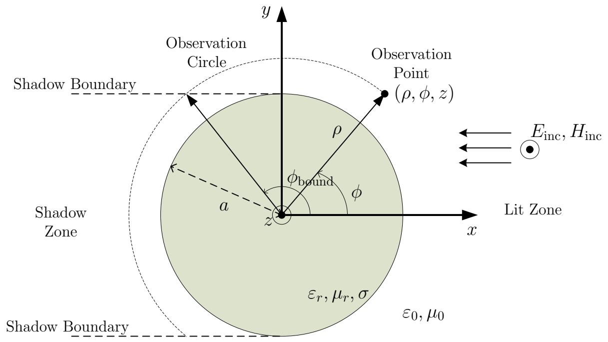

Figure 3.3: 2D view of the problem geometry.

The lit region is defined by $\phi < \phi_{\text{bound}}$ and the shadow region by $\phi > \phi_{\text{bound}}$. It the following, it will be assumed that $a \simeq \rho$ which leads to $\phi_{\text{bound}} \simeq \pi/2$. The equations will be developed independently for the lit and shadow regions.

3.2.1.2 TM polarization

The exact solution of the scattering of a plane wave by a dielectric cylinder is given in a lossless case in [68] and can be generalized to a lossy one:

$$\begin{aligned}
E^{\text{s}}_{\rho} &= -jE_0 \cos\theta_i e^{jkz\cos\theta_i} \sum_{n=-\infty}^{+\infty} j^n a_n H_n^{(2)'}(k\rho\sin\theta_i) e^{-jn\phi} \\
E^{\text{s}}_{\phi} &= -jE_0 \frac{\cot\theta_i}{k\rho} e^{jkz\cos\theta_i} \sum_{n=-\infty}^{+\infty} n j^{n-1} a_n H_n^{(2)}(k\rho\sin\theta_i) e^{-jn\phi} \\
E^{\text{s}}_{z} &= E_0 \sin\theta_i e^{jkz\cos\theta_i} \sum_{n=-\infty}^{+\infty} j^n a_n H_n^{(2)}(k\rho\sin\theta_i) e^{-jn\phi}
\end{aligned} \tag{3.7}$$

where J_n and $H_n^{(2)}$ are, respectively, Bessel functions of the first kind and second order Hankel functions [69]. It can be shown that a_n can be written in the high frequency range (by assuming that $ka \gg 1$) [70] as:

$$a_n = -\frac{J_n'(ka\sin\theta_i) + QJ_n(ka\sin\theta_i)}{H_n^{(2)'}(ka\sin\theta_i) + QH_n^{(2)}(ka\sin\theta_i)} \tag{3.8}$$

where $Q = j\eta$, $\eta = \sqrt{\varepsilon_r/\mu_r}$ is the normalized admittance with respect to the free space admittance $\sqrt{\varepsilon_0/\mu_0}$ [71] and $k = k_0$.

In (3.7), at high frequency, the series slowly converges and the number of terms required for convergence is too large to allow a fast computation. To speed up convergence, we propose a simplified model where the electric field is approximated by a creeping wave in the shadow region and by Geometrical Optics in the lit one.

Lit Region As can be seen in [72], Geometrical Optics (GO) can be used to solve diffraction problems in the lit region at high frequencies. As shown in Figure 3.4, the total field is then calculated by the sum of the incident and reflected waves. Equation (3.5) is modified by introducing the reflection matrix $\overline{\overline{R}}$ and reflected wave $\mathbf{E}^{\mathrm{refl}}$ as:

$$\mathbf{E}^{\mathrm{tot}} = \mathbf{E}^{\mathrm{inc}} + \overline{\overline{R}}\,\mathbf{E}^{\mathrm{refl}} \tag{3.9}$$

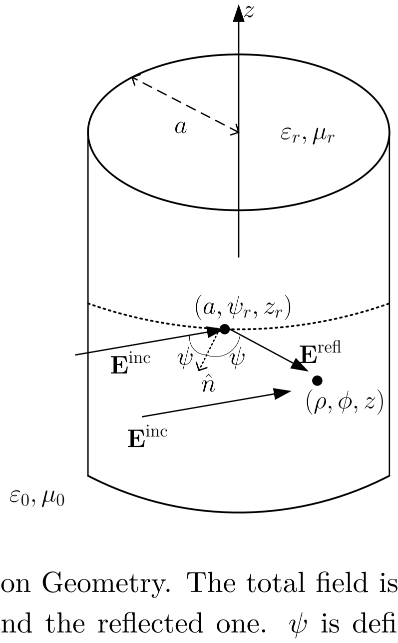

Figure 3.4: Lit region Geometry. The total field is given by the sum of the incident field and the reflected one. ψ is defined as the reflection angle and $\hat{n}$ is the normal vector at the reflection point.

At 60 GHz, the cylinder modeling the body is electrically large ($ka \gg 1$), the scattering surface can be approached by an infinite plane. The reflection matrix is then given by:

$$\overline{\overline{R}} = \begin{pmatrix} R_\rho & 0 & 0 \\ 0 & R_\phi & 0 \\ 0 & 0 & R_z \end{pmatrix} \tag{3.10}$$

with

$$R_z = R_\rho = \frac{\sin\psi - \sin\psi_t}{\sin\psi + \sin\psi_t} \text{ and } R_\phi = \frac{\tan\psi - \tan\psi_t}{\tan\psi + \tan\psi_t}. \tag{3.11}$$

In those equations, ψ is the reflection angle and $\psi_t = \arcsin(\sin(\psi)/\sqrt{\varepsilon_r})$ is the transmission angle. The reflected wave is obtained by introducing a propagation term :

$$\mathbf{E}^{\text{refl}} = \mathbf{E}^{\text{inc}}(a, \psi_r, z_r)\sqrt{\frac{\rho_r}{\rho_r + s_r}}e^{-jks_r} \tag{3.12}$$

where $\rho_r = \frac{a}{2}\cos\psi$ and s_r is the distance between the observation point (ρ, ψ, z) and the reflection point (a, ψ_r, z_r).

Shadow Region By using Watson's transformation [73] on (3.7), the total field in the shadow region $\phi > \pi/2$ becomes:

$$\begin{aligned} E_\rho^{\text{tot}} &= -\frac{2\pi}{m} jE_0 \cos\theta_i e^{jkz\cos\theta_i} \sum_s j^{\upsilon_s} \tilde{a}_{\upsilon_s} {W_2}'(\tau_s)\Phi_{\upsilon_s}(\phi) \\ E_\phi^{\text{tot}} &= -2\pi jE_0 \frac{\cot\theta_i}{k\rho} e^{jkz\cos\theta_i} \sum_s \upsilon_s j^{\upsilon_s - 1} \tilde{a}_{\upsilon_s} W_2(\tau_s)\Phi_{\upsilon_s}(\phi) \\ E_z^{\text{tot}} &= 2\pi E_0 \sin\theta_i e^{jkz\cos\theta_i} \sum_s j^{\upsilon_s} \tilde{a}_{\upsilon_s} W_2(\tau_s)\Phi_{\upsilon_s}(\phi) \end{aligned} \tag{3.13}$$

where $m = (ka\sin\theta_i)^{1/3}$, $\upsilon_s = ka\sin\theta_i + m\tau_s$ and:

$$\begin{aligned} \Phi_\upsilon(\phi) &= \frac{\cos(\upsilon(\phi - \pi))}{\sin(\upsilon\pi)} \\ \tilde{a}_{\upsilon_s} &= \frac{A'(\tau_s) - qA(\tau_s)}{\tau_s W_2(\tau_s) - qW_2'(\tau_s)} \\ h &= \frac{k}{m}\sin\theta_i(\rho - a). \end{aligned} \tag{3.14}$$

In these equations, $q = mQ$ and the τ_s are defined by:

$$W_2'(\tau_s) - qW_2(\tau_s) = 0 \tag{3.15}$$

$A(z)$ is the Airy function of the first kind and $W_2(z) = 2e^{j\pi/6}A(e^{j4\pi/3}z)$. Since 60 GHz numerically implies the condition on the imaginary parts $|\mathrm{Im}(\upsilon_1)| \ll |\mathrm{Im}(\upsilon_s)|$ for $s > 2$, the sum (3.13) can be approximated by:

$$\begin{aligned}
E_\rho^{\mathrm{tot}} &= -\frac{2\pi}{m} jE_0 \cos\theta_i e^{jkz\cos\theta_i} j^{\upsilon_1+1} \tilde{a}_{\upsilon_1} W_2{}'(\tau_1) e^{-j\upsilon_1\phi} \\
E_\phi^{\mathrm{tot}} &= -2\pi jE_0 \frac{\cot\theta_i}{k\rho} e^{jkz\cos\theta_i} \upsilon_1 j^{\upsilon_1} \tilde{a}_{\upsilon_1} W_2(\tau_1) e^{-j\upsilon_1\phi} \\
E_z^{\mathrm{tot}} &= 2\pi E_0 \sin\theta_i e^{jkz\cos\theta_i} j^{\upsilon_1+1} \tilde{a}_{\upsilon_1} W_2(\tau_1) e^{-j\upsilon_1\phi}
\end{aligned} \tag{3.16}$$

by using $\Phi_{\upsilon_s}(\phi) \simeq je^{-j\upsilon_s\phi}$. Equation (3.16) gives the creeping wave solution in the shadow zone. The path gain of the creeping wave can be deduced by introducing the power $P = 20\log_{10}|E|$ expressed in dB and noting that $|E| \propto e^{\mathrm{Im}(\tau_1)\phi}$:

$$P_\gamma = P_\gamma^{\pi/2} + n^{\mathrm{TM}}(\pi/2 - \phi) \tag{3.17}$$

where $\gamma = \rho, \phi, z$ and $P_\gamma^{\pi/2}$ is the power at the boundary of the shadow zone $\phi = \pi/2$ for the γ component. It is remarkable that the path gain factor n^{TM} is the same for each component of the electric field. The power P_{tot} for the total field can also be easily deduced:

$$P_{\mathrm{tot}} = P_{\mathrm{tot}}^{\pi/2} + n^{\mathrm{TM}}(\pi/2 - \phi) \tag{3.18}$$

The path gain factor can be derived from (3.16):

$$n^{\mathrm{TM}} = 20\log_{10}(e)|\mathrm{Im}(\tau_1)|m \tag{3.19}$$

3.2.1.3 TE polarization

For TE polarization, the incident electric field is:

$$\begin{aligned}
E_\rho^{\mathrm{inc}} &= -\frac{H_0}{c\varepsilon_0} \sin\phi \; e^{jkz\cos\theta_i} e^{jkx\sin\theta_i} \\
E_\phi^{\mathrm{inc}} &= -\frac{H_0}{c\varepsilon_0} \cos\phi \; e^{jkz\cos\theta_i} e^{jkx\sin\theta_i} \\
E_z^{\mathrm{inc}} &= 0
\end{aligned} \tag{3.20}$$

The exact solution can also be easily obtained by solving the boundary conditions problem in cylindrical coordinates:

$$\begin{aligned}
E^{\mathrm{s}}_{\rho} &= -j\frac{H_0}{\omega\varepsilon\rho}\frac{e^{-jkz\cos\theta_i}}{\sin\theta_i}\sum_{n=-\infty}^{+\infty} nj^{n-1}b_nH_n^{(2)}(k\rho\sin\theta_i)e^{-jn\phi} \\
E^{\mathrm{s}}_{\phi} &= j\sqrt{\frac{\mu}{\varepsilon}}H_0e^{-jkz\cos\theta_i}\sum_{n=-\infty}^{+\infty} j^nb_nH_n^{(2)\prime}(k\rho\sin\theta_i)e^{-jn\phi} \\
E^{\mathrm{s}}_{z} &= 0
\end{aligned} \tag{3.21}$$

where, by using the high frequency assumption:

$$b_n = -\frac{QJ_n'(ka\sin\theta_i) + J_n(ka\sin\theta_i)}{QH_n^{(2)\prime}(ka\sin\theta_i) + H_n^{(2)}(ka\sin\theta_i)} \tag{3.22}$$

Equations (3.5) is used to get the total field for each component. The same methodology as used in section 3.2.1.2 is then carried out to speed up convergence.

Lit Region In the lit region, equations (3.9) - (3.12) are used by defining the incident field with (3.20).

Shadow region By applying Watson's transformation, the creeping wave expression of the total field in the shadow region is:

$$\begin{aligned}
E^{\mathrm{tot}}_{\rho} &= \quad -j\frac{H_0}{\omega\varepsilon_0\rho}\frac{e^{-jkz\cos\theta_i}}{\sin\theta_i}2\pi\upsilon_1'j^{\upsilon_1'}\tilde{b}_{\upsilon_1'}W_2(\tau_1'-h)e^{-j\upsilon_1'\phi} \\
E^{\mathrm{tot}}_{\phi} &= \quad j\sqrt{\frac{\mu_0}{\varepsilon_0}}H_0e^{-jkz\cos\theta_i}\frac{2\pi}{m}j^{\upsilon_1'+1}\tilde{b}_{\upsilon_1'}W_2'(\tau_1'-h)e^{-j\upsilon_1'\phi} \\
E^{\mathrm{tot}}_{z} &= 0
\end{aligned} \tag{3.23}$$

where $\upsilon_1' = ka\sin\theta_i + m\tau_1'$ and τ_1' is the first zero of:

$$qW_2'(\tau_1') - W_2(\tau_1') = 0 \tag{3.24}$$

and

$$\tilde{b}_{\upsilon_1'} = \frac{qA'(\tau_1') - A(\tau_1')}{q\tau_1'W_2(\tau_1') - W_2'(\tau_1')}. \tag{3.25}$$

These equations give the path gain:

$$P_{\text{tot}} = P_{\text{tot}}^{\pi/2} + n^{\text{TE}}(\pi/2 - \phi) \tag{3.26}$$

where $P_{\text{tot}} = 20\log_{10}|\mathbf{E}^{\text{tot}}|$ in dB, and

$$n^{\text{TE}} = 20\log_{10}(e)|\text{Im}(\tau_1')|m. \tag{3.27}$$

The path gain of each component of the electric field can be rewritten as (3.17) by using n^{TE} for the path gain

3.2.2 Numerical results

Normal Incidence The validity of the model developed in section 3.2.1 and the split into two regions (lit and shadow) are first compared for normal incidence ($\theta_i = \pi/2$) TM polarization. The exact solution (3.7) is shown in Fig. 3.5 for both PEC and human skin cases. In the following simulations, the incident electric field magnitude has been normalized to 1 V/m. In the top side of Fig. 3.5, it can be observed that the model is very accurate. The exact solution (3.7) needs about one thousand terms to converge while the creeping wave solution (3.16) only needs one term. The same conclusion can be drawn with the bottom side of Fig. 3.5 where the model is compared with the exact solution for a cylinder filled with the dielectric properties of skin at 60 GHz. It can be observed that the accuracy of the GO modeling decreases around the shadow boundary.

The TE mode can be split into in two components: ρ and ϕ. As can be observed in Fig. 3.6, the ϕ component of the creeping wave is negligible in the shadow zone. The dielectric and PEC cylinders are also compared with the model for TE polarization in Fig. 3.6(b). As seen in Fig. 3.6, the PEC cylinder gives different path gains than the human skin for the TE case. Fig. 3.5 and 3.6 show an interference pattern in the lit region as expected [72]. The local maxima and minima are due to constructive and destructive interference between the direct and reflected rays on the cylinder. In the shadow region, the path gain approximation shows perfect fitting. This validates the fact that the first

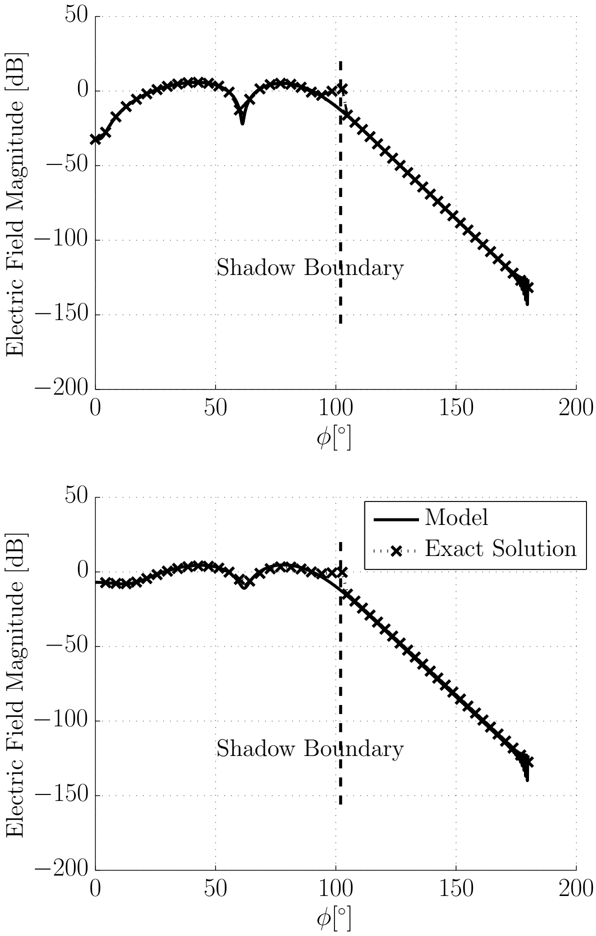

Figure 3.5: TM mode with $f = 60$ GHz, $a = 0.2$ m and $\rho = 0.205$ m. On the top side, the PEC Cylinder solution and on the bottom side, the cylinder with human skin properties one.

creeping wave mode dominates at 60 GHz. The impact of the creeping wave mode coming from the other side of the cylinder ($\phi < 0$) can be observed with the exact solutions around $\phi = 180\,^\circ$ where an interference pattern appears. Given the power level reached for those values of ϕ, this creeping wave mode can be neglected.

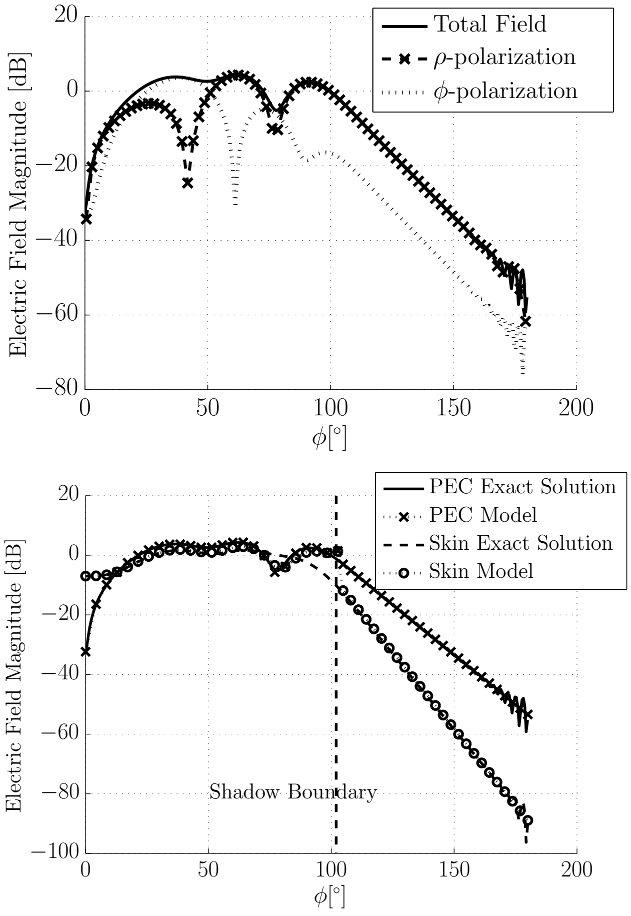

Figure 3.6: TE mode with $f = 60$ GHz, $a = 0.2$ m and $\rho = 0.205$ m. On the top side, the PEC Cylinder solution components comparison and on the bottom side, the cylinder with human skin properties one and PEC cylinder comparison.

Creeping waves path gains Two configurations are under study: the perfectly conducting cylinder (PEC) and the dielectric cylinder having the electric properties of the human skin [3]($\varepsilon_r' = 7.9753$, $\sigma = 36.397$ S/m). The first zeroes τ_1, τ_1' are computed from (3.15) and (3.24). In the TM case, the dependence of τ_1 with the elevation angle

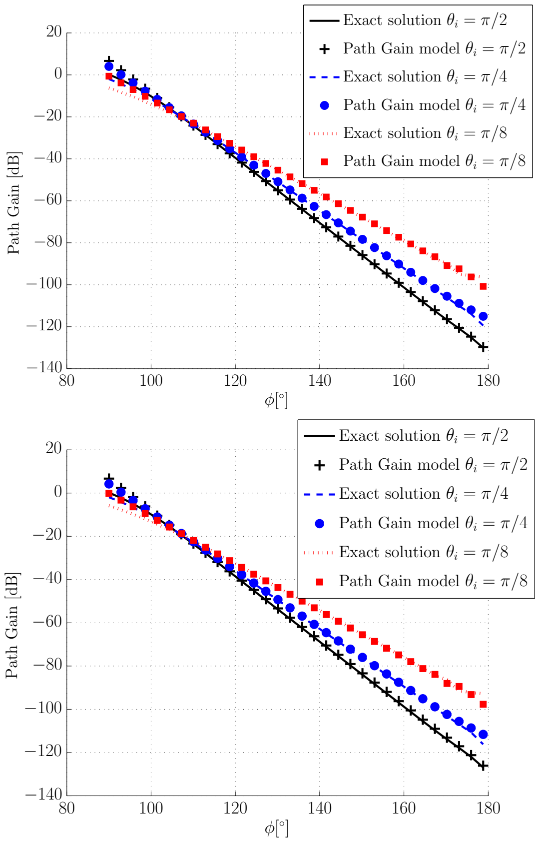

Figure 3.7: Total Field in the shadow zone for TM polarization with $f = 60$ GHz, $a = 20$ cm and $\rho = 20.5$ cm. On the upper side, the PEC Cylinder solution and on the bottom side, the cylinder with human skin properties one.

θ_i is negligible. The solution of (3.15) gives $\tau_1 = 1.17 - j2.025$ for the PEC cylinder, and $\tau_1 = 1.14 - j1.97$ for the dielectric case. As can be seen in Figures 3.7 (a) and (b), the creeping wave model fits the exact solution in the PEC and dielectric cases. The magnitudes have been normalized in order to have unitary incident electric field magnitude.

Figures 3.8 (a) and (b) present the path gain for TE polarization for different values of θ_i. It can be seen that the creeping wave model fits

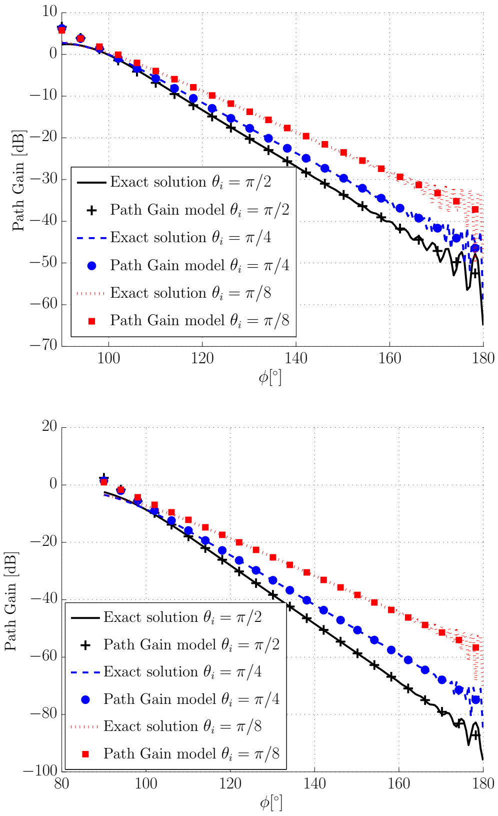

Figure 3.8: Total Field in the shadow zone for TE polarization with $f = 60$ GHz, $a = 20$ cm and $\rho = 20.5$ cm. On the upper side, the PEC Cylinder solution and on the bottom side, the cylinder with human skin properties one.

the exact solution in both cases. In the PEC case, $\tau_1' = 0.51 - j0.88$ does not depend on θ_i. In the dielectric case, the variation of τ_1' with θ_i has to be taken into account.

Table 3.1 summarizes the path gain factors in [dB/cm] for different values of the radius a and elevation angle θ_i. It is worth noting that the path gain factor decreases with decreasing elevation angle θ_i. This fact can be interpreted geometrically. The cylinder sees a plane wave with a normal incidence with a lower frequency $f \longrightarrow f \sin\theta_i$. At lower

Table 3.1: Gains $(n^{\mathrm{TM}}, n^{\mathrm{TE}})$ in [dB/cm] for a PEC cylinder and a dielectric cylinder filled with the electric properties of the human skin.

		θ_i[rad]			
PEC		$\pi/2$	$\pi/4$	$\pi/6$	$\pi/8$
a[cm]	15	(5.34,2.32)	(4.75,2.07)	(4.23,1.84)	(3.87,1.69)
	20	(4.40,1.92)	(3.92,1.71)	(3.50,1.52)	(3.20,1.39)
	25	(3.80,1.65)	(3.38,1.47)	(3.01,1.31)	(2.76,1.20)
	30	(3.36,1.46)	(2.99,1.30)	(2.67,1.16)	(2.44,1.06)
Dielectric		$\pi/2$	$\pi/4$	$\pi/6$	$\pi/8$
a[cm]	15	(5.20,3.40)	(4.61,2.89)	(4.10,2.47)	(3.73,2.19)
	20	(4.30,2.91)	(3.82,2.50)	(3.39,2.11)	(3.09,1.87)
	25	(3.71,2.58)	(3.30,2.20)	(2.93,1.87)	(2.67,1.66)
	30	(3.29,2.34)	(2.92,2.00)	(2.60,1.70)	(2.37,1.50)

frequency, creeping wave attenuation is lower.

This analysis gives some useful insights regarding BAN applications. To improve off-body communications in terms of path gain using creeping wave modes, remote base stations should be located on the ceiling in order to minimize the elevation angle. This solution will improve the link budget of off-body communication.

3.2.3 Experimental Results

To assess the validity of the proposed propagation model, two measurement campaigns have been conducted. The first one has been realized using a perfectly conducting (PEC) cylinder in order to precisely verify the theoretical path gains. First, these path gains have been experimentally studied with for normal incidence for two distances between the cylinder and the receive antenna. Then, the path gains have been assessed for three elevation angles. The second campaign has been conducted on a human. Its purpose was to evaluate the validity of the model to emulate a real body though it has been developed for a cylinder.

Table 3.2: Spatial parameters values

Symbol	Value
a	0.2 m
d	1.92 m
ϕ	from 90 ° to 180 °
Angular Step $\Delta\phi$	5 ° (or 10 °)

3.2.3.1 PEC Measurement Campaign

The first experimental campaign has been done on a convex perfectly conducting cylinder (PEC). This campaign aims at having a very accurate measurement of the path gain around the cylinder and validating precisely the creeping wave model.

Experimental set-up The experimental geometry and the measurement set-up are presented in Fig. 3.9(a) and 3.9(b). The theoretical path gain has been verified by conducting measurements using an *Agilent E8361C VNA* in an anechoic chamber. U-band horn antennas (shown in Fig.3.10) were used with a beamwidth of 10 ° and a gain of 20 dB. The horn antennas have an aperture size of 3 cm x 2.3 cm. This antenna is well suited for such measurement since it increases the dynamic range and reduces the effect of the multipath components. The effect of the horn antenna is to keep almost only the power of the creeping wave of around the cylinder.

As can be observed in Fig. 3.9(a), the Tx horn antenna is located far from the cylinder to obtain a plane wave illumination. The Rx horn antenna is located tangentially to the cylinder to maximize the amount of power received from the creeping wave. Since the antenna is fixed to the cylinder, the antenna has no effect on the angular behaviour of the model and it allows to measure only the phenomenon described by the model. The distance Δr is defined from the middle of the horn antenna and δr defines the distance between the cylinder and the antenna. The parameters are summarized in Table 3.2. The cylinder has a height of 1.2 m and the horn antennas are placed at middle height. To discriminate the time of arrival of the creeping wave between two spatial positions with $\Delta\phi = 10^\circ$, a 10 GHz bandwidth is selected. The frequency step is chosen in such a way that the length of the signal impulse response is 0.015 μs which is equivalent to a propagation length

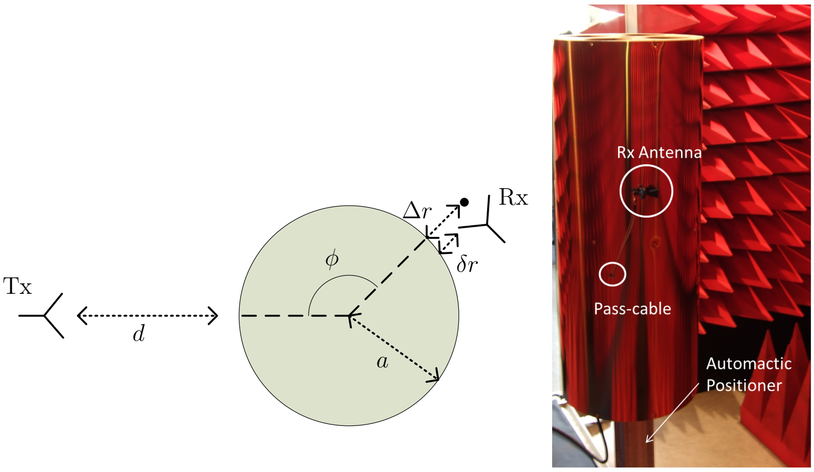

(a) Experimental Geometry. (b) Experimental Set-up.

Figure 3.9: The receiving horn antenna (Rx) is located against the cylinder and $\Delta r = \rho - a$ is defined from the cylinder surface to middle of the horn antenna. δr defines the distance between the cylinder surface and the antenna's edge. The distance d is defined from the cylinder surface to the transmitting horn antenna (Tx).

Figure 3.10: Photo of the U-band Antenna with 10° beamwidth

Table 3.3: VNA frequency parameters values

Symbol	Value
f_{start}	50 GHz
f_{stop}	60 GHz
f_{step}	66.67 MHz
VNA IFbandwidth	1 Hz
VNA Averaging parameter	1024

of 4.5 m which is sufficient to discriminate the relevant paths. The IFbandwidth and the averaging parameter are chosen to get the highest dynamic range possible. The bandwidth has been chosen between 50 GHz and 60 GHz. The upper frequency was limited because of the U-band (40 to 60 GHz) equipment available. The 10 GHz bandwidth was used to perform time-gating to increase the dynamic range. First, the raw S21-frequency data's are converted into delay domain using an IFFT operation. Then, the delay-domain data's (impulse response) are filtered using a rectangular window of 0.33 ns centred at the expect propagation delay (calculated as the distance between the antennas around the cylinder divided by the speed of light). Finally, the maximum value of the impulse response is kept. This technique allows to keep only the propagation path under interest by removing the effect of potential multipath components. Time-gating will give the measured path gain in the center of the bandwidth: 55 GHz. For a 0.2 m radius PEC cylinder, the difference between the path gains at 55 GHz and 60 GHz is about 0.126 dB/cm for TM mode and 0.055 dB/cm for TE mode (These values are calculated by using the theoretical equations of the path gain factors). The antenna was fixed on the cylinder. The whole cylinder was rotated thanks to an automatic angular positioner (*Newport MICRO-CONTROLE Motorized Rotation Stage RV Series*). The coaxial cables have about 6 dB/m losses. To avoid the need for long distance cables and optimize the received power, the VNA was put inside the anechoic chamber and covered by absorbing material. To

minimize the cables movement during rotation, all cables were passed inside the cylinder by a pass-cable expressly designed for.

This measurement campaign was conducted in order to validate the azimuth dependence of (3.18) and (3.26). Due to the use of horn antennas, the received field is integrated over the aperture size and so over ρ. Equations (3.18) and (3.26) are separated variables solutions in terms of radial and angular variations. The integration over the aperture size does not change the angular variation. For the first values of ϕ around 90 °, part of the horn antenna will be in the lit zone and the other in shadow one. The validity of the first measurements will be discussed in the following. To determine the shadow boundary influence, the receiving horn antenna is placed at two distances from the cylinder $\delta r=$ 0 mm (against the cylinder) and 20 mm. The second distance allows to have the entire aperture of the horn antenna in the lit region for the first measurement points. The distances Δr are summarized in Table 3.4 by taking into account the antenna size for TM and TE modes.

Table 3.4: Distances between the cylinder and the receiving horn antenna

Mode	δr [mm]	Δr [mm]
TM	0	15
	20	35
TE	0	11.5
	20	31.5

Antenna against the cylinder The measurements made with the VNA are compared with (3.18) and (3.26) with the antenna against the cylinder ($\delta r = 0$). Fig. 3.11 is drawn by normalizing the theoretical path gains with respect to the measured received power at $\phi = 90^\circ$.

As can be observed in Fig. 3.11, the model fits the measurements although after $\phi = 150^\circ$ the noise floor is reached and the measurements are no longer valid for TM case. For TE propagation mode, only the ρ polarization of the electric field was measured

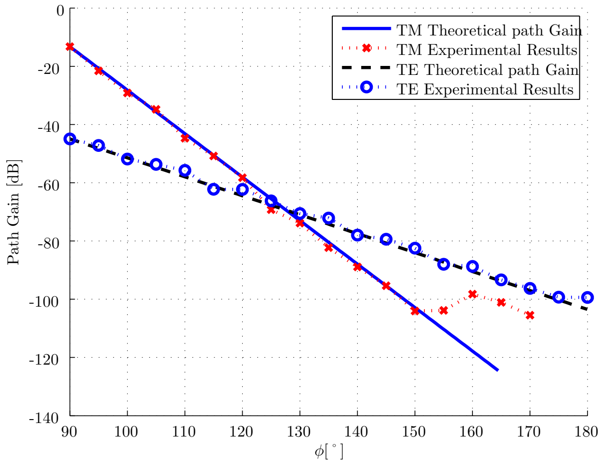

Figure 3.11: PEC case, antenna against the cylinder. Comparison between the theoretical path gain and the measurements for TE and TM modes with $f = 55$ GHz.

because of the horn antenna position. Equation (3.26) is still valid noting that $E_{\phi}^{\mathrm{TE}} \ll E_{\rho}^{\mathrm{TE}}$ in the shadow zone. It can be seen that the dynamic range is higher due to the lower path gain. In these two results, measurements also fit for values around $\phi = 90\,^\circ$. The influence of the shadow boundary cannot be interpreted in those figures.

Antenna at 2 cm away from the cylinder Path gain formulas are compared for the horn antenna at 2 cm from the cylinder which is equivalent to $\Delta r = 35$ mm (TM) and $\Delta r = 31$ mm (TE). In Fig. 3.12, it can be seen that measurements deviate from the path gain model below $\phi = 110\,^\circ$. The shadow boundary has been outlined for a better understanding. In this figure, unlike Fig. 3.11, the shadow boundary influence is clearly visible due to the fact that the entire receiving antenna was in the lit zone at the beginning of the measurements. These measurement positions should have been modeled with GO.

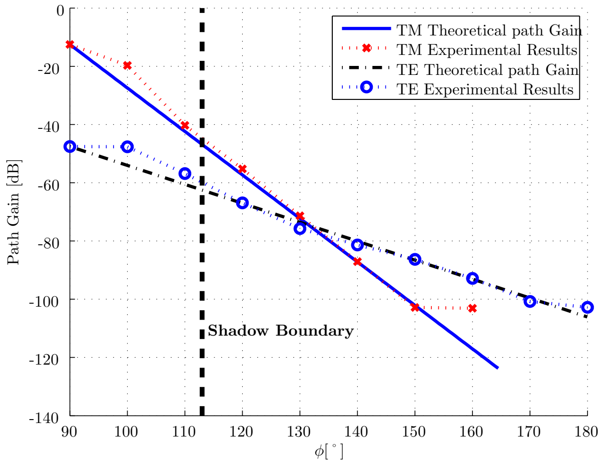

Figure 3.12: PEC case, antenna at 20 mm of the cylinder. Comparison between the theoretical path gain and the measurements for TE and TM modes with $f = 55$ GHz.

3.2.3.2 Elevation Angle Measurement Campaign

This experimental campaign has been conducted with the same experimental set-up as the previous one. Three values of θ_i have been chosen: 25 °, 55 °and 90 °. The measurements have been performed for both polarizations for three values of elevation angle. Time gating has been performed to increase the dynamic range. It was centered on the predicted time of arrival of the creeping wave. The results in Fig. 3.13 show that the analytical creeping wave models (3.18) and (3.26) fit the measurements. As can be seen, the TE mode has a higher dynamic range and, consequently, measurements are obtained up to higher values of ϕ.

3.2.3.3 Real Human Measurement Campaign

The second set of experiments was conducted on a real human body. The human body is compared with a dielectric ($\varepsilon'_r = 7.9753$ and $\sigma = 36.397$ S/m [3]) cylinder having with the same perimeter.

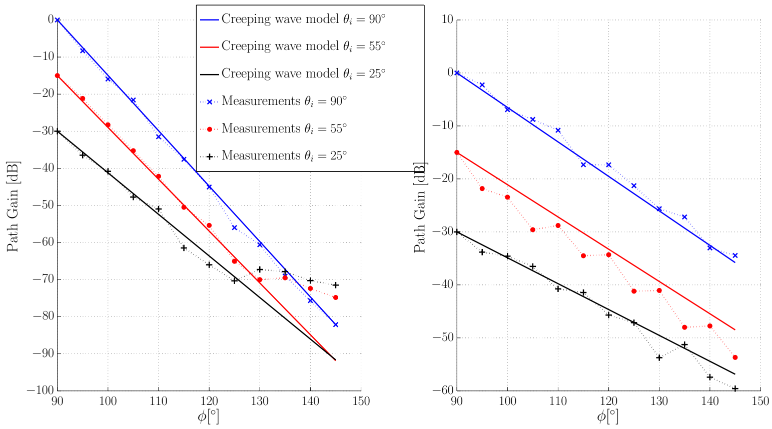

Figure 3.13: Measurement Results for different values of θ_i. On the left, TM polarization and TE polarization on the right side.

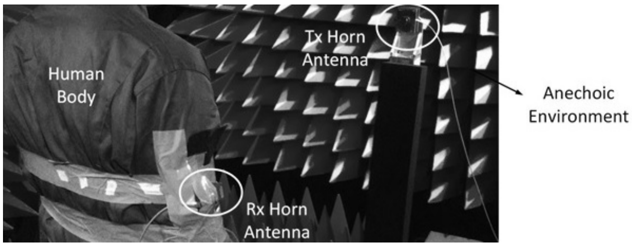

Figure 3.14: Photo of the experimental off-body experimental set-up in an anechoic chamber.

Experimental set-up The experimental set-up used for this campaign is the same as the one presented in Fig. 3.9(b) and a photo of the set-up is presented in Fig. 3.14. The same horn antennas have again been used in order to improve the dynamic range and to decrease the effect of parasitic phenomenon (multipath components). Hence, almost only the power due to the creeping wave around the human body is measured. The measurements were done at a single frequency $f_0 = 60$ GHz, to have quicker measurements. Each measurement was carried out during 60 seconds to average the influence of the small movements of the body. This measurement time is equivalent to 48 snapshots per spatial

Table 3.5: Main time-frequency parameters

Symbol	Value
f_0	60 GHz
VNA IFbandwidth	1 Hz
VNA Averaging parameter	1024
Measurement duration	60 s
Time averaging snapshots	48

Table 3.6: Main spatial parameters

Symbol	Value
Body Perimeter	93 cm
Equivalent Radius	14.8 cm
Spatial step	1.5 cm
Angular step	5.8 °
d	1.92 m

position. The main parameters of this campaign are presented in Table 3.5. The experiments were done around a human torso of 93 cm of perimeter. It is equivalent to a cylindrical body with a radius of about 14.8 cm. A spatial step of 1.5 cm was chosen which is equivalent to an angular step of 5.8 ° . These parameters are summarized in Table 3.6. The arms of the body remained up not to disturb the measurement around the torso.

Experimental Path Gains The theoretical gain factors for a cylinder with different values of radius a [cm] are summarized in Table 3.7. Measurement results for the TM polarization are shown in Fig. 3.15(a). The mean value of the received power fits the theoretical path gain (normalized according to the first experimental value). Measurements have been conducted up to 140 ° . Beyond that angle, the main path reaches the measurement noise level. Time gating could not be performed because of the single-frequency measurement constraint. The TE case is shown in Fig. 3.15(b). Measurements have been done in a larger range

Table 3.7: Theoretical path gain factors

a [cm]	$n_{\text{skin}}^{\text{TM}}$ [dB/cm]	$n_{\text{skin}}^{\text{TE}}$ [dB/cm]
13.8	5.489	3.552
14.8	5.242	3.426
15.8	5.021	3.304

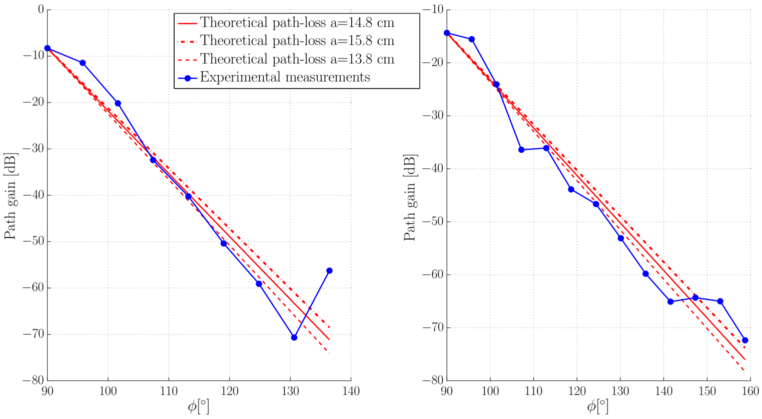

Figure 3.15: Human case. Antenna against the body. Comparison between the theoretical path gain for TM polarization on the left and TE polarization on the right for different radius a with $\Delta r = 11.5$ mm with $f = 60$ GHz.

than the TM case because of the higher dynamic range. Experiment and theoretical results show a good agreement as well.

These results show the validity of using a simple path gain formula obtained with an equivalent cylinder for a real body. As can be observed, different theoretical curves have been plotted to study the sensitivity of the radius a of the equivalent cylinder, by choosing a maximum error of 1 cm. It can be observed in Table 3.7 that an error of 5% on a gives an error of 3.5% on $n_{\text{skin}}^{\text{TM}}$ and 2.75% on $n_{\text{skin}}^{\text{TE}}$. Fig. 3.15 (a) and (b) show that these differences are negligible. Evaluation of the mean square root error (MSRE) has been done in [dB]. The errors are summarized in Table 3.8. This table shows that the MSRE hardly changes with the equivalent radius a. The low sensitivity of the theoretical path gain curve allows an error of 1 cm on the radius a.

Table 3.8: Mean Square Root Error with the equivalent radius

a [cm]	MSRE_{TM}	MSRE_{TE}
13.8	0.080	0.077
14.8	0.077	0.073
15.8	0.112	0.079
Minimum MSRE		
14.4	0.073	-
14.9	-	0.074

3.3 Indoor Off-Body Channel model

In an off-body scenario, each ray in (3.1)-(3.2) is perturbed by the presence of the human body near the receiver. In order to extend the model to an off-body scenario, the idea is to convert each ray in (3.1)-(3.2) into a wave diffracted by a circular cylinder with a radius a and an antenna located at (ρ, ϕ_0) position.

The proposed model allows one to study a variety of parameters for an off-body communication. First, it permits to study the effect of the environment on the received power, the orientation of the user with respect to the transmit antenna and the polarization of the transmitted waves. Since the model is ray based, the effect of the antennas can be easily taken into account by introducing radiation patterns. Indeed, by measuring or simulating with commercial software the radiation pattern of the receive antenna located close to the body, it allows one to conduct more accurate simulations. In the following, the antennas will be assumed to be isotropic and omni-directional.

The aim of this model is to give quick and averaged quantities for a specific scenario. It is not claimed to be a high accuracy model. Indeed, the circular cylinder model has been widely used in the field of BANs but it is a simplified shape. It does not permit to change the posture of the body or to move some parts of it. Also, it is shown above that the creeping wave formula on the cylinder shows a maximum 3 dB error on the received power on a real human torso. Another limitation of the model is the simple reflection created in the lit region. The fact of having a more complex body shape (roughness, irregularities, body parts,...) would probably generate a reflected cluster instead of a wave. This can be evaluated through extensive measurement but it is not the scope of this chapter.

The validity of this model is related to the chosen indoor channel model. In fact, the diffraction model is valid over a large frequency range while the indoor channel model is based on measurements conducted on the frequency range from 55 to 65 GHz which limits the frequency range of the model proposed in the section.

3.3.1 Model Generation

Let $\mathcal{T}$ be the operator applying this transformation:

$$\begin{pmatrix} \alpha^{(i,k)'} \\ \tau^{(i,k)'} \\ \phi_{\mathrm{rx}}^{(i,k)'} \\ \theta_{\mathrm{rx}}^{(i,k)'} \end{pmatrix} = \mathcal{T}_{(a,\rho,\phi_0)} \begin{pmatrix} \alpha^{(i,k)} \\ \tau^{(i,k)} \\ \phi_{\mathrm{rx}}^{(i,k)} \\ \theta_{\mathrm{rx}}^{(i,k)} \end{pmatrix} \tag{3.28}$$

where the parameters in the off-body scenario take a ' and the other parameters on the right-hand side are given by the IEEE 802.11ad model. As explained previously, $\mathcal{T}$ must be defined by considering two regions: $\mathcal{T}^{\mathrm{lit}}$ in the lit and $\mathcal{T}^{\mathrm{sha}}$ in the shadow region described in Fig. 3.2(a). The delay and angular parameters are easily obtained geometrically.

Lit Region The operator $\mathcal{T}^{\text{lit}}$ modifies the incident plane wave and adds a reflected one.

$$\mathcal{T}^{\text{lit}}_{(a,\rho,\phi_0)} \begin{pmatrix} \alpha^{(i,k)} \\ \tau^{(i,k)} \\ \phi^{(i,k)}_{\text{rx}} \\ \theta^{(i,k)}_{\text{rx}} \end{pmatrix} = \begin{pmatrix} \alpha^{(i,k)} \\ \tau^{(i,k)} - \dfrac{a\cos(\Delta\phi)}{c} \\ \Delta\phi \\ \theta^{(i,k)}_{\text{rx}} \end{pmatrix} \oplus \begin{pmatrix} R_\upsilon \alpha^{(i,k)} \sqrt{\dfrac{\rho_r}{\rho_r + s_r}} e^{-jks_r} \\ \tau^{(i,k)} - \dfrac{a\cos\psi - s_r}{c} \\ \pi + \psi \\ \pi - \theta^{(i,k)}_{\text{rx}} \end{pmatrix} \tag{3.29}$$

where $\Delta\phi = |\phi_0 - \phi^{(i,k)}_{\text{rx}}|$, c is the speed of light and $\oplus$ refers to adding a new wave in the impulse response. $\rho_r = \frac{a}{2}\cos\psi$, ψ is the reflection angle, s_r is the distance between the antenna and reflection position and R_υ is the reflection coefficient depending on the polarization $\upsilon = \rho, \phi$ or z where

$$R_\phi = R_\rho = \frac{\cos\psi_t - \sqrt{\varepsilon_r}\cos\psi}{\cos\psi_t + \sqrt{\varepsilon_r}\cos\psi} \text{ and } R_z = \frac{\cos\psi - \sqrt{\varepsilon_r}\cos\psi_t}{\cos\psi + \sqrt{\varepsilon_r}\cos\psi_t}. \tag{3.30}$$

where $\psi_t = \arcsin(\sin(\psi)/\sqrt{\varepsilon_r})$.

Shadow Region The operator $\mathcal{T}^{\text{sha}}$ is given by:

$$\mathcal{T}^{\text{sha}}_{(a,\rho,\phi_0)} \begin{pmatrix} \alpha^{(i,k)} \\ \tau^{(i,k)} \\ \phi^{(i,k)}_{\text{rx}} \\ \theta^{(i,k)}_{\text{rx}} \end{pmatrix} = \begin{pmatrix} C^\gamma_\upsilon(\theta_i)\alpha^{(i,k)} e^{-j\eta^\gamma \Delta\phi} \\ \tau^{(i,k)} + r\dfrac{\Delta\phi - \pi/2}{c} \\ \pi/2 \\ \theta^{(i,k)}_{\text{rx}} \end{pmatrix} \tag{3.31}$$

where γ is the polarization of the emission source such as $\gamma =$ TM or TE, $C^\gamma_\upsilon(\theta_i)$ and η^γ are derived from section 3.2.1 and recalled here below. For a TM polarization transmitter, the coefficient C^{TM}_υ is given by:

$$\begin{aligned} C^{\text{TM}}_\rho &= -\frac{2\pi}{m} j \cos\theta_i e^{jkz\cos\theta_i} j^{\upsilon_1+1} \tilde{a}_{\upsilon_1} W_2{}'(\tau_1 - h) \\ C^{\text{TM}}_\phi &= -2\pi j \frac{\cot\theta_i}{k\rho} e^{jkz\cos\theta_i} \upsilon_1 j^{\upsilon_1} \tilde{a}_{\upsilon_1} W_2(\tau_1 - h) \\ C^{\text{TM}}_z &= 2\pi \sin\theta_i e^{jkz\cos\theta_i} j^{\upsilon_1+1} \tilde{a}_{\upsilon_1} W_2(\tau_1 - h) \end{aligned} \tag{3.32}$$

where τ_1 is defined as the first solution of:

$$W_2'(\tau_1) - qW_2(\tau_1) = 0 \tag{3.33}$$

and $A(z)$ is the first kind Airy function, $W_2(z) = 2e^{j\pi/6}A(e^{j4\pi/3}z)$, $q = jm\sqrt{\varepsilon_r/\mu_r}$, $m = (ka\sin\theta_i)^{1/3}$, $h = \frac{k}{m}\sin\theta_i(\rho - a)$ and:

$$\begin{aligned}\Phi_\upsilon(\phi) &= \frac{\cos(\upsilon(\phi-\pi))}{\sin(\upsilon\pi)}\\ \tilde{a}_{\upsilon_1} &= \frac{A'(\tau_1) - qA(\tau_1)}{\tau_s W_2(\tau_1) - qW_2'(\tau_1)}\end{aligned} \tag{3.34}$$

Also, it can be inferred that:

$$\eta^{\mathrm{TM}} = ka\sin\theta_i + m\tau_1 \tag{3.35}$$

For a TE polarization transmitter, the coefficient C_υ^{TE} is given by:

$$\begin{aligned}C_\rho^{\mathrm{TE}} &= \frac{-j}{k\rho}\frac{e^{-jkz\cos\theta_i}}{\sin\theta_i}2\pi\upsilon_1' j^{\upsilon_1'}\tilde{b}_{\upsilon_1'}W_2(\tau_1' - h)\\ C_\phi^{\mathrm{TE}} &= je^{-jkz\cos\theta_i}\frac{2\pi}{m}j^{\upsilon_1'+1}\tilde{b}_{\upsilon_1'}W_2'(\tau_1' - h)\\ C_z^{\mathrm{TE}} &= 0\end{aligned} \tag{3.36}$$

where τ_1' is the first zero of:

$$qW_2'(\tau_1') - W_2(\tau_1') = 0 \tag{3.37}$$

and

$$\tilde{b}_{\upsilon_1'} = \frac{qA'(\tau_1') - A(\tau_1')}{q\tau_1' W_2(\tau_1') - W_2'(\tau_1')}. \tag{3.38}$$

Also, it can be inferred that:

$$\eta^{\mathrm{TE}} = ka\sin\theta_i + m\tau_1' \tag{3.39}$$

3.3.2 Channel Simulations

The indoor environment we consider is the *Conference Room* environment of the IEEE 802.11ad model [56]. The room has a size of 4.5 ×

3×3 m^3. The channel is studied for a receive (Rx) and transmit (Tx) antenna at 1.5 m height. The distance d between the antennas is 2 m. Tx is placed at location (1m, 1.5m, 1.5m). The Rx antenna is assumed to be located at 5 mm from the body surface. For sake of simplicity, it is assumed that the antennas are dimensionless isotropic radiators and so omni-directional with a gain equal to 0 dBi. The radius of the cylinder body has been set to 0.15 m. The body turns around with $\phi = 0\,^\circ$ to 180 ° with an angular step of 5 ° . The reference $\phi = 0$ is the axis between Tx and the center of the body. 2430 channel realizations are calculated by changing the position of the user in the room, paying attention to still have $d = 2$ m. In the following, averaged results on the channel realizations are presented.

In an off-body scenario, the parameter of interest is the orientation ϕ of the body with respect to the transmitter and all results will be plotted as a function of this angle. Obviously, the case without body does not depend on ϕ and corresponding results will always be constant. It will be referred as “TM indoor” or “TE indoor” according to the transmitted wave propagation.

Channel Attenuation The channel gain is considered as the mean value of the frequency response $E[|H(f)|^2]$ where $E[\cdot]$ stands for the expected value on the channel realizations. It is presented in Fig. 3.16. The mean attenuation is of first importance because it is directly related to the averaged SNR over the bandwidth.

It can be seen in Fig. 3.16 that for most values of ϕ, the body creates a high attenuation compared to the indoor case. This attenuation is due to two phenomena. First, the scattering by the human body creates constructive and destructive interferences in the lit region. The interference between the direct path and the the waves scattered (reflected) by the body is the reason for the appearance of the local maxima and minima of the channel gain in the lit region. In the shadow region, the body shadows the signal which creates the high power decrease when the user turns around. Secondly, with TE polarization, a polarization mis-alignment occurs when the body turns around. When

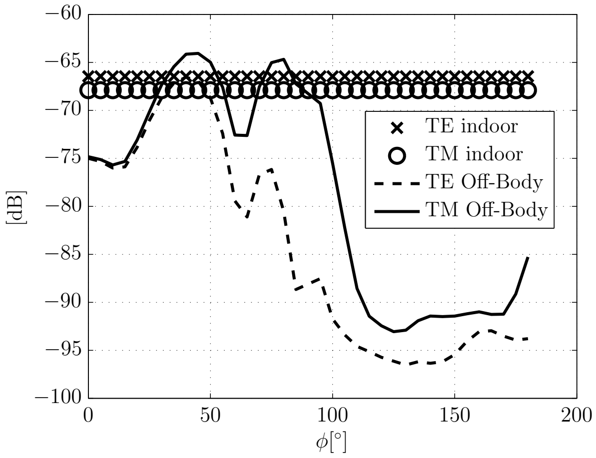

Figure 3.16: Channel gain for a distance of 2 m. Comparison between indoor and indoor off-body.

the body turns, the orientation of the receiving antenna changes. If this receiving antenna orientation is not completely aligned to the incident multipath component, an attenuation occurs due to this mis-alignment.

Rician Factor The Rician K factor is calculated by:

$$K = \frac{\max_{(i,k)} \left[\alpha^2_{(i,k)}\right]}{\sum_{(i,k)} \alpha^2_{(i,k)} - \max_{(i,k)} \left[\alpha^2_{(i,k)}\right]} \tag{3.40}$$

This allows us to characterize the effect of the multipath components due to the environment with regard to the main path. A high value for K implies that the channel is line-of-sight like while low K channels have an higher sensitivity to multipath components. It is important to notice that this definition is not the commonly used Rician factor defined as the power of the line-of-sight component divided by the total power of the multipath components. The definition (3.40) seemed more relevant for the studied scenario.

Fig. 3.17 shows the K factor for both indoor and indoor off-body. This figure allows one to compare the power of the LOS with respect to the multipath components. Again it is shown that for some values of ϕ the channel has a higher K factor than in the case of the indoor channel without human body. In the lit region, most of the multipaths is blocked by the human body. Also the Rician factor highly depends on the polarization alignment between the receiving antenna and the incident plane waves. Multipath components in TE polarization will be quickly attenuated due to polarization mis-alignment.

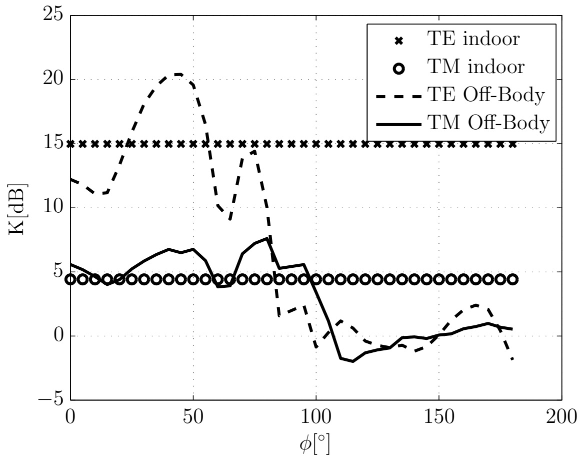

Figure 3.17: Rician K-factor for a distance of 2 m. Comparison between indoor and indoor off-body.

3.3.3 Experimental Assessment

Experiments have been performed in order to validate the numerical model proposed in section 3.3. The measurement have been conducted in a 7×4 m^2-room. The transmitter (Tx) has been located in the center of the room and the receive antenna (Rx) was located on the body torso. *Flann Microwave* omni-directional antennas have been used and located at 1.3 m height from the ground. The antenna were placed vertically to the ground in order to measure TM polarization. Fig. 3.18 shows the elevation radiation pattern of the antenna under test (the azimuthal radiation pattern has no interest since it is omni-directional). The antenna has the main effect of reducing the mutlipath components coming from the ground and the ceiling. However, it allows to measure the reflected wave on the body which is one of main phenomenon under study. It is then important that the reader keeps in mind that the antenna will not measure some simulated paths. However, these paths with extreme elevation angle values have not a strong influence on the considered channel. Also, the antenna size is electrically large which may introduce some spatial averaging of the channel. However, this phenomenon is neglected in the following since only large scale parameters (mean attenuation and K-factor) are under interest. S21 parameter has been measured using a *R&S* Vector Network Analyzer (VNA) up to 75 GHz. The carrier frequency was set to 60 GHz with a span of 1 GHz. The frequency step was 10 MHz and the IF bandwidth was set to 0.1 kHz. The output power of the VNA was 0 dBm. In order to improve the dynamic range, a 35 dB low noise amplifier has been used at the receiver side. The measure has been repeated 20 times. The user was a 1.85 m tall male. His body perimeter is 84 cm. Measurement have been taken each 2 cm on the body.

The measurement results are presented in Fig. 3.19. The mean attenuation is presented on the left of the figure. The simulations are presented as the mean value over the channel realizations with its standard

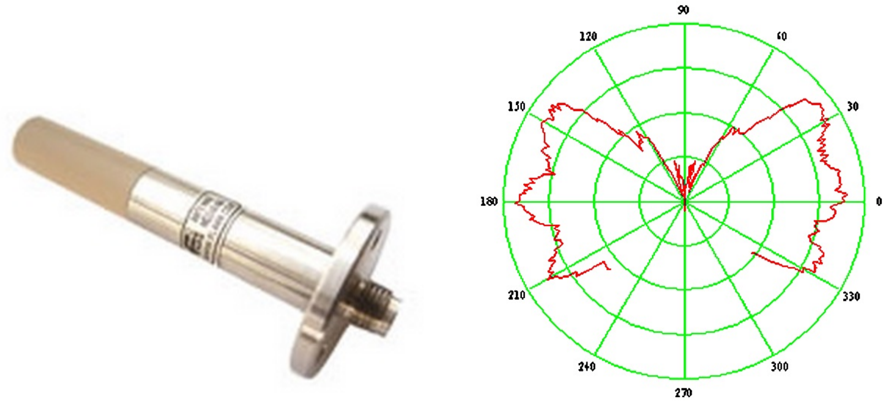

Figure 3.18: *Flann Microwave* omni-directionnal antenna and elevation radiation pattern (4dB/div).

deviation. The radius of the cylinder model has been chosen in order to have the same perimeter of the subject, namely 13.5 cm. The measured mean channel attenuation shows good agreement with the model except for the region corresponding to the front of the user. The drop of power appearing in the simulations in the front of the user is due to the destructive interference between the direct and reflected paths on the body. However, in the experiment, we measured only the direct path for the first measured positions due to the obstruction of the antenna. The interference between direct and reflected paths can be further observed in the positions where the antenna is not blocking the reflection off the body. The average power in the shadow region corresponding to the multipath components is correctly simulated.

The right side of Fig. 3.19 shows the K-factor of the measurement compared to the simulations. For the front zone, it can be observed that the Rice factor is greater than the model prevision, thus reinforcing the hypothesis that the reflected path is masked or weaker. It can be seen that the experimental results and the simulations show good match.

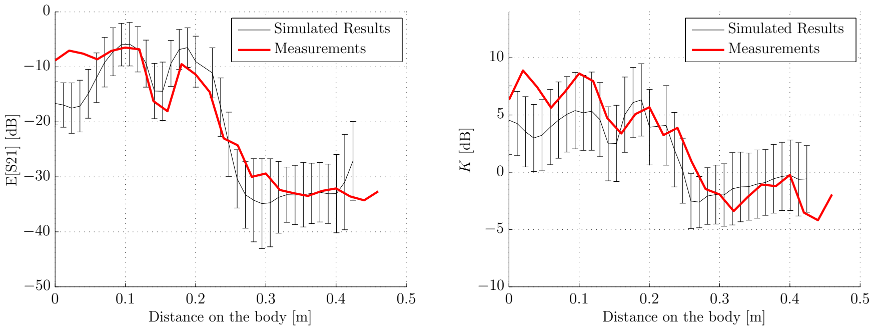

Figure 3.19: Comparison between measurements and simulated results for TM polarization. The mean attenuation is presented on the left and the Rician K-factor on the right.

3.4 Performance Evaluation of WiGig in an indoor Off-Body Communication

3.4.1 Simulation Results

The bit error rate (BER) of an OFDM communication is studied without channel coding. It is important to notice that using a channel coding will allow to reach better performances than the ones obtained in the following. The effect of the multipath components on the BER can change accordingly. The aim of this section is to present a comparison between the polarized channels. No further discussion is made regarding the coding and it is left to the interested reader. The communication system is assumed to be a WiGig [15] whose parameters are summarized as following. The sampling rate and the occupied bandwidth are respectively 2.64 GHz and 1.825 GHz. The number of subcarriers, the occupied subcarriers and the cyclic prefix are 512, 358 and 128 (giving a 5.15625 MHz subcarrier spacing). For this scenario, a QPSK modulation has been chosen.

The noise floor n is defined as the thermal noise over the bandwidth Δf plus the receiver noise figure NF:

$$n = k_B T \Delta f + \mathrm{NF} \simeq -80 + \mathrm{NF}\ [\mathrm{dBm}] \tag{3.41}$$

where k_B is the Boltzmann constant, T is the temperature (assumed 290 K). The receiver noise figure is assumed to be 10 dB and the noise floor is then equal to -70 dBm. The emitted power P_{Tx} is 10 dBm.

Two different omni-directional antenna polarizations are studied. Body worn antennas are generally z or ϕ polarized. The standard channel model calculates the impulse channel for both emitting TM and TE polarizations. The TM mode is matched to z receiving polarization, while mode TE is matched to ϕ polarization. The other combinations of polarizations are considered as cross-polarization and negligible.

In Fig. 3.20, it can be seen that a trade-off between TM and TE polarizations appears. It can be observed that TE polarization gives a better BER in the lit zone, even below 10^{-7} for some positions. But the angular coverage around the body is smaller than with a

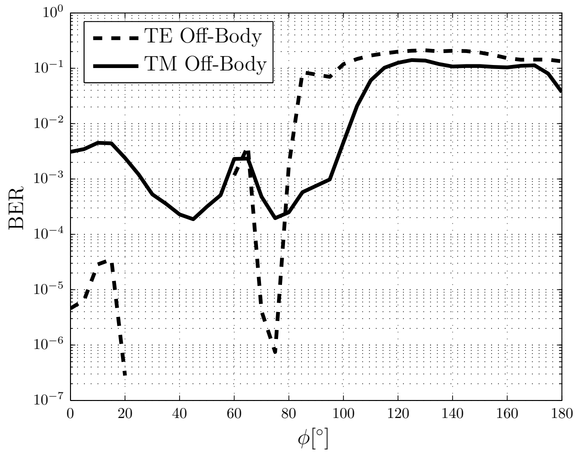

Figure 3.20: BER for QPSK modulation. The BER in indoor environment is lower than 10^{-7} and not shown here.

TM polarization, for a reference BER. It can be observed that the BER increases after $\phi = 100\,^{\circ}$ for TM polarization while it falls from $80\,^{\circ}$ onward for TE polarization. This phenomenon is mainly due to a polarization mis-alignment at the receiver side when the body turns around. In TM polarization, the receiving antenna is always aligned.

In the lit region, as observed in Fig. 3.16, TM polarization has a better SNR than TE polarization but the BER of TE polarization is much better. This comes from the better K factor of TE polarization. Around the transition region (between lit and shadow), the Rice factor and SNR of TE polarization drop while they remain high enough for TM polarization. This explains why the coverage of TM polarization is higher than the TE one.

3.4.2 Spatial and Polarization Diversity

As can been seen in Fig. 3.20, the BER in the off-body case is largely poorer than in the indoor case without body. A Maximum Ratio Combining (MRC) scheme [74] can be used to increase the performance based on polarization or spatial diversity. Polarization diversity takes into account the received channel for both TE and TM polarizations at the same location while spatial diversity is calculated with received antennas spaced by 1.7 cm (equivalent of 5 ° on the body). Spatial diversity is calculated for each polarization. In order to be comparable to the polarization diversity, a two-antennas spatial diversity scheme is studied.

It can be seen in Fig. 3.21, as expected, that MRC largely increases the communication performance. In the case of spatial diversity, the trade-off obtained in the previous section remains. TE polarization reaches better performance but coverage is higher for TM polarization.

Polarized MRC takes advantage of both polarizations. The coverage is increased and the performances in the lit region is still high. Also, polarization diversity allows to build more compact receivers than spatial diversity.

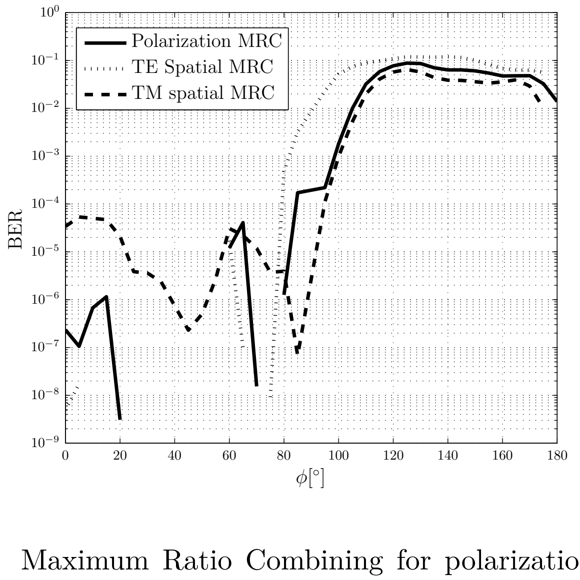

Figure 3.21: Maximum Ratio Combining for polarization and spatial diversity.

3.5 Summary

This chapter proposes a numerical implementation of a polarized 60 GHz indoor off-body channel model has been studied. This model is based on the standardized indoor channel IEEE 802.11ad and the diffraction by a circular cylinder.

A fast computation diffraction solution is proposed by using a combination of geometrical optics and creeping wave equations. This solution has been validated on a PEC cylinder and a real human body. For the cylinder case, the creeping wave path gains perfectly fits with the theoretical propagation model developed in this chapter while for the human body case, a 3 dB maximum error has been obtained. These experimental results prove that the propagation model is accurate enough and is thereby well suited for being included in a standard such as IEEE 802.11ad.

Parameters of the indoor off-body channel such as mean attenuation and Rice factor have been extracted with the body orientation through the azimuthal angle ϕ. These parameters are compared to the indoor ones. The human body influence on the channel has been studied. It has been shown that it creates variability depending on the orientation. Finally, a WiGig communication has also been computed on the developed channel. The bit error rate is studied for both TM and TE polarizations as a function of the body orientation. It has been observed that TE mode gives a better BER in the lit zone but the coverage around the body is less than TM mode for a reference BER. Further, a Maximum Ratio Combining scheme has been computed in order to compare polarization and spatial diversity.

Chapter 4

On-body channel characterization

Contents

4.1 On Torso Propagation

4.1.1 Flat Body Propagation model

Classic analytic models for on-torso propagation are solved by assuming that the body is flat. This has been widely investigated by Norton for radio communication during the 20th century [75].

Mathematically, the problem is modelled as a normal or tangential dipole radiating over a flat body as depicted in Fig. 4.1. The flat body is a lossy media with a complex permittivity ε. Due to the small wavelength and skin-depth at 60 GHz, the body model can be assumed having the electric properties of the human skin. $\hat{z}$ is the axis normal to the surface and a (ρ, ϕ, z) coordinate system is adopted. The dipole with current I and length l is placed at a height h. The time dependence $e^{j\omega t}$ is assumed and suppressed. The solution is developed for both normal and tangential polarizations. The model is developed by considering infinitesimal dipoles which are the basic elements to form more complex radiation patterns and antennas since the field radiated by any antenna is a superposition of infinitesimal dipoles at the surface of the antenna. In the following, only the solutions for dipoles are considered but the reader has to keep in mind that it can be extended to more complex antennas.

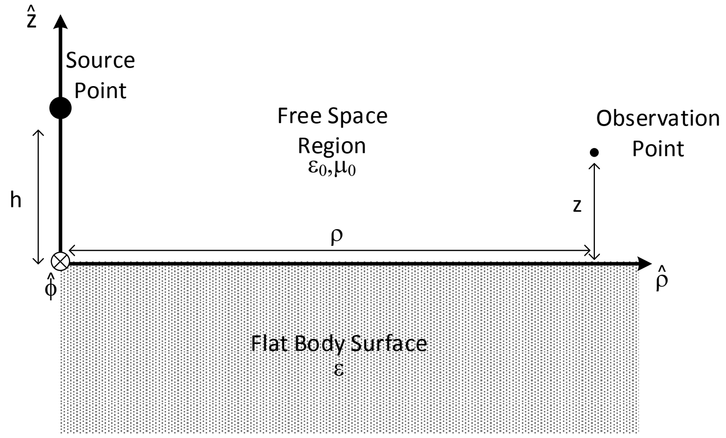

Figure 4.1: Flat Body geometry.

Normal Polarization The electric field components are E_z and E_ρ. It can be seen that the solution does not depend on ϕ due to symmetry [75].

$$\begin{aligned}
E_\rho(\rho, z) =& -\frac{2\omega\mu_0 Il}{4\pi k_0}\{e^{jk_0r_1}(\frac{\rho}{r_1})(\frac{z-h}{r_1})(\frac{jk_0}{r_1}-\frac{3}{r_1^2}-\frac{3j}{k_0r_1^3}) \\
&+ e^{jk_0r_2}(\frac{\rho}{r_2})(\frac{z+h}{r_2})(\frac{jk_0}{r_2}-\frac{3}{r_2^2}-\frac{3j}{k_0r_2^3}) \\
&- 2\epsilon e^{jk_0r_2}\left[(\frac{\rho}{r_2})(\frac{jk_0}{r_2}-\frac{1}{r_2^2}) - k_0^2\epsilon(\frac{\pi}{k_0r_2})^{1/2}e^{-jw}F(w)\right]\} \\
E_z(\rho, z) =& \frac{2\omega\mu_0 Il}{4\pi k_0} \\
&\times \{e^{jk_0r_1}\left[\frac{jk_0}{r_1}-\frac{1}{r_1^2}-\frac{j}{k_0r_1^3}-(\frac{z-h}{r_1})^2(\frac{jk_0}{r_1}-\frac{3}{r_1^2}-\frac{3j}{k_0r_1^3})\right] \\
&+ e^{jk_0r_2}\left[\frac{jk_0}{r_2}-\frac{1}{r_2^2}-\frac{j}{k_0r_2^3}-(\frac{z+h}{r_2})^2(\frac{jk_0}{r_2}-\frac{3}{r_2^2}-\frac{3j}{k_0r_2^3})\right] \\
&- 2k_0^2\epsilon e^{jk_0r_2}(\frac{\pi}{k_0r_2})^{1/2}(\frac{\rho}{r_2})e^{-jw}F(w)\}
\end{aligned} \tag{4.1}$$

In these formulas, $r_1 = \sqrt{\rho^2+(z-h)^2}$, $r_2 = \sqrt{\rho^2+(z+h)^2}$ and

$$F(w) = \frac{1}{2}(1+j) - \int_0^w \frac{e^{jt}}{(2\pi t)^{1/2}}dt, \; w = \frac{k_0r_2}{2}(\frac{\epsilon r_2+z+h}{\rho})^2 \tag{4.2}$$

where $\epsilon = \frac{k_0}{k_2} - jk_0l$.

Tangential Polarization The solutions for a dipole parallel to the surface are involving z-, ρ- and ϕ-components of the electric field since the azimuthal symmetry is not respected anymore. Norton's equations for the tangential dipole are given by:

$$E_z = \frac{-2\omega\mu_0 Il}{4\pi k_0}\cos\phi\left[(\frac{\rho}{r_2})(\frac{jk_0}{r_2}-\frac{1}{r_2^2}) - k_0^2\epsilon(\frac{\pi}{k_0r_2})^{1/2}e^{-jw}F(w)\right] \tag{4.3}$$

$$\begin{aligned}
E_\rho =& \frac{2\omega\mu_0 Il}{4\pi k_0}\cos\phi \times \\
&\{e^{jk_0 r_1}\left[\frac{2}{r_1^2}+\frac{2j}{k_0 r_1^3}+(\frac{z-h}{r_1})^2(\frac{jk_0}{r_1}-\frac{3}{r_1^2}-\frac{3j}{k_0 r_1^3})\right] \\
&-e^{jk_0 r_2}\left[\frac{2}{r_2^2}+\frac{2j}{k_0 r_2^3}+(\frac{z+h}{r_2})^2(\frac{jk_0}{r_2}-\frac{3}{r_2^2}-\frac{3j}{k_0 r_2^3})\right] \\
&+2e^{jk_0 r_2}\Bigg[\epsilon(\frac{z+h}{r_2})(\frac{jk_0}{r_2}-\frac{1}{r_2^2})-\epsilon^2\Bigg(\frac{jk_0}{r_2}-\frac{1}{r_2^2}-\frac{j}{k_0 r_2^3} \\
&-k_0^2\epsilon(\frac{r_2}{\rho})(\frac{\pi}{k_0 r_2})^{1/2}e^{-jw}F(w)\Bigg)\Bigg]\}
\end{aligned} \tag{4.4}$$

$$\begin{aligned}
E_\phi =& \frac{-2\omega\mu_0 Il}{4\pi k_0}\sin\phi \times \\
&\{e^{jk_0 r_1}(\frac{jk_0}{r_1}-\frac{1}{r_1^2}-\frac{j}{k_0 r_1^3})-e^{jk_0 r_2}(\frac{jk_0}{r_2}-\frac{1}{r_2^2}-\frac{j}{k_0 r_2^3})) \\
&+2e^{jk_0 r_2}\Bigg(\epsilon(\frac{z+h}{r_2})(\frac{jk_0}{r_2}-\frac{1}{r_2^2}) \\
&-\epsilon^2\Bigg[\frac{2}{r_2^2}+\frac{2j}{k_0 r_2^3}+(\frac{z+h}{r_2})^2(\frac{jk_0}{r_2}-\frac{3}{r_2^2}-\frac{3j}{k_0 r_2^3}) \\
&+jk_0\epsilon(\frac{r_2^2}{\rho^3})(\frac{\pi}{k_0 r_2})^{1/2}e^{-jw}F(w)\Bigg]\Bigg)\}
\end{aligned} \tag{4.5}$$

The normal and tangential dipole solutions are not straightforward and are complicated to be simplified into approximate solutions. In the literature, a numerical fit with a logarithmic path loss in dB is often used [61]:

$$P = |E_i|^2_{\mathrm{dB}} = |E_i|^2_{0,\mathrm{dB}} - 10n\log_{10}(\rho/\rho_0) \tag{4.6}$$

where $i = z, \rho$ or ϕ, $|E_z|^2_{0,\mathrm{dB}}$ is the field strength in dB at the reference distance ρ_0 and n is the path loss exponent. In [61], a numerical study has been conducted at 60 GHz and it has been shown that the path loss expression gives good results compared to experiments. The value of the path loss exponent n for both polarizations at high distances (a few wavelengths) is equal to 4.

4.1.2 Simulation Results

Norton's formulation are used in order to calculate the electric field above a surface and predict the propagation on a human torso. Norton's equations are considering the electric field as a sum of a Geometrical Optics (GO) solution and a surface wave. The GO solution is made up the line-of-sight wave and the reflected one off the surface. Some works often neglect the surface wave which is a valid assumption when considering the antenna height high enough (some wavelengths). However, the surface wave is inseparable from this solution. Some works [76] are aiming to study the relative contribution from each component (GO or surface wave) which may be interesting in order to study how the electric field behaves. Nevertheless, this kind of study has no real interest in the sense that these components can not be excited independently and this will then not be pursuit here.

In Fig. 4.2, the normal polarization of Norton's equations is presented for different antenna heights z and d. It is shown that increasing the height between the antenna and the surface improves propagation. However, for heights higher than 2λ, path loss oscillations are appearing

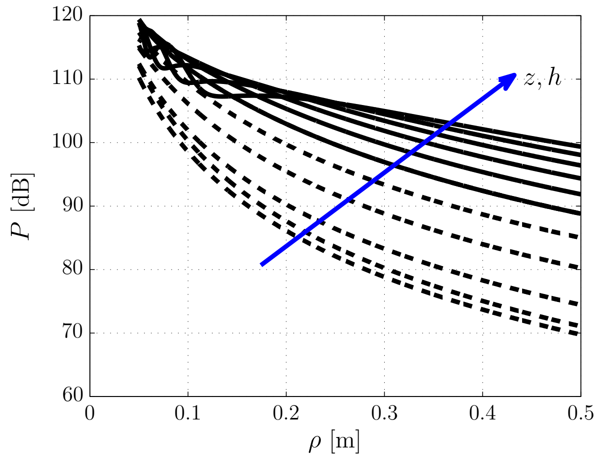

Figure 4.2: Normal polarization z-component of the electric field. The dotted lines are obtained for height between the surface and the antenna below $2\lambda = 1$ cm. The lines are obtained for height between 2λ and 4λ.

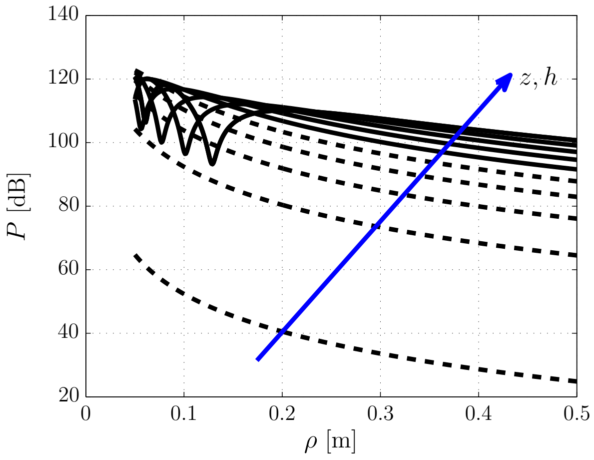

Figure 4.3: Tangential polarization ϕ-component of the electric field in the plane $\phi = \pi/2$. The dotted lines are obtained for heights smaller than $2\lambda = 1$ cm. The lines are obtained for heights between 2λ and 4λ.

at short distance.

In Fig. 4.3, the ϕ-component of the tangential polarization of Norton's equations is presented for different antenna heights z and d. The conclusion are the same as the one for normal polarization. However, in Fig. 4.4, an angular plot of the different components of the electric field is proposed at distance $\rho = 10$ cm. It is shown that, in the plane $\phi = \pi/2$, there is only the ϕ-component while for other values of ϕ, the z-component prevails.

4.1.3 Experimental validation

A measurement campaign has been conducted in order to assess Norton's formulations above the human skin at 60 GHz. A porcine skin of 3 mm thickness and 5 cm width has been used as a phantom for the human skin. Two V-band open rectangular waveguides were pointing towards each other and were placed at the same height from the phantom surface as can be seen in Fig 4.5. These antennas have been chosen in order to be as close as theoretical dipole antenna. The size of the aperture is small enough to neglect spatial averaging effects.

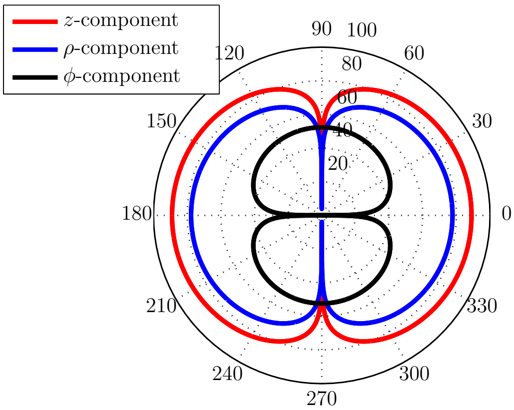

Figure 4.4: Tangential polarization. The three components are compared with $\rho = 10$ cm and $z = h = 0$.

Also, the radiation pattern is wide enough to be able to measure the reflected and surface waves. It seems that these antennas were well suited to assess Norton's equation with the distance between the antennas. Antennas were moved by a automatic positioning device. Data were collected with a Rhode & Schwartz Vector Network Analyzer. In order to remove multipath components, time gating was performed on the collected data by calculating the average power of the frequency data. The measurement were conducted on a 10 GHz bandwidth around 60 GHz with an IF bandwidth of 10 Hz. 101 frequency points were collected. Measurements have been collected for distances ranging from 5 cm to 40 cm with a 1 cm-spatial step.

The measurement were conducted only for normal polarization. Other results can be founded in [61]. The theoretical model has been assessed for two antenna heights, 3 mm and 20 mm. Results are presented in Fig. 4.6 and 4.7. These results shows excellent agreement between experiments and models. The electrical properties of the human skin at 60 GHz have been used in these figures. Oscillations can also been observed in Fig. 4.7 due to interference between direct and reflected wave.

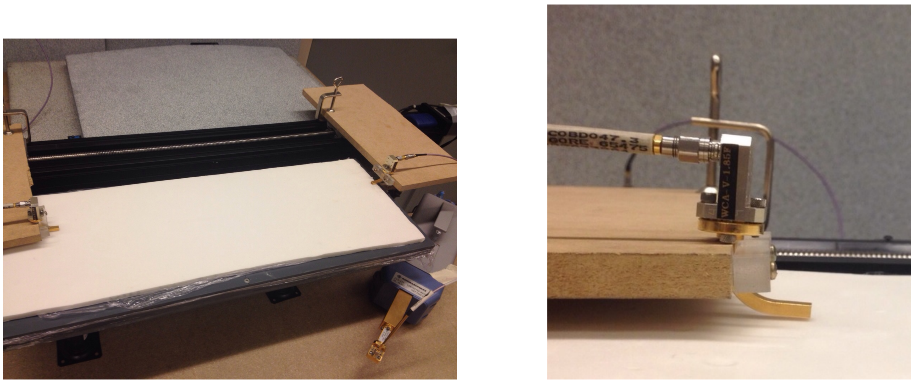

Figure 4.5: Photo of the experiment set-up. The antennas were placed above a white flat phantom. The photo of the open waveguide without flanges is presented on the right side.

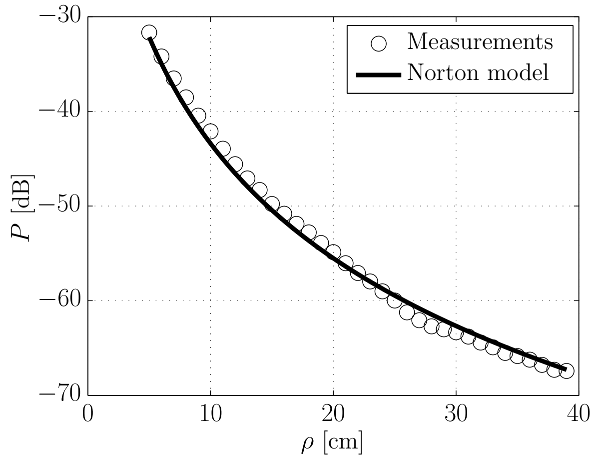

Figure 4.6: Measurement path loss with $h = z = 3$ mm and Norton model. The measurements and model have been normalized with the first measurement path loss.

The effect of each contribution (Geometrical Optics and Surface wave) is described in [61]. It can be concluded that Norton's equations are well suited to described the amplitude of the electric field above a dielectric surface.

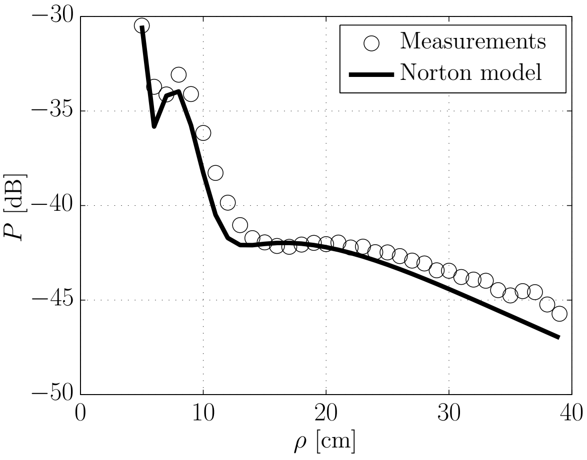

Figure 4.7: Measurement path loss with $h = z = 20$ mm and Norton model. The measurements and model have been normalized with the first measurement path loss.

4.1.4 On-Torso Path Loss

4.1.4.1 Channel Sounding

The experimental campaign has been conducted on a person, with the characteristics presented in table 4.1, in an anechoic chamber to avoid any environment influence. The male human subject is wearing a cotton t-shirt. An Agilent E8361C Vector Network Analyser (VNA) and U-Band open wave-guide antennas have been used. To reduce the losses in the cables and reduce their lengths, the VNA has been placed inside the anechoic chamber. A power amplifier with a gain of 30 dB at 60 GHz has been used at transmit side to raise link budget. The VNA has been used on continuous wave mode.

Measurements have been performed for both normal (to the body surface) and tangential (longitudinal to the body surface) polarizations, and for five distances between the antennas: 5, 10, 15, 20 and 25 cm. For each distance, we took different realizations of the measurements: vertical and horizontal links, with respect to the human body, were

Table 4.1: Physical quantities of the body

Quantity	Value
Gender	Male
Height	172 cm
Weight	60 Kg
Torso Perimeter	86 cm

investigated, so that for each distance and for each polarization forty measurements were taken. The positions have been chosen in order to have equal numbers of measurement on the chest and on the abdomen, as well as vertical and horizontal links. So, for example, for vertical polarization and for 5 cm between the antennas, we measured 10 vertical and 10 horizontal links on the chest, 10 vertical and 10 horizontal links on the abdomen. For 20 and 25 cm distances, vertical measurements correspond to 20 chest-abdomen links. For the distance 25 cm, tangential measurements have not been taken, since the torso of the PUT was not sufficiently large to obtain such distance. A scheme is shown in Fig. 4.8, where stars linked by a dashed line indicate a measure for a particular distance, place on the PUT and orientation of the link. We have schematically indicated chest and abdomen by an horizontal line representing the diaphragm.

Each measurement has been conducted during 10 seconds which is equivalent to 150 temporal acquisitions. The antennas were located at 2 cm from the body surface for both transmitter (TX) and receiver (RX) antenna. This choice permits to compare the influence of antenna body separation by comparison with [61]. The measurement parameters are summarized in table 4.2.

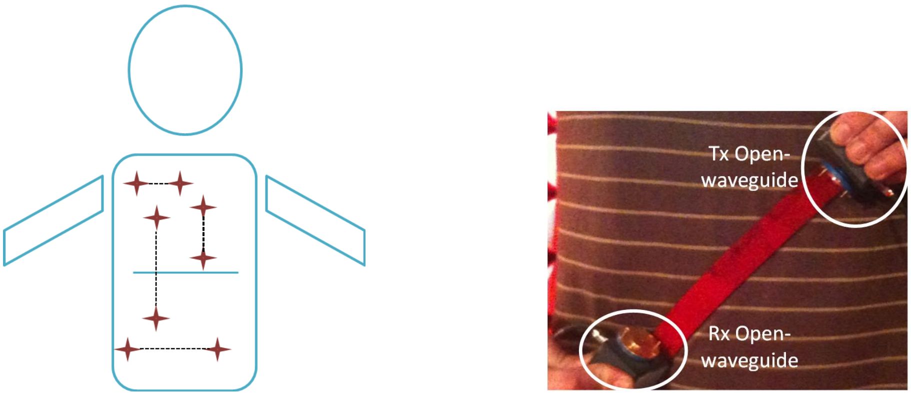

Figure 4.8: Measurement scheme. Stars correspond to measurement points on the front of torso. We depicted horizontal and vertical links of different lengths, on the chest, on the abdomen and one vertical chest-abdomen link. The horizontal line represents diaphragm and separate chest from abdomen. The photo shows the actual measurement set-up without the fixing band holding the antennas.

Table 4.2: Parameters of the measurement campaign

Symbol	Value
f	60 GHz
Measurement time	10 s
Acquisitions per measurement	150
Body-antenna distance	2 cm
Reference distances	5, 10, 15, 20 and 25 cm

4.1.4.2 Measurement Results

In the following, the experimental results are averaged over time and each measurement is presented as the mean value over the 150 time acquisitions.

Normal polarization The path loss for vertical and horizontal links for normal polarization are shown in Fig. 4.9 and Fig. 4.10 respectively.

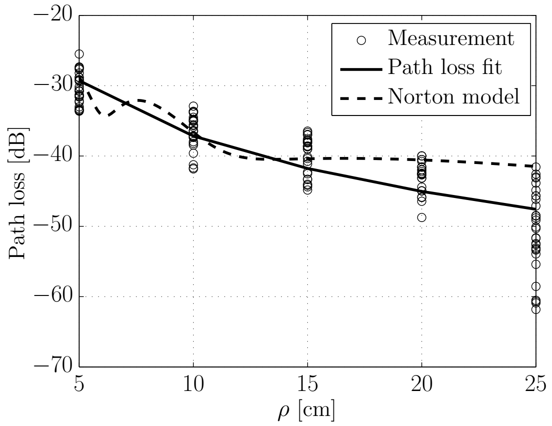

Figure 4.9: Path loss for normal polarization, vertical links. The dots stand for time averaged measurement and the solid line for the fitted path loss model (4.7).

The Norton path loss is also presented. It can be seen that this model is not well suited due to the oscillations created by the direct and reflected waves interference. This interference probably lead to the high standard deviation of the measured signal.

The path loss L_{dB} can be easily modeled with distance ρ as a logarithmic path loss :

$$L_{\mathrm{dB}}(d) = L^{0}_{\mathrm{dB}} + 10n \log_{10}(\rho/\rho_0) \tag{4.7}$$

where ρ_0 is a reference distance, L^0_{dB} is the path loss at d_0 and n is the path loss exponent. Shadowing can be modeled by a random variable following normal distribution, with zero mean and standard deviation σ_L. Standard deviation for vertical links is shown in Fig 4.13. We propose for both vertical and horizontal links two values of σ_L, depending on the distance range. Model parameters are summarized in Table 4.3.

It can be deduced that the electromagnetic waves attenuate faster for horizontal links. The reason is that for horizontal links, the surface of propagation is more curved than for vertical ones because of the human body shape, and therefore diffraction is more severe. Moreover,

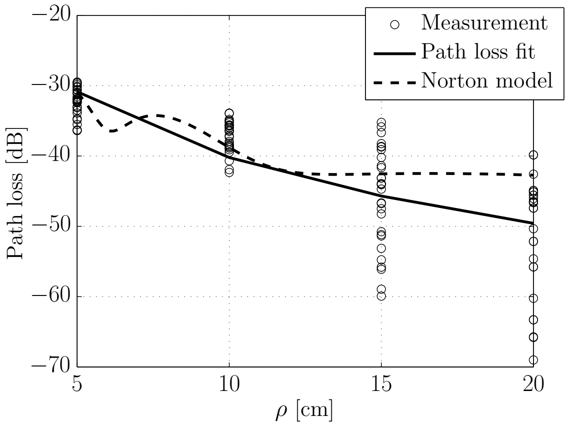

Figure 4.10: Path loss for normal polarization, horizontal links. The dots stand for time averaged measurement and the solid line for the fitted path loss model (4.7).

Table 4.3: Path gain parameters for vertical and horizontal links for normal polarization

Vertical links	Horizontal links
ρ_0=5 cm L^0=29.3 dB n=2.62	ρ_0=5 cm L^0=30.87 dB n=3.1
$\rho \leq$20 cm σ_L=2.36 dB	$\rho \leq$10 cm σ_L=2.13 dB
ρ =25 cm σ_L=5.85 dB	$\rho \geq$15 cm σ_L=7.68 dB

measurements are more scattered for horizontal links, which is also a consequence of diffraction. For vertical links, it can be considered that the main propagation mechanism is the sum of direct and reflected waves off the flat surface of the body between the antennas. Constructive and destructive interference between these two contributions can be significant.

In [61], a path loss exponent has been reported for a flat human phantom at 60 GHz. In that case, spacing between antennas and body surface was equal or smaller than 5 mm, and the path loss exponent for normally polarized waves ranges from 3.4 to 4. Choosing a greater, but still feasible, spacing between antenna and body surface as is proposed here, permits to reduce path loss exponent for normal polarization, even for horizontal links.

Tangential polarization The path loss for vertical and horizontal links for tangential polarization is shown in Fig. 4.11 and Fig. 4.12. Again, Norton's model is presented and the magnitude of the oscillations due to interference are higher than the normal polarization case. This probably creates a higher standard deviation than the other polarization.

Again, the path loss model is given by equation (4.7) and the path loss coefficients are given in Table 4.4. As compared to normal polarization, tangential polarization measurements show greater standard deviation, as is commonly found in lower frequency BAN channel measurements [77]. This can be explained by the reflected wave influence on the total received field, which, for tangential polarization, is more pronounced than for normal polarization [61]. For vertical links, the standard deviation linearly increases at the rate of 0.3 dB/cm, from a first value equal to 2.61 dB found at 5 cm. For horizontal links the trend is even worse, as it is shown in Fig. 4.13, due to the adverse effects of body curvature.

In [61], path loss for tangential polarization is described by $n = 4$ if the antennas are at the surface of the body phantom. Increasing the antenna height above the body up to 5 mm reduces the value of n, which is in accordance with our results.

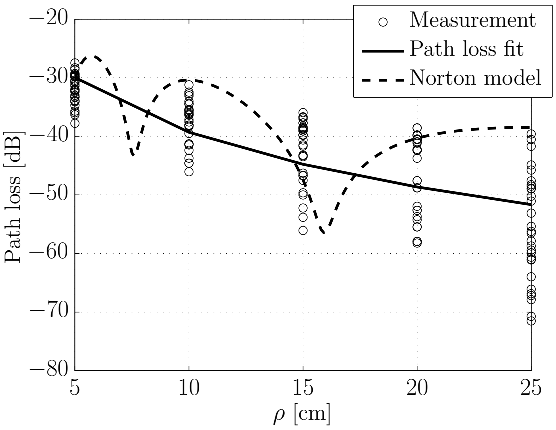

Figure 4.11: Path loss for tangential polarization, vertical links. The dots stand for time averaged measurement and the solid line for the fitted path loss model (4.7).

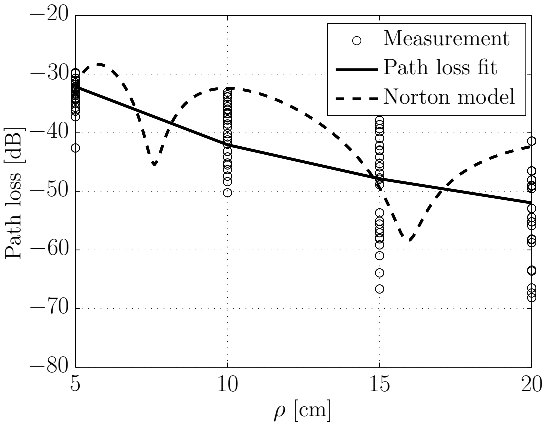

Figure 4.12: Path loss for tangential polarization, horizontal links. The dots stand for time averaged measurement and the solid line for the fitted path loss model (4.7).

4.2 Around Torso Propagation

4.2.1 Introduction

To completely model the on-body propagation, we propose to evaluate the path gain in the case of non-line-of-sight communication. This kind

Table 4.4: Path gain parameters for vertical and horizontal links for tangential polarization

Vertical links	Horizontal links
ρ_0=5 cm	ρ_0=5 cm
L^0=29.98 dB	L^0=32.14 dB
n=3.10	n=3.29
$\rho \geq$25 cm	$\rho \leq$10 cm
σ_L=2.61+0.3(d-5) dB	σ_L=3.77 dB
	$\rho \geq$15 cm
	σ_L=8.27 dB

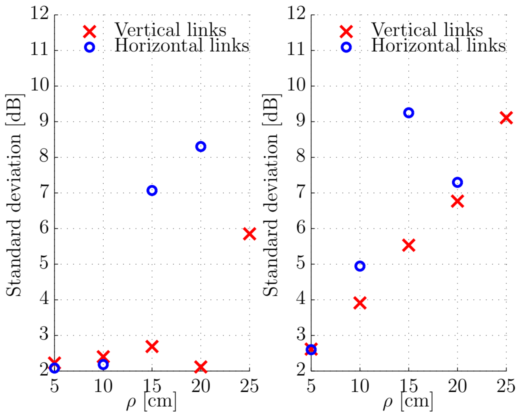

Figure 4.13: Standard deviation for normal and tangential polarizations. The dots stand for vertical measurements and the crosses for horizontal links.

of scenario often appears when devices are placed around torso.

We propose a model based on creeping wave theory to predict the attenuation of normally and tangentially polarized electromagnetic waves around the human torso at 60 GHz. After recalling creeping formulation for the Hertzian dipole radiating above a conducting cylinder, we show measurement results to confirm close-form results. Finally, we derive a linear path gain expression permitting to predict the attenuation of normally or tangentially polarized electromagnetic fields propagating on a circular path around a cylinder having the electromagnetic properties of a human body for frequencies around 60 GHz.

4.2.2 Cylindrical Body model

4.2.2.1 Geometry

We are interested in the propagation around a circular path on the surface of the cylinder, thus both source and observation points will be assumed to lie on a $z = 0$ constant plane. The distance between source and observation points will be indicated as $\rho_s = \phi a$, where ϕ is the angle measured between the source and the observation points. Creeping waves formulations will be adopted to calculate the field excited by Hertzian dipoles located near the surface of the cylinder.

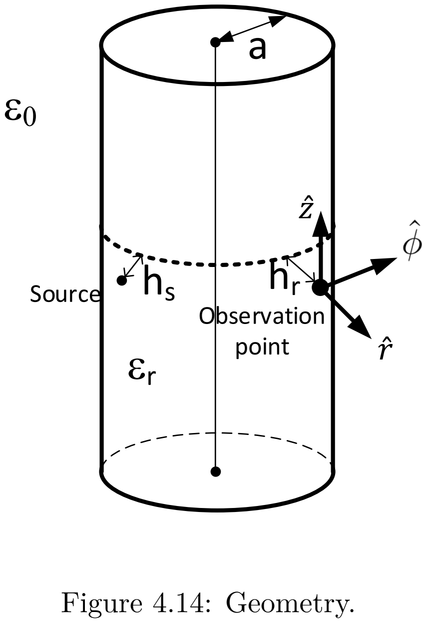

Figure 4.14: Geometry.

4.2.2.2 Hertzian dipole formulation

Dating back to electromagnetic wave propagation on the surface of the Earth studies [78], analytic expressions were originally intended to be applied for a Hertzian dipole radiating at the surface of a large (compared to wavelength) lossy sphere. However, Paknis showed that the same formulations could model propagation of electromagnetic waves on a circular path around a lossy cylinder [79].

The hypotheses permitting to adopt this model are that the radius of the cylinder is larger than free space wavelength and that the complex permittivity of the material filling the cylinder is much larger than unity. Both conditions are fulfilled in the scenarios considered in this thesis. It is assumed that both h_s and h_r are smaller than the distance between the antennas ρ_s [80].

Normal dipole Let a Hertzian dipole placed in the air close to the surface of the cylinder with its axis oriented along the ρ direction. We define this case as the vertical configuration in analogy with most of the literature [81, 82]. The electric field close to the surface of the cylinder has a ρ component and a negligible ϕ component, while the magnetic field is directed towards $\hat{z}$. The electric field is then normally polarized with respect to the surface of the cylinder and the ρ component (which we call E_n) of the electric field is [79]:

$$E_n = \frac{\mathrm{j}\,\omega\mu_0 I dl}{2\pi}\frac{e^{-\mathrm{j}\,\omega\rho_s/c}}{\rho_s}e^{-\mathrm{j}\,\pi/4}\sqrt{\pi\xi}\sum_{i=1}^{\infty}\frac{F(h_s)F(h_r)}{\tau_i - q_n^2}e^{-\mathrm{j}\,\xi\tau_i} \tag{4.8}$$

with

$$F(h) \simeq \frac{W_2\left(\tau_i - \sqrt[3]{\frac{2}{k_0 a}}k_0 h\right)}{W(\tau_i)} \tag{4.9}$$

$$\xi = \sqrt[3]{\frac{\omega a}{2c}}\frac{\rho_s}{a} \tag{4.10}$$

$$q_n = -\mathrm{j}\sqrt[3]{\frac{\omega a}{2c}}\sqrt{\frac{1}{\varepsilon_r}} \tag{4.11}$$

and τ_i are the zeros of

$$W_2'(\tau_i) - q_n W_2(\tau_i) = 0 \qquad i = 1, 2, ... \tag{4.12}$$

$F(h)$ is the "height-gain" function. Equation (4.8) is commonly known as creeping wave and it is an evanescent wave. For a source radiating close to the surface of the cylinder, two creeping waves traveling in opposite directions have to be taken in account and then the total field is:

$$E_T = E_n(\phi) + E_n(2\pi - \phi) \tag{4.13}$$

Tangential dipole Let a Hertzian dipole placed in the air close to the surface of the cylinder with its axis parallel to the $\hat{z}$ direction. We define this case as the tangential configuration. The case of a Hertzian dipole placed parallel to the z axis on the surface of the cylinder is much more complicated than the previous one, since all of the six components of the electromagnetic fields are involved [81]. We are only interested in the fields propagating around the cylinder in the plane $z = 0$, which is the direction perpendicular to the axis of the dipole. In this case, only the transverse component of the electric field is involved and the electric field is then tangentially polarized (or TE polarized). Formulations similar to the previous case have been given in [80] and, with the same notations introduced above, the ϕ component of the electric field at the surface of the cylinder (which we name E_t) is:

$$E_t = \frac{\mathrm{j}\,\omega\mu_0 I dl}{2\pi} \frac{e^{-\mathrm{j}\,\omega\rho_s/c}}{\rho_s} e^{-\mathrm{j}\,\pi/4} \sqrt{\pi\xi} \sum_{i=1}^{\infty} \frac{L(h_s)L(h_r)}{\tau_i' - q_t^2} e^{-\mathrm{j}\,\xi\tau_i'} \tag{4.14}$$

with

$$L(h) \simeq \frac{W_2\left(\tau_i' - \sqrt[3]{\frac{2}{k_0 a}} k_0 h\right)}{W_2(\tau_i')} \tag{4.15}$$

$$q_t = -\,\mathrm{j}\,\sqrt[3]{\frac{\omega a}{2c}} \sqrt{\varepsilon_r} \tag{4.16}$$

and τ_i' are the zeros of

$$W_2'(\tau_j') - q_t W_2(\tau_j') = 0 \quad j = 1, 2, ... \tag{4.17}$$

$L(h)$ is the "height gain" function for tangential polarization.

4.2.3 Simulation Results

For small values of the travel distance ρ_s, as it is shown in Fig. 4.15, accurate results need several zeros of equation (4.17) to be taken in account. This was also found for the normal dipole. Indeed, for small distance, the source and observation points are still in line-of-sight and the surface can be assumed to be flat. Then, as expected, the creeping wave path loss converges towards the Norton's surface result.

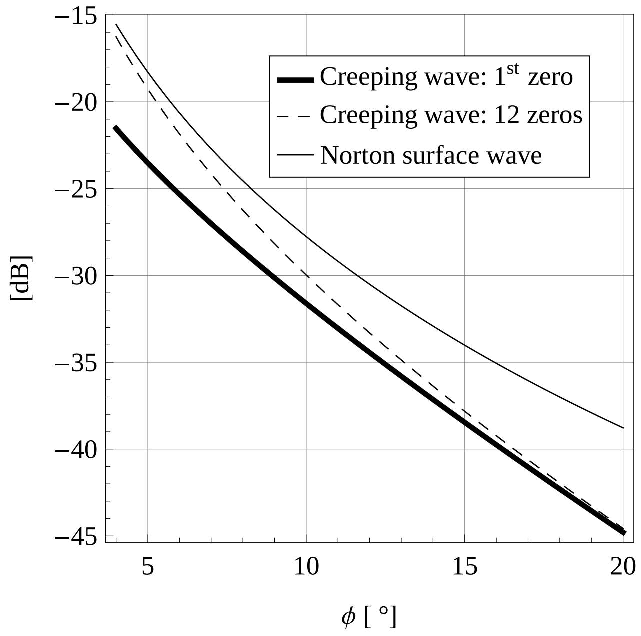

Figure 4.15: Tangential Hertzian dipole: magnitude of the ϕ component of the electric field at the surface of the cylinder for small radial distances from the source. $h_s = 1$ mm, $h_r = 1$ mm, $a = 0.2$ m.

The electric fields radiated at the surface of a conducting cylinder having the electromagnetic properties of human body at 60 GHz by both normal and tangential Hertzian dipoles are drawn in Fig. 4.16. Results have been computed using the twelve first terms of equations (4.8) and (4.14) and assuming that the observation point is at a height $h_r = 1$ mm above the surface of the cylinder, which has a radius equal as 0.2 m.

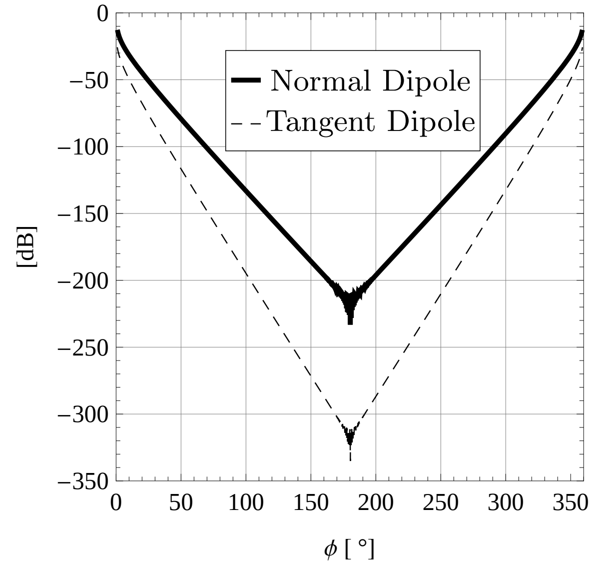

Figure 4.16: Hertzian dipoles: magnitude of the ρ component of the electric field radiated by a normal dipole and magnitude of the ϕ component of the electric field radiated by an tangential dipole as function of ϕ at the surface of a cylinder having radius equal as 20 cm and electromagnetic properties of the human body at 60 GHz. $h_s = 1$ mm, $h_r = 1$ mm.

4.2.4 Path Gain

In order to give a practical, ready to use approximation of the decay of the electric field on a circular cylinder having the electromagnetic properties of the human body around 60 GHz, two zones with respect to ρ_s

are first defined. The first one, $0 < \rho_s < \rho_s^T$, is the zone where the field radiated by a Hertzian dipole located close to the surface of the cylinder cannot be approximated by only the first term of (4.8) and (4.14). For values of ρ_s close to 0, a different expression of (4.8) and (4.14) as an inverse Laplace transform needs to be carried out (this result is given in [79]). Alternatively, as it has been shown in section 4.2.2.2, Norton formulations for planar interfaces can be used. In this zone, which we call planar zone, the precise evaluation of the field decay is strongly dependent on the height of the Hertzian dipole above the surface of the cylinder, mainly because the field reflected off the cylinder surface can add to the direct field constructively or destructively. Consequently, considering also that the planar zone is restricted to small radial distances from the source, the path gain in that region is derived from Norton's equation and can be found in section 4.1.

The second zone, $\rho_s > \rho_s^T$, is the curved zone where only a zero of (4.12) is needed to compute (4.8). Here, the field exponentially decays. In this second zone the observation point lies over the bend of the cylinder with respect to the source: in analogy with terrestrial propagation, it lies "over the horizon" and the field radiated by the source needs to be guided by the surface of the cylinder to reach it (no line of sight path exists between source and observation points lying in this zone).

In [81], ρ_s^T is defined as $\rho_s^T : \rho_s \gg a \sqrt[-3]{\frac{\omega a}{2c}}$ for source and observation points close to the interface between the air and the conductor. By taking into consideration the height of the source and the observation point, we have heuristically found that imposing $\rho_s^T = 0.4\ a$ is a good compromise for values of h_s and h_r smaller than 5 mm and for frequencies around 60 GHz.

In order to give a path gain expression of E_n in the curved zone, we have to simply note that for the first term in (4.8), the ρ_s dependency of the amplitude of E_n is:

$$|E_n(\rho)| = E_0 e^{\mathrm{Im}[\tau_1]\xi} / \sqrt{\rho_s} = E_0 e^{-m_n \rho_s} / \sqrt{\rho_s} \tag{4.18}$$

$$m_n = -\mathrm{Im}[\tau_1] \sqrt[3]{\frac{\omega a}{2c}} \frac{1}{a} \tag{4.19}$$

where $\mathrm{Im}[\tau_1]$ is the imaginary part of τ_1. Therefore, with respect to a reference distance $\rho_{s0} \geq \rho_s^T$, the path gain is:

$$G(\rho_s) = G(\rho_{s0}) - 10\log_{10}\left(\frac{\rho_s}{\rho_{s0}}\right) - n_n(\rho_s - \rho_{s0}) \tag{4.20}$$

$$n_n = 0.2m_n \log_{10}\mathrm{e} \tag{4.21}$$

In the above expressions, both ρ_s and ρ_{s0} are defined in cm and G is the path gain expressed in dB. n_n is the power decay exponent for normal polarization and it is expressed in dB/cm. It is worth noting that (4.20), with n_n computed using (4.21), it is exactly equivalent to E_n evaluated with only the first zero of (4.12). However, an approximate expression of (4.20) starting from a first order series expansion of the logarithm can be derived:

$$G(\rho_s) \simeq G(\rho_{s0}) - n_n'(\rho_s - \rho_{s0}) \tag{4.22}$$

with

$$n_n' = n_n + \frac{1.82}{\rho_{s0}} \tag{4.23}$$

The same derivation can be carried out for the path gain of tangentially polarized waves using equation (4.14) and defining a new power decay exponent n_t, which is:

$$n_t = -0.2\,\mathrm{Im}[\tau_1']\sqrt[3]{\frac{\omega a}{2c}}\frac{1}{a}\log_{10}\mathrm{e} \tag{4.24}$$

$$n_t' = n_t + \frac{1.82}{\rho_{s0}} \tag{4.25}$$

Path gain results are shown in Table 4.5 for $\rho_{s0} = \rho_s^T = 0.4\,a$: different values of the radius of the cylinder have been chosen and frequencies covering the world-wide available spectrum around 60 GHz are shown as well.

It is interesting to compare 60 GHz creeping wave attenuation with similar results obtained at 2.45 GHz [82]. For normal polarization, at 60 GHz the fields attenuate at the rate of nearly 3 dB/cm, while at 2.45 GHz the attenuation rate is only 0.73 dB/cm for a radius equal as 20 cm. Consequently, Table 4.5 represents useful insights for the power management and routing strategies of a 60 GHz BAN. With this information for example, the maximum distance between two nodes can be further determined according to the power dynamics and decoding capabilities of the devices.

Table 4.5: Path gain for normal and tangential polarization, for different frequencies and values of a (*n_n and n_t are expressed in dB/cm, σ is expressed in S/m. ρ_{s0} has been chosen equal as $\rho_s^T = 0.4\ a$)*

	a=0.10 m	$a = 0.15$ m	$a = 0.20$ m	$a = 0.25$ m
57 GHz				
$\varepsilon_r = 8.34$	n_n=4.10	n_n=3.29	n_n=2.82	n_n=2.50
$\sigma = 35.9$	n_t=6.67	n_t=5.11	n_t=4.23	n_t=3.65
58.5 GHz				
ε_r=8.15	n_n=4.16	n_n=3.34	n_n=2.87	n_n=2.54
σ =36.2	n_t=6.73	n_t=5.15	n_t=4.26	n_t=3.68
60 GHz				
ε_r=7.98	n_n=4.23	n_n=3.40	n_n=2.91	n_n=2.58
σ =36.4	n_t=6.78	n_t=5.20	n_t=4.30	n_t=3.71
61.5 GHz				
ε_r=7.81	n_n=4.29	n_n=3.45	n_n=2.96	n_n=2.62
σ =36.6	n_t=6.84	n_t=5.24	n_t=4.34	n_t=3.74
63 GHz				
ε_r=7.65	n_n=4.35	n_n=3.50	n_n=3.00	n_n=2.66
σ =36.8	n_t=6.89	n_t=5.28	n_t=4.37	n_t=3.77
64.5 GHz				
ε_r=8.51	n_n=4.42	n_n=3.55	n_n=3.05	n_n=2.70
σ =37.0	n_t=6.95	n_t=5.32	n_t=4.40	n_t=3.80
66 GHz				
ε_r=7.37	n_n=4.48	n_n=3.6	n_n=3.09	n_n=2.74
σ =37.2	n_t=7.00	n_t=5.36	n_t=4.44	n_t=3.83

4.2.5 Measurements

An experimental campaign has been carried out in an anechoic chamber to measure the field propagation at the surface of a cylindrical body. All measures were performed with an Agilent E8361C Network Vector Analyzer. Since large losses due to the coaxial cables have been founded at 60 GHz (6 dB/m), the Vector Analyzer is placed inside the anechoich chamber to limit the length of the cables feeding the field probes.

4.2.5.1 PEC measurements

In a first step we have chosen to compare the creeping wave model at 60 GHz with the field measured on a brass cylinder. To make the measurements, the brass cylinder has been vertically mounted on a rotor and could thereafter rotate around its axis. A photo of the experimental set-up can be found in Fig. 3.9. A pyramidal horn antenna has been used as electromagnetic waves radiator and fixed at the surface of the cylinder, at middle height, while a field probe has been realized by mounting a second identical antenna on a vertical stand. The probe was then placed as close as possible to the cylinder, at the same height as the source. The horn antennas are well suited to capture only the power coming from the creeping wave which allows to assess the model proposed in this section. The horn antenna allows to increase the dynamic range and decrease the effect of multipath components while it does not change the azimuthal behaviour of the received power. Different distances between source and probe are then achieved by commanding the rotor and so rotating the cylinder. Both polarizations are measured by turning 90 ° both horns on their axis. Relevant parameters of the measurement are summarized in Table 4.6 and a schematic representation of the measurement setup is drawn in Fig. 4.17.

In Fig. 4.18 we have reported the results of the measurement on the brass cylinder for both polarizations. By comparison with the predicted results obtained with the analytic expressions (4.8) and (4.14) computed using only the first term, it can be concluded that the field in the zone we have measured decays as a creeping wave on the surface of the cylinder. However, for TM polarization, the signal rapidly falls under the VNA

Table 4.6: Relevant geometrical parameters for brass cylinder measurements

Parameter	Symbol	Value
Cylinder radius	a	20 cm
Cylinder height		1 m
Angular step	$\Delta\theta$	10 °
Radial distance step	$\Delta\rho_s$	3.5 cm
Number of steps		9
Angular start value		38.7 °
Radial start value		13.5 cm

noise level threshold.

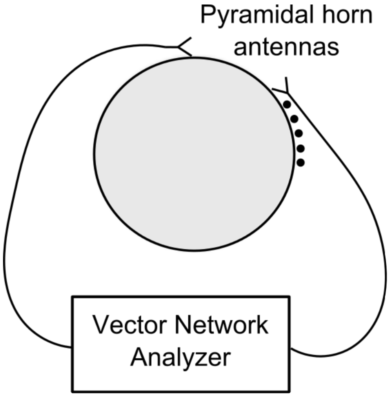

Figure 4.17: Measurement setup. Black dots indicate different measurements points.

4.2.5.2 Body measurements

A second measurement set up has been carried out in order to measure the field propagating around human torso as shown in Fig. 4.19. The aim of these measurements is to demonstrate that creeping wave formulations can be used to predict the attenuation of the field propagating at the surface of the torso in a circular path. However, two main difficulties were expected. First, we were of the opinion that if the source and

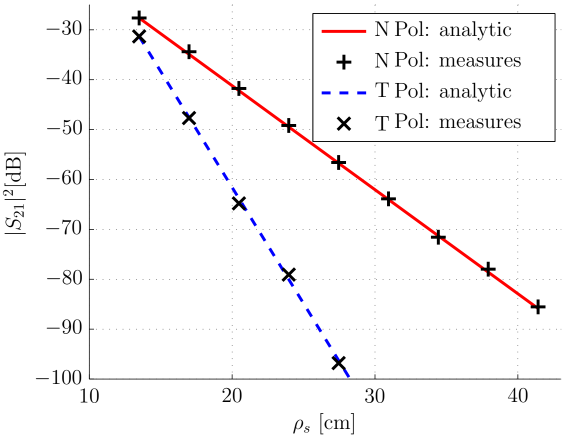

Figure 4.18: Normal and tangential polarization measurement results compared with analytical attenuation prediction for a PEC cylinder of radius a=0.2 m.

Figure 4.19: Photo of the measurement set-up around the human torso.

receiving probes were on the same side of the torso, then they are on line of sight and so planar formulations like Norton's ones should be used. Secondly, we were aware that the fast decay of the creeping wave

Table 4.7: Relevant geometrical parameters for human torso measurements

Parameter	Symbol	Value
Torso perimeter		0.9 m
Approximated radius	a	15 cm
Height of the subject		1.68 m
Radial distance step	$\Delta\rho_s$	1.5 cm
Number of steps		9
Source position		Left nipple
Radial start value		19 cm

would have limited the maximum distance from source and probe, for which measurements can be possibly conducted taking account power dynamics limitations. Consequently, we chose to measure the decay of the field radiated by a horn antenna (for the same reasons described in section 4.2.5.1) placed on the front side of the torso, approximately on the nipple, in the curved region of the torso itself, under the arm. is of these measurements.

The results of the measurement are plotted in Fig. 4.20 and 4.21. Although the measurements points fluctuate around the theoretical prediction line more than in the PEC case, the measurements confirm that the field decay on the curved zone of the torso can be modeled by a creeping wave.

4.2.6 Velocity of Creeping Waves

4.2.6.1 Creeping Wave Formulations

In the previous section, the creeping wave formulation has been calculated from radiation of a Hertzian dipole at the surface of a large dielectric cylinder.

It has been shown above that the first creeping wave mode is dominant and it can be written as:

$$E_{n,h} = c_{n,h} e^{-j(k+m\tau_{n,h}/a)\rho_s} \tag{4.26}$$

The complex coefficient $c_{v,h}$ depends on a, h_s, h_r and ω as can be

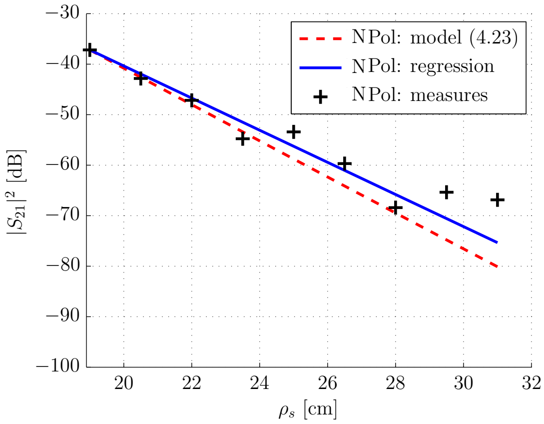

Figure 4.20: Normal polarization measurement results compared with the theoretical attenuation prediction on a human torso of radius a=0.15 m.

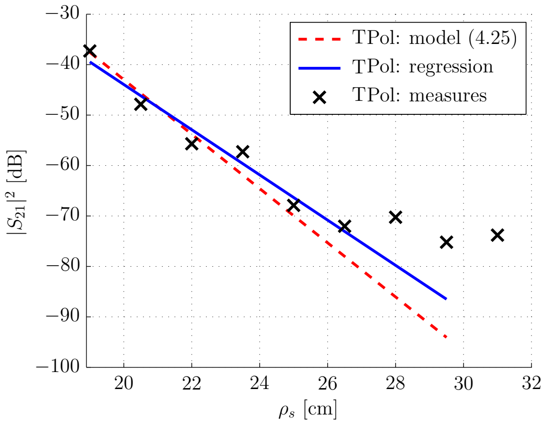

Figure 4.21: Tangential polarization measurement results compared with the theoretical attenuation prediction on a human torso of radius a=0.15 m.

found above. It is important to note that it also depends on ρ_s but only in magnitude (ρ_s have no impact on the phase).

4.2.6.2 Velocity Assessment and Numerical Study

The phase shift $\Delta\psi$ of a creeping wave propagating at a distance d can be easily derived from (4.26):

$$\Delta\psi = (k + m\mathrm{Re}(\tau_{n,t})/a)d \tag{4.27}$$

where Re(·) stands for the real part. Since the phase shift linearly varies with frequency, $\Delta\psi = \dfrac{2\pi f d}{v_\psi}$ [83], the phase velocity $v_\psi^{n,t}$ is given by :

$$v_\psi^{n,t} = \frac{2\pi f}{(k + m\mathrm{Re}(\tau)/a)} = \frac{c}{1 + \frac{m\mathrm{Re}(\tau_{n,t})}{ka}} \tag{4.28}$$

Equation (4.28) represents the phase velocity of a creeping wave around a circular cylinder. Basically, the phase depends on two parameters: the radius a and the frequency f. The term m/ka is trivial to evaluate since it is algebraic. However, the phase velocity also depends on the term $\mathrm{Re}(\tau_{v,h})$ which is not straightforward to calculate since $\tau_{v,h}$ is the solution of (4.12) or (4.17). In the following, it is proposed to numerically evaluate $\mathrm{Re}(\tau_{v,h})$ over the bandwidth. These simulations are conducted for a cylinder having the same permittivity as the human skin and a PEC cylinder.

The result is presented in Fig. 4.22. It is important to notice that the permittivity of the human skin is with frequency [3]. In the case of a PEC cylinder, the variation of both τ_n and τ_t is less than 0.01%.

The variation of $\mathrm{Re}(\tau_{n,t})$ in the case of the human skin is maximum for the normal polarization and is about 2%. However, this variation is also negligible. Using basic propagation of uncertainty theory, it can be trivially inferred that this 2% variation creates, on average, 0.04% error on the phase velocity. Then, in the following, the values of $\tau_{v,h}$ will be considered as constant over the whole bandwidth.

Since change of $\mathrm{Re}(\tau_{n,t})$ over the bandwidth is negligible, it can be numerically shown that the maximum variation over the V-band of the phase velocity (equation (4.28)) is about 0.5%. Hence, the phase velocity can be considered as constant over the bandwidth. Table 4.8 summarize the $\tau_{n,t}$ parameter and related phase velocities.

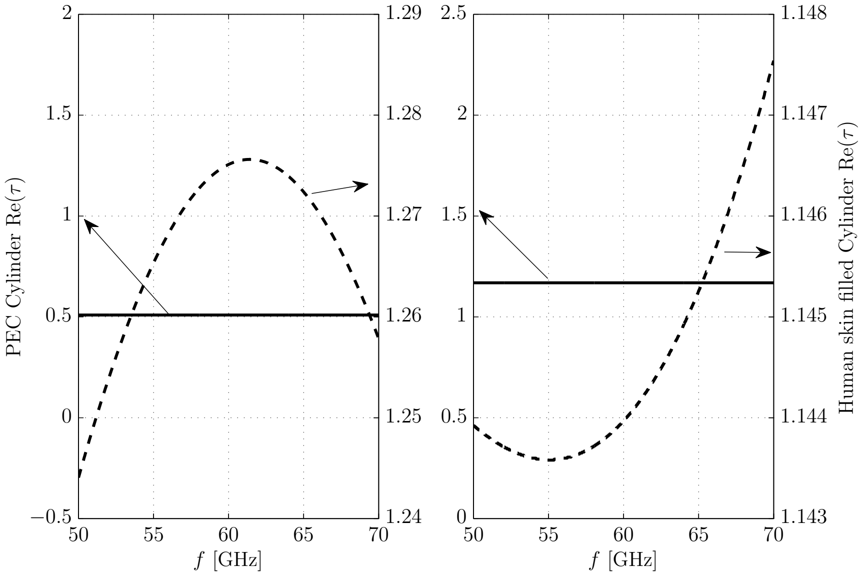

Figure 4.22: Variation of the real part of τ_n (left) and τ_t (right) on the V-band with $a = 0.2$ m. PEC cylinder result corresponds to the plain curve reported on the left axis while the cylinder having the same permittivity as the human skin to the the dotted line reported on the right axis.

Table 4.8: Mean values of $\tau_{n,t}$ and v_ψ over the V-band for a PEC and a human skin filled cylinders.

a [m]	$\mathrm{Re}(\tau_n)^{\mathrm{Skin}}$ $\mathrm{Re}(\tau_n)^{\mathrm{PEC}}$	$(v_\psi^n)^{\mathrm{Skin}}$ [m/s] $(v_\psi^n)^{\mathrm{PEC}}$ [m/s]	$\mathrm{Re}(\tau_t)^{\mathrm{Skin}}$ $\mathrm{Re}(\tau_t)^{\mathrm{PEC}}$	$(v_\psi^t)^{\mathrm{Skin}}$ [m/s] $(v_\psi^t)^{\mathrm{PEC}}$ [m/s]
0.15	1.219	2.911×10^8	1.154	2.918×10^8
	0.509	2.962×10^8	1.169	2.916×10^8
0.2	1.227	2.924×10^8	1.155	2.932×10^8
	0.509	2.968×10^8	1.169	2.930×10^8
0.25	1.232	2.934×10^8	1.156	2.941×10^8
	0.509	2.973×10^8	1.169	2.940×10^8
0.30	1.234	2.940×10^8	1.157	2.947×10^8
	0.510	2.976×10^8	1.169	2.946×10^8

It is important to note again that the variation of $\tau_{n,t}$ is negligible with the radius of the cylinder a.

4.2.6.3 Experimental Velocity estimation method

In [84], a frequency correlation analysis for wideband signals is proposed to evaluate the phase velocity of on-body waves. The correlation is estimated between two observation locations noted 1 and 2 spaced by a distance d. The complex correlation ρ is given by:

$$\rho = \frac{E[S_1 S_2^*]}{\sqrt{E[|S_1|^2]E[|S_2|^2]}} \tag{4.29}$$

where S_1 and S_2 are the frequency channel transfer functions between the source and the observation points 1 and 2, * denotes the complex conjugate operation and $E[]$ stands for the mean value that averages channel realizations.

The phase $\Delta\psi$ of this correlation linearly varies with frequency [83] and it can be written as:

$$\Delta\psi = \frac{2\pi f}{v_\psi} d \tag{4.30}$$

where v_ψ is the phase velocity. The method proposes to estimate the coefficient $(2\pi d / v_\psi)$ for different distances d. Then, using the obtained coefficient with d, the phase velocity can be easily obtained. This method will be used in the following in order to assess analytically and experimentally the phase velocity of a creeping wave.

To assess the validity of the proposed model, two measurement campaigns have been conducted. The first one has been realized using a perfectly conducting (PEC) cylinder in order to precisely verify the theoretical path gain. The second campaign has been conducted on a human. Its purpose was to evaluate the validity of the model to emulate a real body though it has been developed for a cylinder.

4.2.6.4 PEC Measurement Campaign

Experimental Set-up The measurements were conducted with an *Agilent E8361C VNA* and U-band horn antennas (20 dB gain) in an anechoic chamber. To increase the dynamic range, two amplifiers have been used (the first at the transmitter side and the second at the receiver side).To make the measurements, the brass cylinder has been vertically mounted on a rotor and could therefore rotate around its axis. The measurements have been performed from 0 ° to 90 ° with a 10 ° step. A pyramidal horn antenna has been used as electromagnetic waves radiator. The antenna has a gain of 20 dB and a beamwidth of 10°. The aperture size is 2.3 cm x 3 cm. It has been mounted directly on the surface of the cylinder, at middle height. A field probe has been realized by fixing a second identical antenna on a vertical stand. The probe was then moved at the surface of the cylinder, at the same height as the source. The receiving (Rx) and transmitting (Tx) horn antennas were placed tangentially to the cylinder to maximize the amount of power received from the creeping wave. The cylinder had a 0.2 m radius, a height of 1.2 m and the Rx horn antenna was placed at middle height. The measurements have been conducted from 50 to 60 GHz with a 66.67 MHz step. The IFbandiwdth of the VNA was 1 Hz in order to have the highest dynamic range possible.

The coaxial cables have about 6 dB/m losses. To avoid the need of long distance cables and maximize the received power, the VNA was put inside the anechoic chamber and covered by absorbing material. Time gating has been performed to increase the dynamic range.

Results The method presented in section 4.2.6.3 was used on the measurements. The phase of the correlation is drawn in Fig. 4.23 for two particular values as example. As expected, the phase linearly varies with respect to the frequency. For each couple of measurements positions, the slope of the curve is calculated and presented in Fig. 4.24. This latter is analytically equal to $2\pi f d/v_\psi$.

This allows to easily obtain the phase velocity of the creeping wave since the slope is given with the distance d. The dynamic range for normal polarization being higher than for tangential polarization, measurements have been restricted for shorter distances in the tangential case.

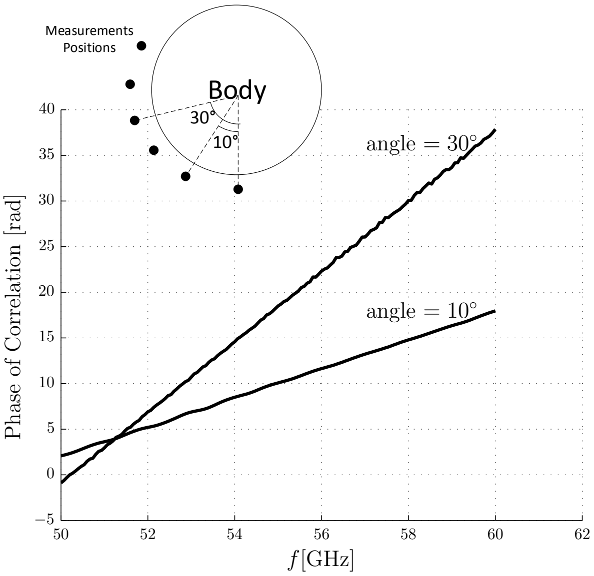

Figure 4.23: PEC measurements. Exemple of measurement results for normal polarization. Phase of the correlation with the frequency.

The slope of these curves is theoretically equal to $2\pi f/v_\psi$. Hence, the phase velocity v_ψ can be directly obtained from these figures.

Finally, in table 4.9, the theoretical and measured phase velocities are summarized. It can be shown that the comparison between the measurements and the theoretical model shows an relative error of less than 1%. These results allowed to assess the validity of the equations presented in section 4.2.6. However, since the model is developed for body area networks, it is necessary to evaluate the accuracy of these equations on a real human body.

4.2.6.5 Human Measurement Campaign

Experimental Set-up The measurements were conducted using a *Rhode & Schwarz ZVA-Z7* in a semi-anechoic room. Two V-band (1.85 mm) cables of 1 meter have been used with 10 dB of losses. To optimize the dynamic range, a 30 dB Low Noise Amplifier has been placed at the

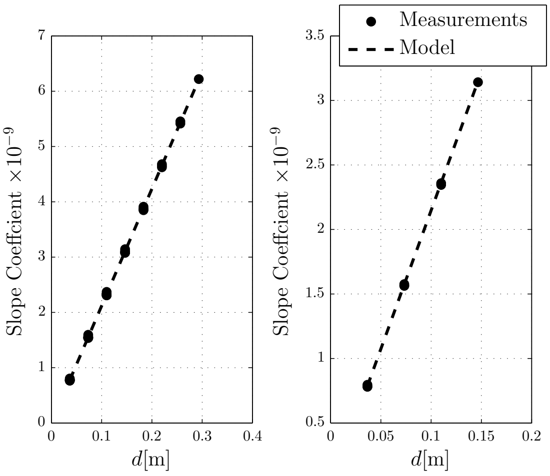

Figure 4.24: Slope of the phase with the frequency for each distance in normal (left) and tangential (right) polarizations.

Table 4.9: PEC measurements. Comparison between measured and theoretical phase velocities.

	Normal Polarization	Tangential Polarization
Theoretical	2.967 $\times 10^8$ m/s	2.926 $\times 10^8$ m/s
Measured	2.969 $\times 10^8$ m/s	2.935 $\times 10^8$ m/s
Relative Error	0.08%	0.33%

Table 4.10: Relevant Parameters for the real human measurement campaign

Parameter	Value
f_{start}	55 GHz
f_{stop}	65 GHz
f_{step}	50 MHz
VNA IFbandwidth	1 kHz
VNA Averaging	1
Stomach Perimeter	0.8 m
Equivalent Raduis	12 cm
Height of the subject	1.68 m
Gender	Male

receiver side. The transmitting and receiving antennas were standards V-band horns with 10 dB of gain. The measurements parameters and the human characteristics are summarized in Table. 4.10.

The measurements have been carried out around the stomach of the subject and for each distance a collection of 10 measurements have been obtained and averaged. The channel has been obtained at each centimeter from 3 to 11 cm and the antennas have been placed on a belt explicitly designed for this measurement campaign. Time gating has been used to isolate the creeping wave contribution.

Results The results are presented in Fig. 4.25. It can be seen that the measurement linearly varies with distance. The theoretical slope has been obtained by using the formulation (4.28), and measurement fitting is obtained by minimizing the least squares error.

As can be observed in Table 4.11, the relative error between the theoretical model and the measured velocity is between 2 and 3.5%. This can be easily explained by the human body geometry around the stomach which is not an exact circular cylinder. However, as seen, the circular cylinder is a good approximation of the human body for propagation around the human stomach.

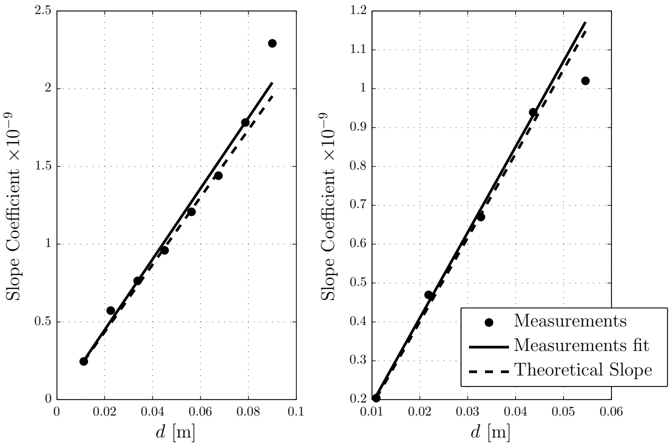

Figure 4.25: Real Human measurements for normal (left) and tangential (right) polarizations. Slope of the phase with the frequency for each distance in tangential polarization. The measurements with enough dynamic range have been kept.

Table 4.11: Real Human measurements. Comparison between measured and theoretical phase velocities.

	Normal Polarization	Tangential Polarization
Theoretical	2.899×10^8 m/s	2.906×10^8 m/s
Measured	2.799×10^8 m/s	2.846×10^8 m/s
Relative Error	3.57%	2.10%

4.3 Millington Effect for Propagation enhancement

4.3.1 Objective

The high propagation losses obtained in the previous sections are a critical issue for on-body communication systems, and recent studies have been proposed to tackle this problem. In [63], an electro textile covering the skin between the transmitter and receiver is used to improve the wave propagation along human body.

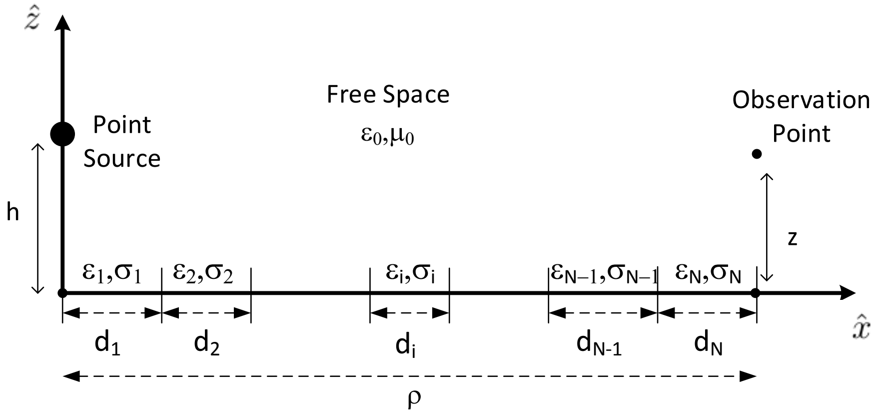

Figure 4.26: Millington scheme geometry. The flat surface is split up into N segments with different electrical properties. The propagation between the point source and the observation point is studied.

In this section, we propose a more realistic scenario in which only some body parts are covered with an electro textile or metallic inserts. Millington equations are used to analytically investigate this problem. Propagation above mixed propagation paths has been solved using a combination of Norton's equation [81] by G. Millington [85, 86] to study propagation above an assumed flat sea taking into account the presence of islands. We propose here to use the Millington equations for 60-GHz BANs. Since it has been shown in [63] that path loss above a lossy dielectric surface is higher than above a conducting surface, we propose to artificially create mixed paths composed of skin and metallic sheets, with the aim to improve the link budget without covering all surfaces with a metallic layer.

4.3.2 Analytical Model

4.3.2.1 Geometry under study

The human body is assumed to be a flat lossy half space in free space. As presented in Fig. 4.26, the flat surface modelling the human body is split into N homogeneous regions, where d_i denotes the length of i^{th}

region in the propagation direction $\hat{x}$. The relative complex permittivity of each dielectric region is given by $\varepsilon_i^c = \varepsilon_i - j\sigma/\omega\varepsilon_0$, with ε_i the real relative permittivity and σ_i the conductivity of i^{th} segment. All regions are assumed to be non-magnetic (permeability μ_0). The source and observation points are vertically-polarized elementary dipoles with current I and equivalent height l. Hence, only the z-component (normal to the surface) of the electric field is considered in the following since it has been shown in [61, 87] that the vertical polarization is dominant in on-body propagation and that the x- and y-component of the electric field are negligible with respect to the z-component. The source dipole and the observation point are placed along $\hat{z}$ at heights h and z above the body surface, respectively. In the following, a special focus is given to 3-segment surfaces. These segments are assumed to be either human skin or perfect electrical conductor (PEC). The human skin is assumed to have a real relative permittivity of $\varepsilon = 7.98$ and a conductivity $\sigma = 36.4$ S/m [3].

Norton's equation is evaluated at 60 GHz in Fig. 4.27 for human skin and PEC surfaces with $I \times l = 1$ A.m and for $h = z = 3$ mm. It can be inferred, as in [61, 63], that the path loss exponent is equal to 2 and 4, for propagation over PEC and skin surface respectively. This property will be used in the following to enhance propagation over the body using small-size PEC inserts, as described by Millington.

4.3.2.2 Millington Effect

Millington [85] discovered for the first time signal attenuation and recovery at sea-land transitions in the HF band. He introduced a generic approach to determine the power level above an inhomogeneous surface: the recursive equations of the Millington Curve Fitting Method (equations (4.31) to (4.35)). These equations are reminded here for sake of completeness. Millington proposed to calculate the direct and reversed powers P^{D} and P^{R} (in dB) as follows

$$P^{\text{D}} = \sum_{i=1}^{N} P_i(s_i) - \sum_{i=2}^{N} P_i(s_{i-1}) \tag{4.31}$$

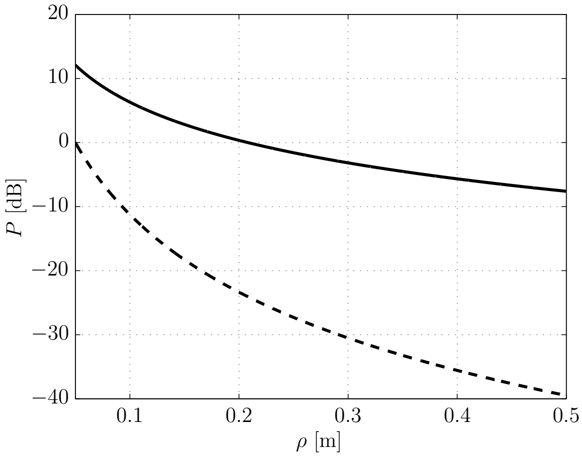

Figure 4.27: Power $P = 20\log_{10}|E_z|$ on a flat surface. Comparison between PEC (plain curve) and skin (dotted curve) surfaces. The curves have been normalized to have a 0-dB for path loss over skin surface at 5 cm distance from the point source.

$$P^{\mathrm{R}} = \sum_{i=1}^{N} P_i(r_i) - \sum_{i=2}^{N} P_{i-1}(r_i) \tag{4.32}$$

With

$$s_i = \sum_{n=1}^{i} d_n \tag{4.33}$$

$$r_i = \sum_{n=1}^{i} d_{N-n+1} \tag{4.34}$$

The total field strength P_{tot} is then given by

$$P_{\mathrm{tot}} = \frac{1}{2}(P^{\mathrm{D}} + P^{\mathrm{R}}) \tag{4.35}$$

In these equations, $P_i(x)$ is the power in dB at the homogeneous i^{th} segment at distance x and it can be noted that the distance $\rho = \sum_{n=1}^{N} d_n$. If a 3-path scenario is considered, it can be written that

$$\begin{aligned} P^{\mathrm{D}} =& P_1(d_1) - P_2(d_1) + P_2(d_1 + d_2) \\ &- P_3(d_1 + d_2) + P_3(d_1 + d_2 + d_3) \end{aligned} \tag{4.36}$$

and the reversed field strength P_r as

$$\begin{aligned} P^{\mathrm{R}} = & P_3(d_3) - P_2(d_3) + P_2(d_3 + d_2) \\ & - P_1(d_3 + d_2) + P_1(d_1 + d_2 + d_3) \end{aligned} \tag{4.37}$$

4.3.3 Experimental Results

Measurements have been conducted in a semi-anechoic environment using a *Rhode & Schwartz* Vector Network Analyzer (VNA), with 101 equally spaced frequency points spanning from 55 to 65 GHz. The IF bandwidth has been set to 10 Hz and the transmitter power to 0 dBm. Time gating has been performed to remove multipath effects. A photograph of the measurement set-up is provided in Fig. 4.28.

The propagation surface is a flat body phantom whose electric properties have been presented in [18]. In order to measure the field strength over the propagation surface, open-ended vertically-polarized WR-15 waveguides without flanges are used as transmitting and receiving antennas. The receiving waveguide is mounted on a numerically-controlled positioner. The path loss has been measured over a distance between the transmitting and receiving waveguides ranging from 5 to 50 cm. The waveguide apertures are located about 3 mm above the surface ($h = z = 3$ mm, in Fig. 4.26).

Seven measurement scenarios have been considered, as summarized in Table 4.12; they are based on different combinations of PEC/phantom segments. Metallic inserts have been used in practice for PEC regions; the strip width is fixed (5 cm), whereas their lengths vary, as reported in Table 4.12. Further transmission measurements have shown that wider strip widths do not lead to significant changes in the results. Scenario 0 is defined as the reference one since it corresponds to propagation over a homogeneous flat human skin. The corresponding measured and analytical results are shown in Fig. 4.29; the measured path loss at a distance of 5 cm between the transmitter and receiver is in the range of values obtained in [61] (between -34 and -40 dB attenuation).

Each analytical curve has been normalized with respect to the first measurement. It is the only conducted fitting process in order to compare the model and the measurements. Fig. 4.29 presents path loss as

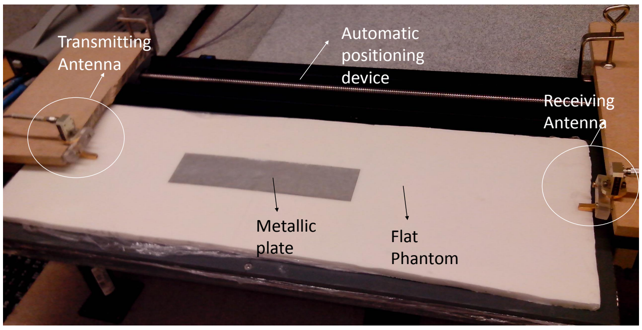

Figure 4.28: Photo of the experimental set-up.

Table 4.12: Measurement set-ups

Measurement scenario	set-up		
Scenario 0		Skin	
		50 cm	
Scenario 1	Skin	PEC	Skin
	10 cm	10 cm	30 cm
Scenario 2	Skin	PEC	Skin
	10 cm	20 cm	20 cm
Scenario 3	Skin	PEC	Skin
	20 cm	10 cm	20 cm
Scenario 4	PEC	Skin	
	10 cm	40 cm	
Scenario 5	Skin	PEC	
	40 cm	10 cm	
Scenario 6	PEC	Skin	PEC
	10 cm	30 cm	10 cm

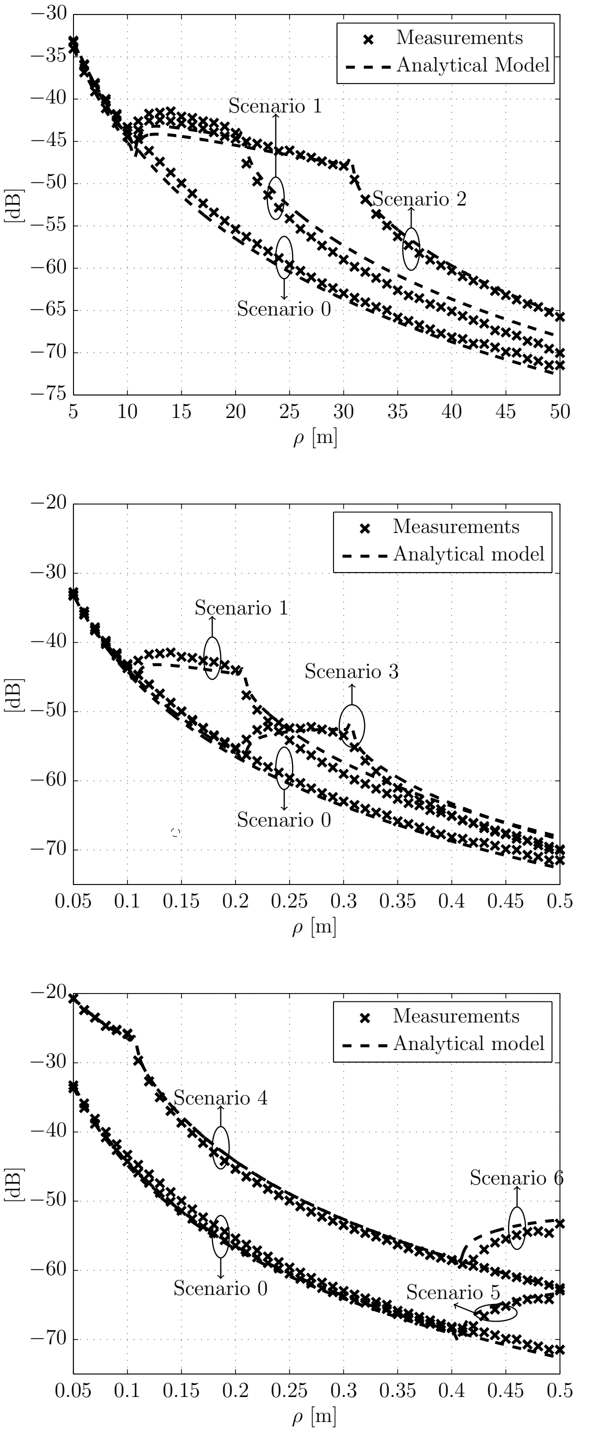

Figure 4.29: Measured and simulated path gains for the different scenarios. Dotted curves refer to transmission coefficients computed using Norton's or Millington formulations assuming the transmitting and receiving antennas are placed 3 mm above the phantom. Curves with markers correspond to measurements.

a function of the distance ρ when inserting a metallic surface between the transmitter and receiver for the different scenarios summarized in Table 4.12. The slope change in the path loss decay is clearly visible at ρ values for which the propagation is on the PEC. It is clearly shown that this effect results in a decrease of the overall path loss. The experimental results are in very good agreement with the analytical model and demonstrate that adding a PEC insert allows improving the propagation over the body. This model leads to the results achieved by [63] which showed that covering all the propagation surface with an electro textile increases the link budget. Fig. 4.29 demonstrated the role of the location of the metallic plate under the antennas. It is shown that in this case the gain is higher compared to other scenarios.

Discrepancies between theoretical and experimental results show a maximum absolute error of 2.74 dB (for scenario 6) and a mean absolute error of 1.33 dB (for scenario 1). These errors are mainly due to the imperfections of the phantom surface. During the experiments, it has been observed that the antenna was not always at the exactly same height above the surface for different ρ distances. A variation of height of maximum 1 mm has been observed during the measurement campaign. However, measurements and theory are sufficiently similar to validate the theoretical model.

4.3.4 Numerical Study and Discussion

The analytical model can be used in order to determine the minimum path loss achievable with scenarios described in Table 4.13 and Fig. 4.26. The objective is to optimize the path loss reduction (gain factor) G with and without the use of a metallic plate. In subsection 4.3.3, we assumed that z and h are equal to 3 mm to experimentally validate the analytical model. Here we also study the impact of the height of the antennas on G. The maximum distance $\rho = d_1 + d_2 + d_3$ is considered to be 50 cm which is a typical link length that can occur in BAN [33]. Hence, the gain factor G will be defined as:

$$G = P^{\text{With PEC}}(\rho = 0.5 \text{ m}) - P^{\text{Without PEC}}(\rho = 0.5 \text{ m}). \tag{4.38}$$

Table 4.13: Medium per region for the two different schemes

Scheme	Region 1	Region 2	Region 3
1	Skin	PEC	Skin
2	PEC	Skin	PEC

4.3.4.1 Considered Schemes

The first scenario studies the effect of a metallic plate placed between the two antennas. It is called “Skin-PEC-Skin”. This scenario is interesting in the field of topology studies and relay device location in BAN [88]. The idea is to replace complex relay devices made up receiver and transmitter by a simple metallic plate if the achieved gain is sufficient.

The second scenario analyses the propagation when the transmitting and receiving antennas are placed above a metallic plate. It is called “PEC-Skin-PEC”. This scheme allows to analytically study the gain factor obtained with the size of the ground plane placed under the antenna. Millington formula here allows one to tackle this problem from the propagation point of view.

4.3.4.2 Scheme 1: Skin-PEC-Skin

Scheme 1 studies the influence of a PEC between the transmitter and receiver placed on the human body. This PEC insert acts as a “repeater", having a gain factor proportional to its length (Fig. 4.29). In the following, only the sizes d_1 and d_2 of the skin region and the length of the PEC region are discussed.

Fig. 4.30 shows that G increases with the length of the metallic plate as expected. Also G increases by placing the metallic insert closer to the transmitter. By reciprocity, the same curves as in Fig. 4.30 can be obtained by replacing d_1 by d_3. These results only suggest that the gain factor is higher when approaching the surface to the antennas and this scenario will be consequently further investigated in the next subsection (scheme 2).

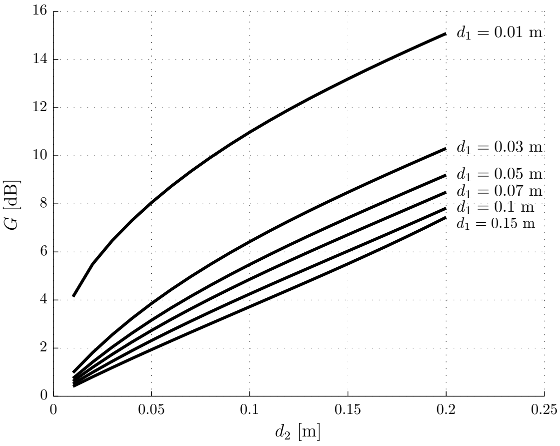

Figure 4.30: Scheme 1. Computed gain factor values G obtained by adding a PEC plate of length d_2 with $h = z = 3$ mm, for various values of d_1 (distance between the transmitting antenna and PEC plate).

Fig. 4.31 demonstrates the impact of h and z on the gain factor G. The metallic plate is placed between the two antennas so that $d_1 = d_3 = 0.25 - d_2/2$. This situation is not optimal as can be seen in Fig. 4.31 but allows us to analyze the impact of modifying the parameter d_2 only. These curves show that G is higher when antennas are closer to the surface. Since the path loss is higher close to the surface, adding a PEC surface shows a stronger effect and save more of the otherwise dissipated power in the surface in this latter case.

4.3.4.3 Scheme 2: PEC-Skin-PEC

Scheme 2 studies the influence of a PEC placed under the transmitter and the receiver worn on the human body. As shown in Fig. 4.29, the PEC plates under the antennas result in the increase of the link budget. In the following, the gain factor G is evaluated considering $d_1 + d_2 + d_3 = 0.5$ m. Let us define the total length of PEC as $d_{\text{PEC}} = d_1 + d_3$, coefficients α_1 and α_3 are defined as follows $\alpha_1 = d_1/d_{\text{PEC}}$ and $\alpha_3 = d_3/d_{\text{PEC}} = 1 - \alpha_1$.

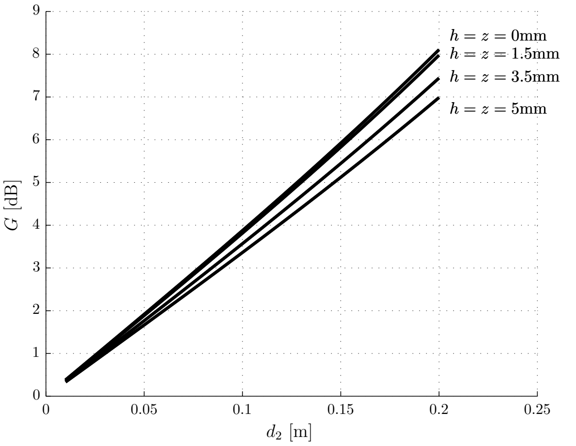

Figure 4.31: Scheme 1. Computed gain factor values G obtained by adding a PEC plate of length d_2 for various values of $h = z$.

Fig. 4.32 presents the variation of G with d_{PEC}. Using equal values for $\alpha_1 = \alpha_3 = 0.5$ leads to the best performance. In [89], the effect of a circular groundplane is studied. It is shown that increasing the groundplane size decreases the currents in the propagation surface and reduces the energy transmitted inside the surface. This leads to a better link budget as suggested by the results presented here. The radiation patterns presented in [89] show that more power is dissipated in the surface closer to the antennas. In conclusion, the PEC surface increases the link budget and by reciprocity, swapping α_1 and α_3 gives the same results.

Fig. 4.33 presents the gain factor for different values of the antenna heights h and z with a coefficient $\alpha_1 = 0.5$ which is the optimal value. The results are not as straightforward as in Fig. 4.31. Two different effects contribute to the modification of the path loss. When h varies, the radiation pattern of the antenna does change as well, thereby leading to an increase or a decrease of the gain toward the Rx direction. In addition, as h increases, the shielding effect of the ground plane becomes

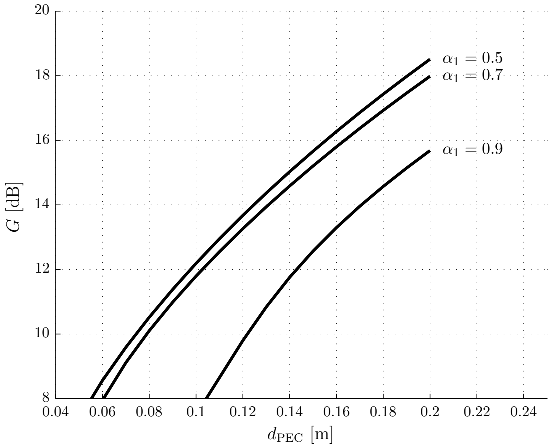

Figure 4.32: Scheme 2. Computed gain factor values G obtained by adding a PEC plate of length d_{PEC} with $h = z = 3$ mm, for various values of α_1 (PEC length repartition between transmitter and receiver side).

less effective and more energy is lost inside the skin.

4.3.4.4 Discussion

By comparing the two scenarios and Fig. 4.30 and 4.32, it can be easily deduced that scheme 2 has a better link budget than scheme 1 for the same total length of PEC. It is shown that the use of a 3.5-cm metallic plate in front of each antenna allows improvement of the power budget by 10 dB. This seems to be a high constraint. However, in subsection 3, a metallic adhesive paper has been used and it showed great performance. The malleability of such matter makes it practical for body-centric communications. Also, scheme 1 increases the link budget of about 5 to 10 dB by using a metallic surface between the two antennas. This can be useful for replacing relays and saving power with a passive structure. Globally, using the two presented schemes and multiple electro textile surfaces may accommodate saving up to 30 dB without the need of any active equipment.

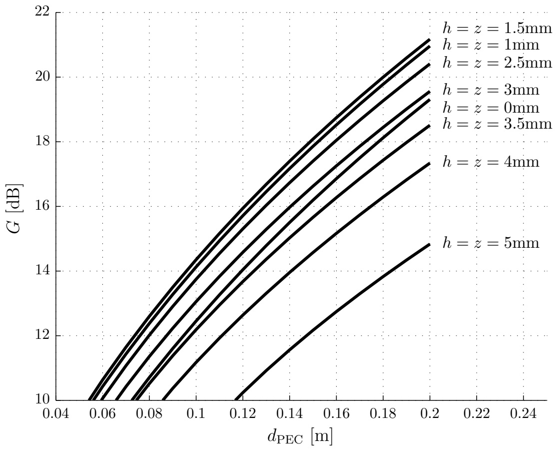

Figure 4.33: Scheme 2. Computed gain factor values G obtained by adding a PEC plate of length d_{PEC} with $\alpha_1 = 0.5$ for various values of $h = z$.

4.4 Summary

In this chapter, we presented a theoretical analysis of the propagation on a human torso assumed to be flat. The electric field has been then calculated using Norton's equations. The results of a measurement campaign conducted at 60 GHz on the front of the torso of a human subject for both normal and tangential polarizations. A logarithmic path loss in dB is proposed to model vertical and horizontal links and numerical parameters are derived.

In the case of around torso propagation, creeping wave formulation for both normally and tangentially polarized electromagnetic waves traveling on a circular path around a cylinder are given. Such formulations can be used to predict the path loss of an on-body 60 GHz communication link. Measurements carried on a brass cylinder and on the torso of real human body at 60 GHz are in good agreement with creeping waves analytic model. A linear path gain has been derived and values of the approximated power decay exponent have been summarized for different frequencies and values of the radius of the cylinder. Further, the phase velocity of creeping waves is theoretically investigated and experimentally validated.

Finally, an efficient method for propagation enhancement using metallic sheets is proposed. This problem is theoretically studied with Millington equations. It has been quantitatively shown that using longer metallic insert increases the path loss reduction and therefore, increases the link budget. Placing a PEC surface between the two antennas allows one to save between about 1 and 10 dB depending on the length of the surface. However, placing the metallic plate under the antennas allows to save up to 20 dB for the same size of the surface. This technique can easily be implemented for passive relaying of power.

Chapter 5

Near-Body Propagation

Contents

5.1 Introduction

One of the most probable scenarios would be the presence of the human body next to the communication device. The widespread of smartphones and tablets has increased the need for higher wireless data rates in a close region around the human body (against the ear, in front of the user,...). We choose to define a new spatial region from 5 to 30 cm away from the body, referred to as the *Near-Body* zone. This zone corresponds to the region where the user often places his smartphone, tablet or laptop.

In this chapter, a simple diffraction model is proposed for a receiver located from 5 to 30 cm away from the body. The model is similar to deterministic BAN channel models [90, 91]. The simplicity of the model does not allow an exact description of the channel since it does not take into account complex interactions such as arm movements, etc. However, the model is able to spatially characterize the channel around the human body and to give a physical understanding of the phenomenon.

Section 5.2 presents the numerical implementation of the indoor off-body channel model. General considerations about the model, the spatial region under study and the simulations are also presented. Then, Section 5.3 studies the mean attenuation of the channel over the bandwidth in this Near-Body scenario. Also, a discussion of the communications aspects is given. Section 5.4 presents the experimental validation. Finally, section 5.5 concludes this chapter.

5.2 Indoor Near Body Channel Implementation

In chapter 3, an off-body channel model has been derived by modeling the human body by a circular cylinder. The cylindrical model has been widely used in the literature [92] and it is convenient to model static (or averaged) scenarios. It was shown in section 3.2.3 that the cylindrical model gives a maximum 3 dB error on the electric field power measured on a real human torso-body. In the following, we will consider that this error is small enough to consider a cylindrical model for the human body in static scenarios. However, in chapter 3, the antenna was always assumed to be at maximum 5 mm from the human body. Using the same methodology, a modified model can be derived for larger distances from 5 to 30 cm. This will model the channel between an external base station and a user using a device close to his body. The developed model is ray-based so that it can be included in Saleh-Valenzuela like channel models [56].

5.2.1 Geometry and Spatial Regions

The base station and the user are located in an indoor environment. The user holds a communication device close to him in the small zone drawn in Fig. 5.1.

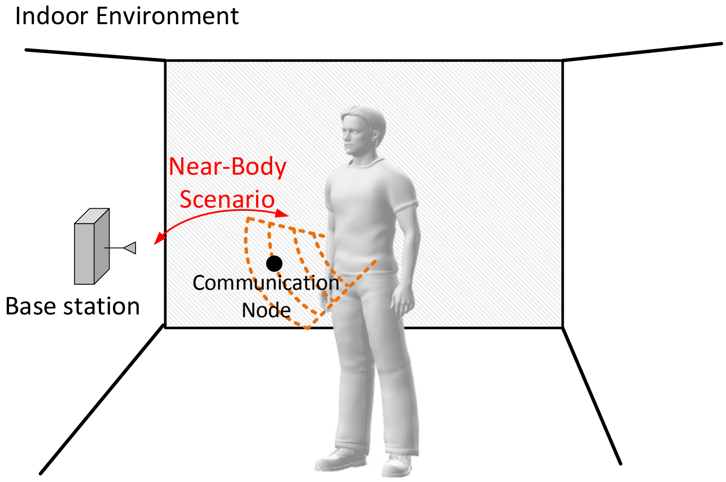

Figure 5.1: Near-Body scenario.

It is proposed to split space into two regions with respect to the transmitter (Tx): front and back as presented in Fig. 5.2. The regions are defined azimuthally with respect to the human body model (cylinder).

The regions are defined by considering the location of the receiving antenna with respect to the fixed base station. The front region is then defined as the set of points where the base station and the receiving antenna are in line-of-sight, while the locus given by the non-line-of-sight configurations is the back region.

This definition of the front and back regions are in agreement with the physical regions in chapter 3: lit and shadow regions which have been defined by considering the behaviour of the electric field (Geometrical Optics and creeping wave).

In the simulations in section 5.3, the base station and the human body are moved randomly in the indoor environment but the definition of the regions still remains as described above.

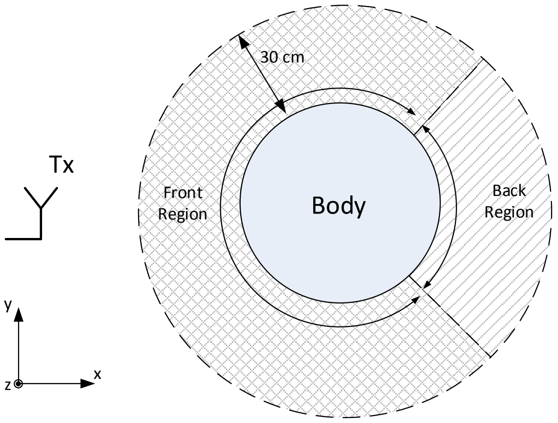

Figure 5.2: Studied Regions Scheme with respect to the transmitter (Tx).

5.2.2 Diffraction Model

The diffraction model in the front (or lit) region is calculated using Geometrical Optics (GO). These solutions are trivial and not presented here but can be found in [72].

In chapter 3, the classic modal solution of the scattering by a circular cylinder is simplified in the back (or shadow) region into a creeping wave formulation using Watson's transform. It is known that the modal solution has convergence issues while the creeping wave formulation in equation (5.1) is a fast computing and convergent solution. Due to the close-to-cylinder assumption, the sum was approximated to the first creeping wave mode. For distances between 5 cm and 30 cm, it can be numerically shown that three terms of (5.1) are enough to obtain an acceptable accuracy.

For a normalized incident plane wave transmitted by a vertically polarized antenna and called TM, the creeping wave modes formulations are:

$$\begin{aligned}
E_{\rho}^{\text{tot,TM}} &= -2\pi j \cos\theta_i e^{jkz\cos\theta_i} \sum_l j^{\upsilon_l} \tilde{a}_{\tau} H_{\upsilon_l}^{(2)'}(k\rho\sin\theta_i)\Phi_{\upsilon_l}(\phi) \\
E_{\phi}^{\text{tot,TM}} &= 2\pi \frac{\cot\theta_i}{jk\rho} e^{jkz\cos\theta_i} \sum_l \upsilon_l j^{\upsilon_l-1} \tilde{a}_{\tau} H_{\upsilon_l}^{(2)}(k\rho\sin\theta_i)\Phi_{\upsilon_l}(\phi) \\
E_{z}^{\text{tot,TM}} &= 2\pi \sin\theta_i e^{jkz\cos\theta_i} \sum_l j^{\upsilon_l} \tilde{a}_{\tau} H_{\upsilon_l}^{(2)}(k\rho\sin\theta_i)\Phi_{\upsilon_l}(\phi)
\end{aligned} \tag{5.1}$$

where k is the free space wavenumber, θ_i is the elevation angle of the incident plane wave and

$$\tilde{a}_{\tau} = \frac{1}{m}\frac{A'(\tau) - qA(\tau)}{\tau W_2(\tau) - qW_2'(\tau)}, \tag{5.2}$$

$\upsilon_l = ka + m\tau_l$, $m = (ka/2)^{1/3}$, $\Phi_{\upsilon}(\phi) = \frac{\cos\upsilon(\phi-\pi)}{\sin\pi\upsilon}$ and $q = m\sqrt{\varepsilon_r}$. ε_r is the complex relative permittivity, a is the cylinder radius and ρ is the distance between the center of the cylinder and observation point. In these equations, $H_{\upsilon}^{(2)}$ is the Hankel function and A, W_2 are respectively the standard and modified Airy functions [90]. The τ_l are obtained by solving:

$$W_2'(\tau_l) - qW_2(\tau_l) = 0. \tag{5.3}$$

For a normalized TE incident plane wave, the creeping wave modes formulation is calculated by:

$$\begin{aligned}
E_{\rho}^{\text{tot,TE}} &= -j\frac{1}{k\rho}\frac{e^{-jkz\cos\theta_i}}{\sin\theta_i} 2\pi \sum_l \upsilon_l' j^{\upsilon_l'} \tilde{b}_{\tau_l'} H_{\upsilon_l'}^{(2)}(k\rho\sin\theta_i)\Phi_{\upsilon_l'}(\phi) \\
E_{\phi}^{\text{tot,TE}} &= je^{-jkz\cos\theta_i}\frac{2\pi}{m} \sum_l j^{\upsilon_l'+1} \tilde{b}_{\tau_l'} H_{\upsilon_l'}^{(2)'}(k\rho\sin\theta_i)\Phi_{\upsilon_l'}(\phi) \\
E_{z}^{\text{tot,TE}} &= 0
\end{aligned} \tag{5.4}$$

where $\upsilon_l' = ka + m\tau_l'$, τ_l' verifies $W_2'(\tau_l) - qW_2(\tau_l) = 0$ and

$$\tilde{b}_{\tau} = \frac{1}{m}\frac{qA'(\tau) - A(\tau)}{q\tau W_2(\tau) - W_2'(\tau)}, \tag{5.5}$$

Numerically, it can be shown by comparing the creeping wave modes formulation to the Eigenmode solution [68] that the first three modes are sufficient to reach a maximal 3 dB error between both solutions in the Near-Body region. This error corresponds to the accuracy of the circular cylinder model found in the previous chapter.

5.2.3 Indoor Channel Implementation

The same methodology as section 3.3 is proposed here. Let $\mathcal{T}$ be the operator applying this transformation:

$$\begin{pmatrix} \alpha^{(i,k)'} \\ \tau^{(i,k)'} \\ \phi_{\text{rx}}^{(i,k)'} \\ \theta_{\text{rx}}^{(i,k)'} \end{pmatrix} = \mathcal{T}_{(a,\rho,\phi_0)} \begin{pmatrix} \alpha^{(i,k)} \\ \tau^{(i,k)} \\ \phi_{\text{rx}}^{(i,k)} \\ \theta_{\text{rx}}^{(i,k)} \end{pmatrix} \tag{5.6}$$

where the parameters in the near-body scenario take ' and the other parameters on the right-hand side are given by the IEEE 802.11ad model. By using the GO and the equations (5.1) and (5.4) developed above, $\mathcal{T}$ can be easily defined in the Near-Body zone by considering the two regions: $\mathcal{T}^{\text{front}}$ in the front region and $\mathcal{T}^{\text{back}}$ in the back one.

The indoor channel model considered in the following is the *Conference Room* of the IEEE802.11ad and more particularly the AP-AP one [56]. This means that the transmitting and receiving antennas are placed at the same height and are spaced by 2 meters. The cylinder modelling the human body has a 0.2 m radius and it is filled with material equivalent to the human skin ($\varepsilon_r = 7.97 - 10.92j$). The channel is evaluated all around the body (from $0\,^\circ$ to $360\,^\circ$ in azimuth) with an angular step of $0.3\,^\circ$ and from 5 to 30 cm away from it with a radial step of 0.5 mm. Hundred channel realizations using the IEEE model are evaluated and injected in the model.

The transmitting antenna is assumed to be TM polarized, i.e. the transmitted electric field is parallel to the body height. The receiver is also assumed to be z-oriented. The basic model assumes point sources as antennas but since the model is ray based, more complex antennas can be simulated by introducing radiation patterns.

In the 60 GHz bandwidth, some communication protocols have been set up such as WiGig [15]. Orthogonal frequency-division multiplexing (OFDM) is considered to achieve communication. Hence, in this chapter, it is proposed to study signal shadowing in the Near-Body zone through the mean frequency channel response over the bandwidth which is the relevant parameter describing channel attenuation for OFDM:

$$\mu_H = \frac{1}{\Delta f} \int_{\Delta f} |H(f)| \mathrm{d}f \tag{5.7}$$

with $H(f)$ the channel frequency response.

At 60 GHz, the antenna aperture can not be neglected and has to be taken into account since the carrier wavelength is 5 mm. In the following, spatial integration of the electric field is performed along on the spatial extension of the antenna aperture used in the experimental validation, which is 1 mm^2. To highlight the effect of taking into account the aperture size, both cases will be numerically investigated: with and without the spatial integration on the antenna aperture.

5.3 Mean Attenuation

5.3.1 Front Region Distribution

In the front region, the electric field is calculated using Geometrical Optics. The main impact on μ_H is due to the line-of-sight ray and the reflection off the cylinder. The other rays arriving on the body have a lower power due to the higher travelled distance. This case is well suited to be modelled by a Two-Wave Diffuse Power (TWDP) distribution [93] which models the received amplitude V as :

$$V = V_1 e^{j\Phi_1} + V_2 e^{j\Phi_2} + \sum_i \tilde{V}_i e^{j\Phi_i} \tag{5.8}$$

where $V_{1,2}$ denotes the magnitude of the specular components $1, 2$ and $\Phi_{1,2}$ are the random associated phases. The second part of (5.8) describes the non-specular components. The probability density function (PDF) of r, the magnitude of V, used to fit the simulations in Fig. 5.3–5.4 is calculated by:

$$\begin{aligned} &\text{TWDP PDF}(r; \Delta, K, \sigma) = f(r) = \frac{r}{\sigma^2} e^{\frac{-r^2}{2\sigma^2} - K} \times \\ &\frac{1}{\pi} \int_0^{\pi} e^{\Delta K \cos\theta} I_0\left(\frac{r}{\sigma}\sqrt{2K(1 - \Delta\cos\theta)}\right) \mathrm{d}\theta \end{aligned} \tag{5.9}$$

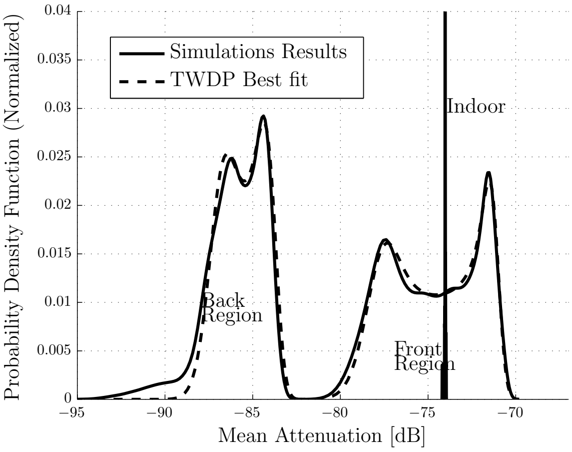

Figure 5.3: Probability density functions of the mean attenuation. Without Antenna Aperture Integration. $K = 21.65$ dB, $\Delta = 0.66$ and $\sigma = 1.25 \times 10^{-5}$ in the front region and $K = 20.85$ dB, $\Delta = 0.35$ and $\sigma = 3.50 \times 10^{-6}$ in the back one. The Indoor distribution corresponds to the case without the body presence.

where σ^2 is the variance of the diffuse part, I_0 is the modified Bessel function of the first order, K is equivalent to the Rice factor, $K = \frac{V_1^2+V_2^2}{2\sigma.^2}$, and Δ is defined by:

$$\Delta = \frac{\text{Peak Specular Power}}{\text{Average Specular Power}} - 1 = \frac{2V_1V_2}{V_1^2 + V_2^2} \tag{5.10}$$

It can be easily deduced that the specular magnitudes are given by:

$$\begin{aligned} V_1 &= \frac{\sqrt{K\sigma^2}}{2}(\sqrt{2+\Delta} + \sqrt{2-\Delta}) \\ V_2 &= \frac{\sqrt{K\sigma^2}}{2}(\sqrt{2+\Delta} - \sqrt{2-\Delta}) \end{aligned} \tag{5.11}$$

Fig. 5.3 shows an example of probability density function and its best fitting.

To fit the obtained data with a two-wave diffuse power distribution, a Maximum Likelihood (MLE) algorithm was used. However, it has been heuristically observed that the convergence of the algorithm is highly

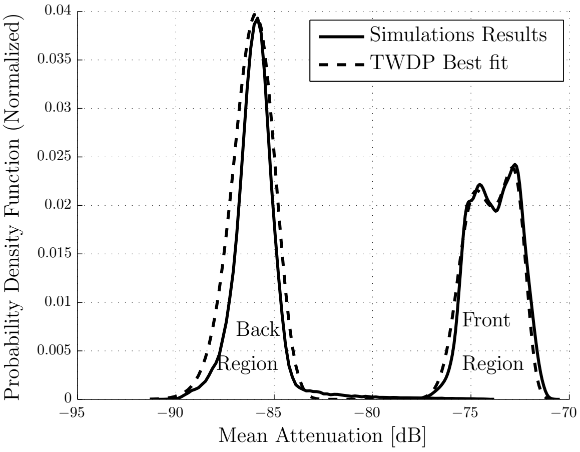

Figure 5.4: Probability density functions of the mean attenuation. With Antenna Aperture Integration. $K = 20.84$ dB, $\Delta = 0.32$ and $\sigma = 1.33 \times 10^{-5}$ in the front region and $K = 15.74$ dB, $\Delta = 0.11$ and $\sigma = 5.79 \times 10^{-6}$ in the back one

dependent to the initial values of the parameters. An easy way of getting these initial values is using the moments μ_n of the TWDP distribution:

$$\mu_n = \int_0^\infty r^n f(r) \mathrm{d}r \tag{5.12}$$

It has been shown in [94] that the first moments are:

$$\begin{aligned} \mu_1 &= (1+K)2\sigma^2 \\ \mu_2 &= (2\sigma^2)^2 \frac{1}{2}(4 + 8K + K^2(2+\Delta^2)) \\ \mu_3 &= (2\sigma^2)^3 \frac{1}{2}(12 + 36K + 9K^2(2+\Delta^2) + K^3(2+3\Delta^2)) \end{aligned} \tag{5.13}$$

Solving this system for each channel realization allows one to give initial values for the distribution parameters K, σ and Δ. Hundred simulations have been computed using the model proposed above and the values of K, σ and Δ have been obtained for each one. It has been numerically observed that these parameters can be well described by a normal distribution. For sake of clarity, the mean value and the 95%

Table 5.1: Two-Waves Diffuse Power parameters in the front region. The values are obtained numerically on hundred channel realizations.

Case	Parameter	Mean Value	$\mathrm{CI}_{95\%}$
Without Antenna Aperture Int.	K	21.70 dB	[21.04, 22.01] dB
	σ	1.23×10^{-5}	$[1.19, 1.32]\times10^{-5}$
	Δ	0.62	[0.606, 0.627]
	V_1	-73.63 dB	[-73.64, -73.58] dB
	V_2	-89.56 dB	[-89.76, -89.51] dB
With Antenna Aperture Int.	K	20.84 dB	[20.49, 21.12] dB
	σ	1.33×10^{-5}	$[1.29, 1.38]\times10^{-5}$
	Δ	0.32	[0.315, 0.326]
	V_1	-73.71 dB	[-73.72, -73.68] dB
	V_2	-95.48 dB	[-95.69, -95.44] dB

confidence interval are presented in Table. 5.1. The confidence interval gives typical bounds and is summarized as $\mathrm{CI}_{95\%}$.

Since the distribution has high K values, the distribution tends to a two-wave distribution but the TWDP is more suited to this problem. This latter better models the rising and descending parts of the curve drawn in Fig. 5.3.

5.3.2 Back Region Distribution

The back region can also been modeled by a TWDP distribution. The same parameters are calculated from the back region and summarized in Table 5.2.

By comparing the results from Tables 5.1 and 5.2, it can be seen that the antenna integration have a severe impact in the Front Region where Δ goes from 0.6 to 0.3 while in the Back one, the variations are limited. As expected, the attenuation of V_1 and V_2 can be noticed between the front and the back regions. The range of variation ($\mathrm{CI}_{95\%}$) of the parameters is also wider in the back region which creates higher variability of the obtained distributions.

Table 5.2: Two-Waves Diffuse Power parameters in the back Region. The values numerically are obtained on hundred channel realizations.

Radius	Parameter	Mean Value	$\text{CI}_{95\%}$
Without Antenna Aperture Int.	K	13.26 dB	[5.38, 18.56] dB
	σ	8.07×10^{-6}	$[0.41, 1.98]\times10^{-5}$
	Δ	0.13	[0.01, 0.27]
	V_1	-85.94 dB	[-89.47, -82.77] dB
	V_2	-108.7 dB	[-119.71,-97.54] dB
With Antenna Aperture Int.	K	15.74 dB	[8.07, 20.40] dB
	σ	5.79×10^{-6}	$[0.34, 1.31]\times10^{-5}$
	Δ	0.11	[0.01, 0.25]
	V_1	-85.82 dB	[-82.299, -89.290] dB
	V_2	-111.36 dB	[-117.50, -101.82] dB

In the front region, parameters have a low standard deviation. This can be easily explained by the fact that the behaviour of μ_H is only due to the direct ray and the reflected one off the body. It seems that the position in the environment has almost no impact on the results and hence, on the fading. On the other hand, the back region is more influenced by the user location since the fitting parameters are more affected.

By comparing the cases with and without antenna integration, it is important to notice that the antenna averages the received power implying a reduction of fading. It seems that the antenna reduces the impact of small scale variations which can be seen by the large reduction of Δ in the front region. In the back region, the two-wave distribution is no longer visible in the probability density function. In summary, it can be inferred that the antenna aperture has a strong smoothing effect on fading.

Recent research [95, 96] has identified and measured the existence of *Hyper-Rayleigh* fading. This term has been introduced to define a fading more severe than the one predicted by the Rayleigh model, which

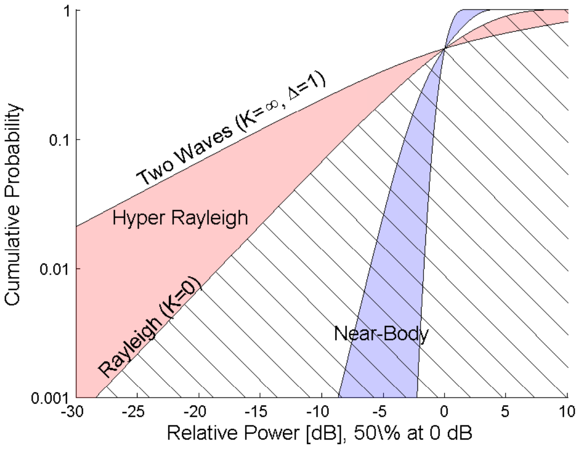

Figure 5.5: Cumulative distribution functions of the relative power representing the hyper Rayleigh region and the Near-Body scenario. The Ricean region corresponds to the hatched one.

has long been utilized as the worst-case fading. It is important to notice that *Hyper-Rayleigh* characterizes a fading behaviour rather than a distribution. It has been empirically shown in [95] that in some specific environments 20% of measurements exhibit *Hyper-Rayleigh* fading. The worst case is obtained in a two-wave environment (TWDP with $\Delta = 1$ and $K = \infty$). Since we defined the Near-Body region with a TWDP distribution, it is necessary to evaluate the type of fading that occurs.

Frolik [95] has defined three fading families (Ricean, Rayleigh and Hyper Rayleigh) based on the received power cumulative distribution function (CDF). They are presented in Fig. 5.5 for the case without antenna aperture integration where the hatched region corresponds to Ricean like fading. The cumulative probabilities have been normalized such that 0 dB corresponds to a 50% probability. The Near-Body region fading has been plotted for the Front Region using the parameters of Table 5.1. The limits of this region are obtained using the parameters in Table 5.1 at the first standard deviation.
It can be seen that the Near-Body fading is in a deep Ricean region insuring weak fading.

Table 5.3: Experimenter parameters

Symbol	Value
Center Frequency	60 GHz
Bandwidth	2 GHz
Number of frequency points	501
VNA IFbandwidth	10 kHz
Total Number of channel acquisitions	1001
Body Perimeter	93 cm
Body Height	1.85 m
Body Mass	75 kg

5.4 Experimental Comparison

The main experimental parameters are presented in Table 5.3. A collection of 1001 channel acquisition points has been obtained randomly in front of the user body using a *Rohde & Schwarz* Vector Network analyser. To increase the dynamic range a 30 dB amplifier was placed at the receiver side and a 3 dB open waveguide antenna was used at the transmitter side. The user was located at 2 m from the transmitter and the receiver was located randomly from 5 cm to 30 cm away from the user body. The antenna were both located at 1.2 m height. To allow shadowing characterization, an omni-directional antenna (*FLANN Microwave* ref. MD249-AA) has been used at the receiver side (see Fig. 3.18). The user holds a support specifically designed for moving the antenna with his hand. This could simulate the utilization of a smart-phone or tablet. In order to compare with the results without the body presence, measurements have been taken with an automatic positioning device during another channel measurement. The room were the measurements have been conducted has a size of 7 m × 4 m and a height of 2.5 m. The receiver has been placed at the center of the room and the transmitter 2 m away. A photography of the experimental set-up is presented in Fig. 5.6. The experimental mean attenuation over the bandwidth is shown in Fig. 5.7.

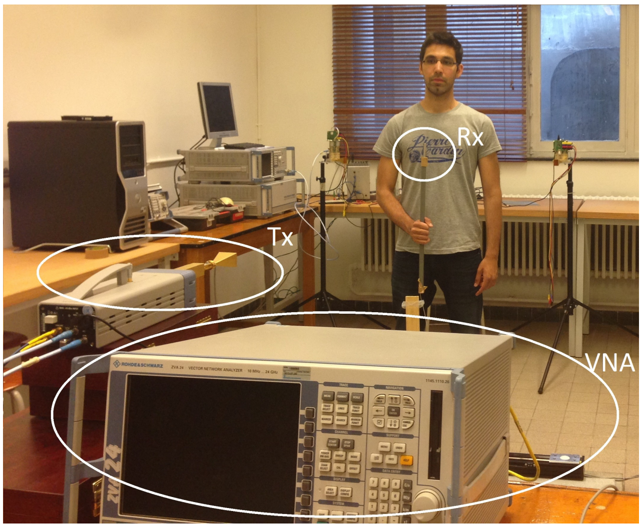

Figure 5.6: Photo of the experimental setup.

Table 5.4: Experimental best fit parameters

	Front Region	Back Region
K	21.24 dB	9.44 dB
σ	$1.3 \cdot 10^{-5}$	$12.79 \cdot 10^{-6}$
Δ	0.27	0.11
V_1	-73.49 dB	-85.42 dB
V_2	-96.87 dB	-116.62 dB

Fig. 5.7 shows a TWDP distribution in the front region. The fading seems to be comparable to the simulated results. The spread of the fading between the indoor case and the front region one is also comparable to previous results. As expected, in the back region, the averaged received power is reduced as compared to the front one.

The fitting parameters are summarized in Table 5.4. It is more convenient to compare the triple of values (V_1, V_2, σ) since it has a clear physical meaning. In the front region, the experiment results give (-73.49 dB, -96.87 dB, 1.3×10^{-5}) and the simulated values with antenna

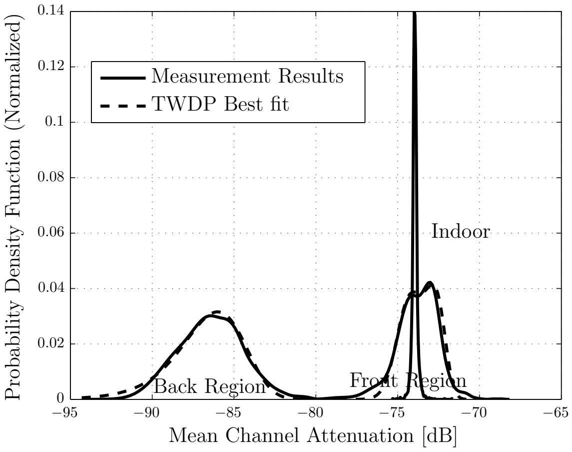

Figure 5.7: Measured Probability density functions. The presented fittings are presented in dotted line. The shadowing whithout the body presence is referred to Indoor.

aperture integration give (-73.71 dB, -95.48 dB, 1.33×10^{-5}). This shows a maximal absolute error of about 1.5 dB and a maximal relative error of about 1.5 % which shows a good agreement between experiment and simulations.

For experimental results, the back region gives the triple (-85.42 dB, -116.62 dB, 1.28×10^{-5}) and (-85.82 dB, -111.36 dB, 5.8×10^{-6}) for the simulations. These values show some differences especially regarding σ. The measured results are in the confidence interval ($\mathrm{CI}_{95\%}$) of Table 5.2.

Discrepancies between experiments and simulations point out some weaknesses of the numerical model. Actually, the signal is impacted by small movements of the body (such as trembling, breathing,...) even in a “static" scenario. Also, the body has a more complex geometry than the circular cylinder and therefore, in the simulation results, the reflections off the user body have not been completely taken into account like the arm of the user that moved the antenna.

Since the experiment gives relatively close agreement to the numerical simulations, it can be concluded that the TWDP distribution as presented here is convenient to simulate body shadowing at 60 GHz.

5.5 Summary

In this chapter, the study of the Near-Body region is proposed for 60 GHz communications. This spatial region is extended from 5 to 30 cm away of the user body. This scenario would be relevant when users are using their devices such as smartphones, laptops or tablets. A numerical model based on the indoor channel model standardized by IEEE802.11ad coupled with simple diffraction models has been used. The diffraction model assumes that the human body can be modeled by a circular cylinder. The aim of this model is to quickly characterize the fading close to the body user in static situations.

This Near-Body zone has been split up into two regions: front and back, with respect to the transmitter since the physical phenomena are different. It has been shown that this latter is spatially distributed as a two wave diffuse power distribution (TWDP) for both the front and back regions which models the fading by considering two specular components with diffuse scattered fields. The model has been illustrated in the case of the *Conference Room* of the indoor channel IEEE802.11ad. The mean attenuation of the channel has been spatially studied. The results of the fading are summarized by presenting the mean value and the 95% confidence interval of the three parameters of the TWDP distribution. Between these two regions, the specular components are reduced by about 10 to 15 dB in the back region and the diffuse power is also reduced of about 3 dB. The experiments have shown results fitting into the confidence interval of the simulations, assessing the model.

Also, the worst case of a TWDP has been discussed by introducing the concept of hyper-Rayleigh environments. Nevertheless, it has been shown that the Near-Body fading is in the Ricean-like fading region.

Chapter 6
Conclusion

During this thesis, channel models for 60 GHz Body Area Networks have been investigated. These models are necessary for next generation Wireless Body Environment Networks (WBENs) which will allow the users to be immersed in high data rate *smart environments*. The idea behind these thesis is to provide body centric channel communications in the 60 GHz band and to study the feasibility of such communications.

Off-Body Propagation and Communication

A numerical implementation of a 60 GHz off-body channel model has been proposed. This model is based on the standardized indoor channel IEEE 802.11ad and the diffraction by a circular cylinder. The propagation model is developed for both TM and TE polarizations. The model assumes that the propagation can be described by geometrical optics in the lit region and by a creeping wave in the shadow one. By using Watson's transformation, the TM and TE creeping waves are deduced from the boundary problem of plane wave scattering by a cylinder and it led to linear path loss in decibel.

Numerical simulations have been done to validate the propagation model by comparing it with the modal solution. Also, it has been shown that to improve link budget of off-body communication, remote base stations should placed on the ceiling. The experimental validation has been done on a perfect electric conductor cylinder for both polarizations. The creeping wave path gains perfectly fits with the theoretical propagation model developed in this chapter. The path gain factors have been validated for different values of elevation angles. A second experimental campaign with a real body has been done to validate the theoretical path gains in the dielectric case. The measurements showed excellent agreement with the theory. These experimental results prove that the propagation model is accurate and is thereby well suited for being included in a standard such as IEEE 802.11ad.

A numerical study of the proposed indoor channel has been performed. Channel parameters such as mean attenuation and Rice factor have been studied with the body orientation through the azimuthal angle ϕ. These parameters are compared to the indoor ones. The human body influence on the channel has been studied. It has been shown that it creates variability depending on the orientation.

Furhter, an OFDM communication based on the WiGig standard has also been computed on the developed channel. The bit error rate is studied for both TM and TE polarizations as a function of the body orientation. It has been observed that TE mode gives a better BER in the lit zone but the coverage around the body is less than TM mode for a reference BER. To solve this trade-off, a Maximum Ratio Combining scheme has been computed. Using polarization diversity, the bit error rate decreases and the coverage is maximized. Polarization diversity is also compared to spatial diversity. It is shown that using spatial diversity decreases the BER but does not solve the trade-off.

On-Body Channel Characterization

A theoretical analysis of the propagation is presented on a human torso assumed to be flat. The electric field has been then calculated using Norton's equations. The results of a measurement campaign conducted at 60 GHz on the front of the torso of a human subject for both vertical and horizontal polarizations. A logarithmic path loss in dB is proposed to model vertical and horizontal links and numerical parameters are derived.

In the case of around torso propagation, creeping wave formulation for both vertical and horizontal polarized electromagnetic waves traveling on a circular path around a cylinder are given. Such formulations can be used to predict the path loss of an on-body 60 GHz communication link. Measurements carried on a brass cylinder and on the torso of real human body at 60 GHz are in good agreement with creeping waves analytic model. A linear path gain has been derived and values of the approximated power decay exponent have been summarized for different frequencies and values of the radius of the cylinder. Further, the phase velocity of creeping waves is theoretically investigated and experimentally validated.

Finally, an efficient method for propagation enhancement using metallic sheets is proposed. This problem is theoretically studied with Millington equations. It has been quantitatively shown that using longer metallic insert increases the path loss reduction and therefore, increases the link budget. Placing a PEC surface between the two antennas allows one to save between about 1 and 10 dB depending on the length of the surface. However, placing the metallic plate under the antennas allows to save up to 20 dB for the same size of the surface. This technique can easily be implemented for passive relaying of power.

Near-Body Propagation

The study of the Near-Body region is proposed for 60 GHz communications. This spatial region is extended from 5 to 30 cm away of the user body. This scenario would be relevant when users are using their devices such as smartphones, laptops or tablets. A numerical model based on the indoor channel model standardized by IEEE802.11ad coupled with simple diffraction models has been used. The diffraction model assumes that the human body can be modeled by a circular cylinder. The aim of this model is to quickly characterize the fading close to the body user in static situations.

This Near-Body zone has been split up into two regions: front and back, with respect to the transmitter since the physical phenomena are different. It has been shown that this latter is spatially distributed as a two wave diffuse power distribution (TWDP) for both the front and back regions which models the fading by considering two specular components with diffuse scattered fields. The model has been illustrated in the case of the *Conference Room* of the indoor channel IEEE 802.11ad. The mean attenuation of the channel has been spatially studied. The results of the fading are summarized by presenting the mean value and the 95% confidence interval of the three parameters of the TWDP distribution. Between these two regions, the specular components are reduced by about 10 to 15 dB in the back region and the diffuse power is also reduced of about 3 dB. The experiments have shown results fitting into the confidence interval of the simulations, assessing the model.

Also, the worst case of a TWDP has been discussed by introducing the concept of hyper-Rayleigh environments. Nevertheless, it has been shown that the Near-Body fading is in the Ricean-like fading region.

Perspectives

This thesis provides a significant amount of results devoted to 60 GHz Body Area Networks channel modeling. However, there is still remaining a number of unresolved issues and under-investigated scenarios. A non-exhaustive list of some perspectives is then presented here.

First of all, the off-body model presented and studied in Chapter 3 considers a circular cylinder as the body model. This model can be extended by considering an elliptic cylinder as the human trunk and circular cylinders modeling the arms for instance. Also, the use of a simple reflected wave can be extended to a cluster with peculiar angle and delay distributions thanks to measurements. Further, a wideband experimental characterization of specific links is required in order to evaluate the validity of the numerical model and to build more sophisticated algorithms thanks to measured distributions and statistics. Dynamics of the channel are not investigated in Chapter 3 and are of great importance for the assessment of communication performances and routing techniques.

In Chapter 4, a great effort has been given for the characterization of the on-body channel. Models with distance between antennas have been proposed in two specific scenarios. However, there is still a need to characterize specific links by placing the nodes on the wrist, head, belt, etc. Also, the impact of the environment has to been studied in that Chapter and is expected to provide a non-negligible amount of power to the received signal. More generally, wideband characterization has to still be done.

In a more general way, multi-antenna scenarios are still lacking and are of great importance. Correlation has to measured in order to provide an accurate picture of multi-antenna BAN channels. This will allow to predict the performances of the system but also to design multi-antenna techniques and processing to improve the communication quality.

Bibliography

[1] L. Petrillo, T. Mavridis, J. Sarrazin, J.-M. Dricot, A. Benlarbi-Delai, P. De Doncker *et al.*, “BAN working frequency: a trade-off between antenna efficiency and propagation losses,” in *8th European Conference on Antennas and Propagation*, 2014.

[2] S. Van Roy, “Modélisation spatio-temporelle ultra-large bande du canal de transmission pour réseaux corporels sans fil,” Ph.D. dissertation, Ph. D. Thesis, 2010.

[3] P. A. Hasgall, E. Neufeld, M.-C. Gosselin, A. Klingenböck, and N. Kuster, “IT’IS database for thermal and electromagnetic parameters of biological tissues, version 2.2,” July 11th, 2012. [Online]. Available: http://www.itis.ethz.ch/database

[4] D. Cook and S. Das, *Smart environments: Technology, protocols and applications.* John Wiley & Sons, 2004, vol. 43.

[5] I. Oppermann, M. Hämäläinen, and J. Iinatti, *UWB: theory and applications.* John Wiley & Sons, 2005.

[6] S. K. Yong and C. C. Chong, “An overview of multigigabit wireless through millimeter wave technology: Potentials and technical challenges,” *EURASIP J. Wireless Commun. Netw.*, vol. 2007, p. 10 pages, 2006.

[7] N. Guo, R. C. Qiu, S. Mo, and K. Takahashi, “60-GHz millimeter-wave radio: Principle, technology, and new results,” *EURASIP J. Wireless Commun. Netw.*, vol. 2007, pp. 1–8, 2007.

[8] B. T. S. Rappaport, J. N. Murdock, and F. Gutierrez, “State of the art in 60-ghz integrated circuits and systems for wireless communications,” *Proceedings of the IEEE*, vol. 99, no. 8, pp. 1390–1436, 2011.

[9] C. R. T. 22-03, "Provisional recommended use of the frequency range 54.25-66 GHz by terrestrial fixed and mobile systems," *Proceedings of Euopean Postal and Telecommunications Administration Collection*, 1990.

[10] E. R. 12-09, "Radio frequency channel arrangement for fixed service systems operating in the band 57-59 GHz which do not require frequency planning," 2004.

[11] FCC, "FCC 14-154," 2014. [Online]. Available: https://apps.fcc.gov/edocs_public/attachmatch/FCC-14-154A1.pdf

[12] T. S. Rappaport, S. Sun, R. Mayzus, H. Zhao, Y. Azar, K. Wang, G. N. Wong, J. K. Schulz, M. Samimi, and F. Gutierrez, "Millimeter wave mobile communications for 5G cellular: It will work!" *Access, IEEE*, vol. 1, pp. 335–349, 2013.

[13] M. C. Models, "Mobile and wireless communications enablers for the twenty-twenty indormation," *Deliverable D1.4*, 2015.

[14] "Status of project ieee201.11 vht study group," 2007. [Online]. Available: http://grouper.ieee.org/groups/802/11/Reports/vht_update.htm

[15] C. J. Hansen, "WiGig multi-gigabit wireless communications in the 60 GHz band," *IEEE Wirel. Commun.*, vol. 18, no. 6, pp. 6–7, 2007.

[16] A. Pellegrini, A. Brizzi, L. Zhang, K. Ali, Y. Hao, X. Wu, C. Constantinou, Y. Nechayev, P. Hall, N. Chahat, M. Zhadobov, and R. Sauleau, "Antennas and propagation for body-centric wireless communications at millimeter-wave frequencies: A review," *IEEE Antennas Propag. Mag.*, vol. 55, no. 4, pp. 262–287, Aug. 2013.

[17] S. L. Cotton, W. G. Scanlon, and B. K. Madahar, "Millimeter-wave soldier-to-soldier communications for covert battlefield operations," *IEEE Communications Magazine*, vol. 47, no. 10, pp. 72–81, 2009.

[18] N. Chahat, M. Zhadobov, and R. Sauleau, "Broadband tissue-equivalent phantom for BAN applications at millimeter waves,"

IEEE Microw. Theory Tech., vol. 60, no. 7, pp. 2259–2266, Jul. 2012.

[19] X. Wu, L. Akhoondzadeh-Asl, and P. Hall, “Printed Yagi–Uda array for on-body communication channels at 60 GHz,” *Microwave and Optical Technology Letters*, vol. 53, no. 12, pp. 2728–2730, 2011.

[20] N. Chahat, M. Zhadobov, L. Le Coq, S. I. Alekseev, and R. Sauleau, “Characterization of the interactions between a 60-GHz antenna and the human body in an off-body scenario,” *Antennas and Propagation, IEEE Transactions on*, vol. 60, no. 12, pp. 5958–5965, 2012.

[21] N. Chahat, M. Zhadobov, and R. Sauleau, “Wearable textile patch antenna for BAN at 60 GHz,” in *Antennas and Propagation (EuCAP), 2013 7th European Conference on*, April 2013, pp. 217–219.

[22] T. Wu, T. Rappaport, and C. Collins, “Safe for generations to come: Considerations of safety for millimeter waves in wireless communications,” *IEEE Microwave Magazine*, vol. 16, no. 2, pp. 65–84, March 2015.

[23] o. N.-I. R. H. IEEE Standards Coordinating Committee 28, “Ieee standard for safety levels with respect to human exposure to radio frequency electromagnetic fields, 3 kHz to 300 GHz,” 1992.

[24] S. LeVine, *The Active Denial System—A Revolutionary, Non-Lethal Weapon for Today’s Battlefield.* Washington, D.C.: National Defense Univ., 2009.

[25] P. J. Riu, K. R. Foster, D. W. Blick, and E. R. Adair, “A thermal model for human thresholds of microwave-evoked warmth sensations,” *Bioelectromagnetics*, vol. 18, no. 8, pp. 578–583, 1997.

[26] H. A. Kues, S. A. D’Anna, R. Osiander, W. R. Green, and J. C. Monahan, “Absence of ocular effects after either single or repeated exposure to 10 mW/cm2 from a 60 GHz CW source,” *Bioelectromagnetics*, vol. 20, no. 8, pp. 463–473, 1999.

[27] J. Ryckaert, P. De Doncker, R. Meys, A. de Le Hoye, and S. Donnay, “Channel model for wireless communication around human body,” *Electronics letters*, vol. 40, no. 9, pp. 543–544, 2004.

[28] W. G. Scanlon and N. E. Evans, “Numerical analysis of bodyworn uhf antenna systems,” *Electronics & communication engineering journal*, vol. 13, no. 2, pp. 53–64, 2001.

[29] D. McNamara, C. Pistorius, and J. Malherbe, “Introduction to the uniform theory of diffraction,” *Artech House*, 1990.

[30] Y. Zhao, Y. Hao, A. Alomainy, and C. Parini, “UWB on-body radio channel modeling using ray theory and subband FDTD method,” *IEEE Transactions on Microwave Theory and Techniques*, vol. 54, no. 4, pp. 1827–1835, 2006.

[31] L. Liu, P. De Doncker, and C. Oestges, “Time-variant on-body channel fading characterization and modelling with dynamic human body.” COST, 2009.

[32] A. Fort, F. Keshmiri, G. R. Crusats, C. Craeye, and C. Oestges, “A body area propagation model derived from fundamental principles: Analytical analysis and comparison with measurements,” *IEEE Trans. Antennas Propag.*, vol. 58, no. 2, pp. 503–514, 2010.

[33] S. L. Cotton, R. D’Errico, and C. Oestges, “A review of radio channel models for body centric communications,” *Radio Science*, vol. 49, pp. 371–388, 2014.

[34] R. D’Errico and L. Ouvry, “Time-variant BAN channel characterization,” in *Personal, Indoor and Mobile Radio Communications, 2009 IEEE 20th International Symposium on.* IEEE, 2009, pp. 3000–3004.

[35] D. Smith, L. Hanlen, D. Miniutti, D. Rodda, B. Gilbert *et al.*, “Temporal correlation of dynamic on-body area radio channel,” *Electronics letters*, vol. 45, no. 24, pp. 1212–1213, 2009.

[36] K. Y. Yazdandoost, K. Sayrafian-Pour *et al.*, “Channel model for body area network (BAN),” *IEEE P802*, vol. 15, 2009.

[37] L. Roelens, S. Van den Bulcke, W. Joseph, G. Vermeeren, and L. Martens, "Path loss model for wireless narrowband communication above flat phantom," *Electronics Letters*, vol. 42, no. 1, pp. 10–11, 2006.

[38] E. Reusens, W. Joseph, G. Vermeeren, L. Martens, B. Latré, I. Moerman, B. Braem, and C. Blondia, "Path-loss models for wireless communication channel along arm and torso: Measurements and simulations," in *in IEEE Antennas and Propagation Society International Symposium 2007*. Citeseer, 2007.

[39] A. Fort, "Body area communications: Channel characterization and ultra-wideband system-level approach for low power," Ph.D. dissertation, Ph. D. Thesis, 2007.

[40] G. Conway, W. Scanlon, S. Cotton, and M. Bentum, "An analytical path-loss model for on-body radio propagation," in *Electromagnetic Theory (EMTS), 2010 URSI International Symposium on*. IEEE, 2010, pp. 332–335.

[41] G. Dolmans and A. Fort, "Channel model WBAN—Holst Centre/IMEC-NL, ieee 802.15 task group 6 document," *IEEE P802.15-08-0418-01-0006*, July 2008.

[42] A. Boulis, D. Smith, D. Miniutti, L. Libman, and Y. Tselishchev, "Challenges in body area networks for healthcare: The mac," *IEEE Communications Magazine*, vol. 50, no. 5, pp. 100–106, 2012.

[43] R. D'Errico and L. Ouvry, "A statistical model for on-body dynamic channels," *International journal of wireless information networks*, vol. 17, no. 3-4, pp. 92–104, 2010.

[44] S. L. Cotton and W. G. Scanlon, "A statistical analysis of indoor multipath fading for a narrowband wireless body area network," in *Personal, Indoor and Mobile Radio Communications, 2006 IEEE 17th International Symposium on*. IEEE, 2006, pp. 1–5.

[45] A. Fort, C. Desset, P. De Doncker, P. Wambacq, and L. Van Biesen, "An ultra-wideband body area propagation channel model-from

statistics to implementation," *IEEE Transactions on Microwave Theory and Techniques*, vol. 54, no. 4, pp. 1820–1826, June 2006.

[46] S. L. Cotton, G. A. Conway, and W. G. Scanlon, "A time-domain approach to the analysis and modeling of on-body propagation characteristics using synchronized measurements at 2.45 GHz," *Antennas and Propagation, IEEE Transactions on*, vol. 57, no. 4, pp. 943–955, 2009.

[47] A. Fort, C. Desset, P. Wambacq, and L. Biesen, "Indoor body-area channel model for narrowband communications," *IET microwaves, antennas & propagation*, vol. 1, no. 6, pp. 1197–1203, 2007.

[48] S. Cotton, W. Scanlon, and G. Conway, "Autocorrelation of signal fading in wireless body area networks," 2009.

[49] S. Van Roy, C. Oestges, F. Horlin, and P. De Doncker, "A comprehensive channel model for UWB multisensor multiantenna body area networks," *Antennas and Propagation, IEEE Transactions on*, vol. 58, no. 1, pp. 163–170, 2010.

[50] L. Liu, R. D'Errico, L. Ouvry, P. De Doncker, C. Oestges *et al.*, "Dynamic channel modeling at 2.4 GHz for on-body area networks," *Advances in Electronics and Telecommunications-Radio Communication Series: Recent Advances in Wireless Communication Networks*, vol. 2, no. 4, 2011.

[51] R. Di Bari, Q. H. Abbasi, A. Alomainy, and Y. Hao, "An advanced UWB channel model for body-centric wireless networks," *progress in electromagnetics research*, vol. 136, pp. 79–99, 2013.

[52] K. Ziri-Castro, W. G. Scanlon, and N. E. Evans, "Indoor radio channel characterization and modeling for a 5.2-GHz bodyworn receiver," *IEEE Antennas and Wireless Propagation Letters*, vol. 3, no. 1, pp. 219–222, 2004.

[53] S. L. Cotton and W. G. Scanlon, "Characterization and modeling of the indoor radio channel at 868 MHz for a mobile bodyworn wireless

personal area network," *IEEE Antennas and Wireless Propagation Letters*, vol. 6, pp. 51–55, 2007.

[54] A. A. Goulianos, T. W. Brown, and S. Stavrou, "A novel path-loss model for UWB off-body propagation," in *Vehicular Technology Conference, 2008. VTC Spring 2008. IEEE.* IEEE, 2008, pp. 450–454.

[55] H. Sawada, T. Aoyagi, J.-i. Takada, K. Y. Yazdandoost, and R. Kohno, "Channel models between body surface and wireless access point for UWB band," *IEEE 802.15 WPAN Document IEEE 802.15-08-0576-00-0006*, pp. 1–14, 2008.

[56] A. Maltsev et al, "Channel models for 60 GHz WLAN systems," *IEEE 802.11 TGad document: IEEE 802.11-09/0334r8*, 2010.

[57] M. Jacob, S. Priebe, A. Maltsev, A. Lomayev, V. Erceg, and T. Kurner, "A ray tracing based stochastic human blockage model for the ieee 802.11 ad 60 GHz channel model," in *Antennas and Propagation (EUCAP), Proceedings of the 5th European Conference on.* IEEE, 2011, pp. 3084–3088.

[58] M. Fakharzadeh, J. Ahmadi-Shokouh, B. Biglarbegian, M. Nezhad-Ahmadi, and S. Safavi-Naeini, "The effect of human body on indoor radio wave propagation at 57–64 GHz," in *Antennas and Propagation Society International Symposium, 2009. APSURSI'09. IEEE.* IEEE, 2009, pp. 1–4.

[59] K. Dong, X. Liao, and S. Zhu, "Link blockage analysis for indoor 60 GHz radio systems," *Electronics letters*, vol. 48, no. 23, pp. 1506–1508, 2012.

[60] M. Jacob, S. Priebe, T. Kurner, M. Peter, M. Wisotzki, R. Felbecker, and W. Keusgen, "Fundamental analyses of 60 GHz human blockage," in *Antennas and Propagation (EuCAP), 2013 7th European Conference on.* IEEE, 2013, pp. 117–121.

[61] N. Chahat, G. Valerio, M. Zhadobov, and R. Sauleau, "On-body propagation at 60 GHz," *IEEE Trans. Antennas Propag.*, vol. 61, no. 4, pp. 1876–1888, Apr. 2013.

[62] A. Guraliuc, M. Zhadobov, G. Valerio, N. Chahat, and R. Sauleau, "Effect of textile on the propagation along the body at 60 GHz," *IEEE Trans. Antennas Propag.*, vol. 62, no. 3, pp. 1489–1494, Mar. 2014.

[63] A. Guraliuc, M. Zhadobov, G. Valerio, and R. Sauleau, "Enhancement of on-body propagation at 60 GHz using electro textiles," *IEEE Antennas Wireless Propag. Lett.*, vol. 13, pp. 603–606, 2014.

[64] A. Sard, Y. Hao, Y. Zhao, S.-l. Lee, and G.-Z. Yang, "Subject-specific analysis of the on-body radio propagation channel adopting a parallel FDTD code," in *Antennas and Propagation (EuCAP), 2010 Proceedings of the Fourth European Conference on.* IEEE, 2010, pp. 1–3.

[65] Y. I. Nechayev, X. Wu, C. C. Constantinou, and P. S. Hall, "Millimetre-wave path-loss variability between two body-mounted monopole antennas," *IET Microw., Antennas Propag.*, vol. 7, no. 1, pp. 1–7, Jan. 2013.

[66] Y. Nechayev, X. Wu, C. Constantinou, and P. Hall, "Effect of wearable antenna polarization and directivity on on-body channel path gain at 60 GHz," in *Antennas and Propagation Society International Symposium (APSURSI), 2013 IEEE*, July 2013, pp. 656–657.

[67] Y. Nechayev, C. Constantinou, X. Wu, and P. Hall, "Depolarization of on-body channels and polarization diversity at 60 GHz," *IEEE Trans. Antennas Propag.*, vol. PP, no. 99, pp. 1–1, 2014.

[68] W. C. Chew, *Waves and Fields in Inhomogeneous Media.* New York: IEEE Press, 1995.

[69] M. Abramowitz and I. A. Stegun, *Handbook of Mathematical Functions with Formulas, Graphs, and Mathematical Tables.* 1992: Dover.

[70] H. H. Syed and J. L. Volakis, "High frequency scattering by a smooth coated cylinder simulated with generalized impedance boundary conditions," *Radio Sci.*, vol. 26, pp. 1305–1314, 1991.

[71] L. D. Landau and E. M. Lifshitz, *Electrodynamics of Continous Media.* 1984: Pergamon.

[72] Y. A. Kravtsov and N. Y. Zhu, *Theory of Diffraction : Heuristic Approaches.* 2010: Alpha Science.

[73] C. A. Valagiannopoulos, "An overview of the watson transformation presented through a simple example," *Progress In Electromagnetics Research, PIER 75*, pp. 137–152, 2007.

[74] E. Biglieri, R. Calderbank, A. Constantinides, A. Goldsmith, A. Paulraj, and P. H. V., *MIMO Wireless Communications.* Cambridge University Press, 2007.

[75] K. Norton, "The propagation of radio waves over the surface of the earth and in the upper atmosphere," *Radio Engineers, Proceedings of the Institute of*, vol. 24, no. 10, pp. 1367–1387, 1936.

[76] M. Grimm and D. Manteuffel, "Norton surface waves in the scope of body area networks," 2014.

[77] H. Ghannoum, R. D'Errico, C. Roblin, and X. Begaud, "Characterization of the UWB on-body propagation channel," in *Antennas and Propagation, 2006. EuCAP 2006. First European Conference on*, Nov 2006, pp. 1–6.

[78] V. A. Fock, "Diffraction of radiowaves around the earth's surface," *Acad. Sci. USSR. J. Phys.*, vol. 9, pp. 255–266, 1945.

[79] R. Paknys and N. Wang, "High-frequency surface field excited by a magnetic line source on an impedance cylinder," *IEEE Trans. Antennas Propag.*, vol. 35, no. 3, pp. 293–298, 1987.

[80] K. Li and Y.-L. Lu, “Electromagnetci field from a horizontal electric dipole in the spherical electrically earth coated with n-layered dielectrics,” *Progress In Electromagnetics Research*, vol. 54, pp. 221–244, 2005.

[81] R. W. P. King, G. J. Fikioris, R. B. Mack, and R. W. P. King, *Cylindrical antennas and arrays.* Cambridge, U.K.:Cambridge University Press New York, 2002.

[82] T. Alves, B. Poussot, and J.-M. Laheurte, “Analytical propagation modeling of BAN channels based on the creeping-wave theory,” *IEEE Trans. Antennas Propag.*, vol. 59, no. 4, pp. 1269–1274, 2011.

[83] R. Vaughan and J. Andersen, *Channels, propagation and antennas for mobile communications.* IEE, London, United Kingdom, 2003.

[84] S. Van Roy, O. Oestges, F. Horlin, and P. De Doncker, “On-body propagation velocity estimation using ultra-wideband frequency-domain spatial correlation analyses,” *Electronics Letters*, vol. 43, no. 25, pp. 1405 – 1406, 2007.

[85] G. Millington, “Ground-wave propagation over an inhomogeneous smooth earth,” *Proceedings IEE Part IV*, vol. 96, no. 39, pp. 53–64, Jan. 1949.

[86] C. Bourlier and G. Kubicke, “Ground wave propagation along an inhomogeneous rough surface in the hf band: Millington effect for a flat earth,” *IEEE Trans. Geosci. Remote Sens.*, vol. 49, no. 4, pp. 1374–1382, Apr. 2011.

[87] L. Petrillo, T. Mavridis, J. Sarrazin, D. Lautru, A. Benlarbi-Delai, and P. De Doncker, “Analytical creeping wave model and measurements for 60 GHz body area networks,” *IEEE Trans. Antennas Propag.*, vol. 62, no. 8, pp. 4352–4356, Aug. 2014.

[88] J.-M. Dricot, S. Van Roy, G. Ferrari, F. Horlin, and P. De Doncker, “Impact of the environment and the topology on the performance of hierarchical body area networks,” *EURASIP J. Wireless Commun. Netw.*, vol. 2011, no. 1, pp. 1–17, 2011.

[89] A. Leitner and R. Spence, “Effect of a circular groundplane on antenna radiation,” *Journal of Applied Physics*, vol. 21, no. 10, pp. 1001–1006, Oct. 1950.

[90] T. Mavridis, L. Petrillo, J. Sarrazin, D. Lautru, A. Benlarbi-Delai, and P. De Doncker, “Theoretical and experimental investigation of a 60-GHz off-body propagation model,” *IEEE Trans. Antennas Propag.*, vol. 62, no. 1, pp. 393–402, Jan. 2014.

[91] T. Mavridis, L. Petrillo, J. Sarrazin, D. Lautru, A. Benlarbi-Delaï, and P. De Doncker, “Creeping wave model of diffraction of an obliquely incident plane wave by a circular cylinder at 60 GHz,” *IEEE Trans. Antennas Propag.*, p. 1, 2014.

[92] A. Fort, C. Desset, P. De Doncker, P. Wambacq, and L. Van Biesen, “An ultra-wideband body area propagation channel model-from statistics to implementation,” *IEEE Trans. Microw. Theory Tech.*, vol. 54, pp. 1820–1826, 2006.

[93] G. D. Durgin, T. S. Rappaport, and D. A. De Wolf, “New analytical models and probability density functions for fading in wireless communications,” *IEEE Trans. Commun.*, vol. 50, no. 6, pp. 1005–1015, 2002.

[94] D. Dixit and P. Sahu, “Performance of qam signaling over twdp fading channels,” *IEEE Trans. Wirel. Commun.*, vol. 12, no. 4, pp. 1794–1799, April 2013.

[95] J. Frolik, “A case for considering hyper-rayleigh fading channels,” *IEEE Transactions on Wireless Communications*, vol. 6, no. 4, pp. 1235–1239, 2007.

[96] ——, “On appropriate models for characterizing hyper-rayleigh fading,” *IEEE Transactions on Wireless Communications*, vol. 7, no. 12, pp. 5202–5207, 2008.

List of publications

Submitted Work

1. H. Liu, J. Sarrazin,F. Deshours, T. Mavridis, L. Petrillo, Z. Liu, P. De Doncker, and A. Benlarbi-Delaï, Performance Assessment of IR-UWB Body Area Network (BAN) based on IEEE 802.15.6 Standard, To be submitted to *IEEE Ant. Prop. Letters*, 2015.
2. L. Petrillo, T. Mavridis, J. Sarrazin, A. Benlarbi-delaï and P. De Doncker, Experimental Wideband On-Body Channel Model at 60 GHz, To be submitted to *IEEE Ant. Prop. Letters*, 2015.

Journal Papers

1. T. Mavridis, L. Petrillo, J. Sarrazin, A. Benlarbi-delaï and P. De Doncker, Wideband Off-Body Measurements and Channel Modeling at 60 GHz, Submitted to *IEEE Ant. Prop. Letters*, Under Major Review, 2015.
2. T. Mavridis, C. Leduc, L. Petrillo, J. Sarrazin, M. Zhadobov, R. Sauleau, A. Benlarbi-Delaï, P. De Doncker, Millington Effect and Propagation Enhancement in 60-GHz Body Area Networks, Submitted to *IEEE Trans. Antennas Prop.*, Under Major Review, 2015.
3. T. Mavridis, L. Petrillo, J. Sarrazin, A. Benlarbi-delaï and P. De Doncker, Polarized 60 GHz Indoor Off-Body Channels and Communications , Submitted to *Sensing and Imaging, Special Issue on Green Solutions for Body Area Networks, Elsevier*, Under Major Review, 2015.
4. T. Mavridis, L. Petrillo, J. Sarrazin, A. Benlarbi-delaï and P. De Doncker, Near-Body Shadowing Analysis at 60 GHz, *IEEE Trans. Antennas Prop.*, 1-1, 2014.

5. L. Petrillo, T. Mavridis, J. Sarrazin, A. Benlarbi-delaï and P. De Doncker, Statistical On-Body Measurement Results at 60 GHz, *IEEE Trans. Antennas Prop.*, 63-1, pp. 400-403, 2014.

6. T. Mavridis, L. Petrillo, J. Sarrazin, A. Benlarbi-delaï and P. De Doncker, V-Band Velocity Estimation of Creeping Waves around the Human Body, *IEEE Ant. Prop. Letters*, 14, pp. 313-316, 2014.

7. T. Mavridis, J. Sarrazin, L. Petrillo, P. De Doncker and A. Benlarbi-delaï, Information Spatial focusing scheme for UWB Wireless Communications in Smart Environments, *IEEE Ant. Prop. Letters*, 14, pp. 20-23, 2014.

8. L. Petrillo, T. Mavridis, J. Sarrazin, D. Lautru, A. Benlarbi-delaï and P. De Doncker, Analytic Creeping Wave Model and Measurements for 60 GHz Body Area Networks, *IEEE Trans. Antennas Prop.*, 62-8, pp. 4352-4356, 2014.

9. T. Mavridis, L. Petrillo, J. Sarrazin, D. Lautru, A. Benlarbi-delaï and P. De Doncker, Creeping wave model of Diffraction of an Obliquely Incident Plane Wave by a Circular Cylinder at 60 GHz, *IEEE Trans. Antennas Prop.*, 62-3, pp. 1372-1377, 2014.

10. T. Mavridis, L. Petrillo, J. Sarrazin, D. Lautru, A. Benlarbi-delaï and P. De Doncker, Theoretical and Experimental Investigation of a 60-GHz Off-Body Propagation Model, *IEEE Trans. Antennas Prop.*, 62-1, pp. 393-402, 2014.

Conference Papers

1. L. Petrillo, T. Mavridis, J. Sarrazin, A. Benlarbi-Delaï, P. De Doncker. Porcine skin as human body phantom at 60 GHz, *APS 2015*, Vancouver, Canada, 2015

2. L. Petrillo, T. Mavridis, J. Sarrazin, A. Benlarbi-Delaï, P. De Doncker. Indoor Channels Around a Human Subject at 2.4 GHz and 60 GHz, *APS 2015*, Vancouver, Canada, 2015

3. Z. Ma, J. Sarrazin, L. Petrillo, T. Mavridis, P. De Doncker, A. Benlarbi-Delaï. Antenna Radiation Characterization for On-Body Communication Channel Using Creeping Wave Theory, *Proc.2015 EUCAP*, Lisbon, Portugal, 2015

4. T. Mavridis, L. Petrillo, J. Sarrazin, A. Benlarbi-delaï and P. De Doncker. Human influence on 60 GHz communication in close-to-user scenario, *URSI GASS*, Beijing, China, 2014

5. L. Petrillo, T. Mavridis, J. Sarrazin, A. Benlarbi-Delaï, P. De Doncker. Near body zone characterization, *URSI GASS*, Beijing, China, 2014

6. L. Petrillo, T. Mavridis, J. Sarrazin, A. Benlarbi-Delaï, P. De Doncker. Experimental On-Body Fading and Breathing Doppler Characterization on Human Torso at 60 GHz, *International Conference on Body Area Networks*, London, United Kingdom, Sep 2014

7. J. Sarrazin, T. Mavridis, L. Petrillo, P. De Doncker, A. Benlarbi-Delaï, Modélisation de Canal pour Réseaux de Capteurs Corporels à 60 GHz, *Journées scientifiques 2014 de l'URSI France*, Paris, France, March 2014

8. T. Mavridis, L. Petrillo, J. Sarrazin, A. Benlarbi-delaï and P. De Doncker, Implementation and Study of a numerical 60 GHz Indoor Off-Body Channel, *VTC 2014*, Seoul, South Korea

9. L. Petrillo, T. Mavridis, J. Sarrazin, D. Lautru, A. Benlarbi-delaï and P. De Doncker, BAN Working Frequency: a Trade-Off Between Antenna Efficiency and Propagation Losses. *Proc.2014 EUCAP*, The Hague, Nederlands, 2014

10. A. Jafari, J. Sarrazin, L. Petrillo, T. Mavridis, P. De Doncker, and A. Benlarbi-Delaï, Localisation Indoor: Nouvelle Méthode d'Estimation de la TDOA à Partir des Signaux de Communication Millimétrique OFDM. Union Radio-Scientifiques Internationale (URSI France), 2014

11. J. Sarrazin, T. Mavridis, L. Petrillo, P. De Doncker, A. Benlarbi-Delaï. Antenna efficiency influence in Body Area Networks (BAN), *ICCS-2013*, Pilani, India, Oct 2013

12. T. Mavridis, L. Petrillo, J. Sarrazin, D. Lautru, A. Benlarbi-delaï and P. De Doncker, A 60 GHz Off-Body Channel Implementation. In 2013 IEEE International Symposium on Antennas and Propagation and USNC-URSI National Radio Science Meeting, 2013

13. L. Petrillo, T. Mavridis, J. Sarrazin, D. Lautru, A. Benlarbi-delaï and P. De Doncker, Propagation for on-body wireless links at 60 GHz. In 2013 IEEE International Symposium on Antennas and Propagation and USNC-URSI National Radio Science Meeting, 2013

14. T. Mavridis, L. Petrillo, J. Sarrazin, D. Lautru, A. Benlarbi-delaï and P. De Doncker, A 60 GHz Indoor Off-Body Channel Implementation, *COST IC1004*,TD(13)08025, Ghent, Belgium, 2013

15. L. Petrillo, T. Mavridis, J. Sarrazin, D. Lautru, A. Benlarbi-delaï and P. De Doncker, Analytical Creeping Wave Model at 60 GHz for On-Body Communications, *Proc.2013 EUCAP*, Gothenburg, Sweden, 2013, pp. 570 - 573

16. T. Mavridis, L. Petrillo, J. Sarrazin, D. Lautru, A. Benlarbi-delaï and P. De Doncker, Analytical Creeping Wave Model at 60 GHz for Off-Body Communications, *Proc.2013 EUCAP*, Gothenburg, Sweden, 2013, pp. 574 - 578

17. T. Mavridis, F. Bellens, F. Quitin, A. Benlarbi-Delaï and P. De Doncker, Analytical and Experimental Study of Spatial Focusing by UWB Time-Reversal in Indoor Environment, *Proc. PIERS*, Kuala Lumpur, Malaysia, 2012